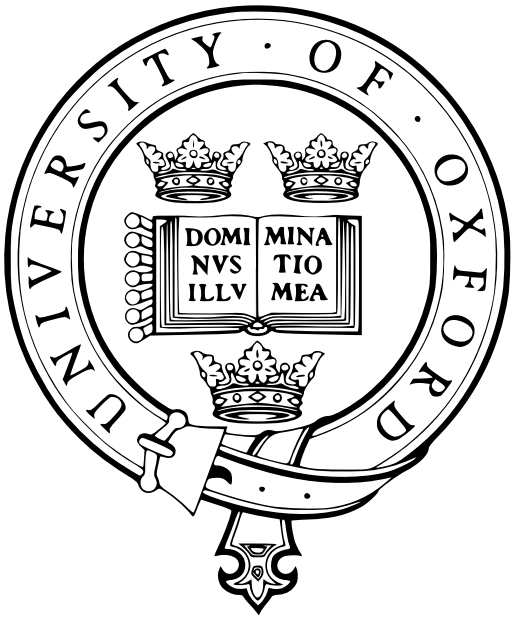


Three-dimensional colloidal crystals: Crystallisation, deformation and grain boundaries

Nicholas H. P. Orr

New College
University of Oxford

Supervisor: Prof. Roel P. A. Dullens
Co-Supervisor: Dr. Andrei V. Petukhov

A thesis submitted for the degree of
Doctor of Philosophy

August 2021

Abstract

In this thesis, the crystallisation, deformation, and grain boundaries of three-dimensionalcolloidal crystals are studied in real space using confocal laser scanning microscopy, CLSM, and in reciprocal space using small angle X-ray scattering, SAXS. Two instances of crystallisation are studied, the first being crystallisation under shear induced by capillary action. Using CLSM and SAXS, we find that drawing a high volume fraction suspension of colloidal particles into a flat and narrow capillary creates a large random hexagonal close packed, RHCP, crystal with long-range orientational order over tens of thousands of colloidal particles. Subsequently, we monitor the deformation of the shear aligned crystals under a gravitational field using CLSM and SAXS. We find that at low enough crystal volume fractions, the initial single orientation of the crystal breaks apart into many crystallites and thus, form grain boundaries at their interfaces. We characterise the rotations of the crystallites during deformation and reveal the mechanism initiating the break-up of the uniform crystal orientation. We develop a method to locate and characterise grain boundaries which can measure local grain boundary misorientations and structure as well as determine the crystal structure of the grains either side. We demonstrate the method's utility by applying it to experimental real space coordinates of colloidal particles. In particular, we consider particle coordinates obtained from an epitaxially templated colloidal $\Sigma 17$ (a coincident site lattice grain boundary) bicrystal, finding a mosaic of different grain boundary types instead of only $\Sigma 17$. We conclude with the second study of crystallisation: homogeneous crystal nucleation in a colloidal fluid. This time, crystallisation produces a crystal with many differently oriented grains and provides an opportunity to study grain boundaries and the misorientation structural changes of nuclei during nucleation. We examine the spatial misorientation variation during nucleation and growth to reveal changes with time. At early times, nuclei exhibit exclusively high misorientation angles, however, at late times, misorientation angles at the surface are higher than the angles within the nuclei cores. Thus, we show that nuclei exhibit structures intermediate between the liquid and the crystal structure at late times during nucleation and growth.

Declaration

This thesis is submitted for the degree of Doctor of Philosophy in Physical and Theoretical Chemistry at the University of Oxford. No part of this thesis has been accepted or is currently being submitted for any degree, diploma, certificate or other qualification in this University or elsewhere. This thesis is wholly my own work, except where indicated.

Contents

Abstract **i**

Declaration **iii**

1 Introduction **1**

1.1 Colloidal dispersions 1

1.2 Crystals 2

1.3 Colloidal crystals 3

1.4 Scope of the thesis 4

2 Theoretical background and experimental methods **7**

2.1 Physics of colloidal dispersions 8

2.1.1 Brownian motion 8

2.1.2 Péclet number 9

2.1.3 Particle interactions 9

2.1.4 Phase behaviour 13

2.2 Colloidal crystals 13

2.2.1 Colloidal crystal structures 14

2.2.2 Crystal lattices 15

2.2.3 Reciprocal lattice 16

2.2.4 Diffraction from colloidal crystals 18

2.2.5 Small angle X-ray scattering 22

2.3 Synthesis of colloidal TPM spheres 23
2.3.1 Conventional synthesis method 23
2.3.2 Pre-hydrolysis of TPM oil 24
2.3.3 Homogeneous fluorescent labelling of colloidal TPM particles 25
2.3.4 Solvent transfer 27
2.3.5 Colloidal dispersions 28
2.4 Confocal laser scanning microscopy 29
2.4.1 General principle 29
2.4.2 Experimental microscope setup 29
2.5 Image analysis 30
2.6 Appendix 31
2.6.1 Derivation of colloidal crystal scattering intensity 31

3 Colloidal crystallisation induced by shear from capillary action 35

3.1 Introduction 36
3.2 Theory 37
3.2.1 Random hexagonal close packed crystal structure 37
3.2.2 Quantifying stacking disorder: Wilson theory 38
3.2.3 Lateral displacement of hexagonal layers: modified Wilson theory 40
3.2.4 Shear strain 41
3.3 Methods 42
3.3.1 Colloidal samples 42
3.3.2 Flow-aligned crystal preparation 42
3.3.3 Crystal structure determination 42
3.3.4 Crystallisation mechanism 46
3.4 Results and discussion 47
3.4.1 Crystal structure and orientation 47

3.4.2 Structure evolution during crystallisation 50
3.5 Conclusion 54
3.6 Appendix 55
3.6.1 Derivation of Wilson theory for lateral displacement correlations 55
3.6.2 Structure factor calculations 59
3.6.3 Lattice constant calculation 62
3.6.4 Approximate volume fraction calculation 64

4 Deformation under gravity of shear-aligned colloidal crystals 65

4.1 Introduction 66
4.2 Methods 67
4.2.1 Colloidal samples 67
4.2.2 Crystal rotations 67
4.2.3 Lattice constant strain 69
4.2.4 Stacking parameter 69
4.3 Results and discussion 69
4.3.1 Crystal rotations 70
4.3.2 Evolution of lattice constants and volume fraction 72
4.3.3 Crystal rotation mechanism 75
4.3.4 Spatial distribution of crystal rotation 79
4.3.5 Initial volume fraction influence on fracture 80
4.3.6 Change of hexagonal stacking over time 82
4.4 Conclusion 82
4.5 Appendix 83
4.5.1 Errors 83

5 Grain boundary characterisation from particle coordinates 87

5.1 Introduction 88

5.2 Theory 90
5.2.1 Orientation, misorientation and symmetry 91
5.2.2 Visualising orientations and misorientations 96
5.3 Grain and grain boundary characterisation method 98
5.3.1 Nearest neighbour identification 98
5.3.2 Registration, orientation, and structure assignment 99
5.3.3 Separation of grains 103
5.3.4 Grain boundary location, misorientation and visualisation 103
5.4 Results and discussion 104
5.4.1 Grain boundary structure in a templated colloidal bicrystal 104
5.4.2 Characterisation of homogeneously nucleated polycrystalline structures . 110
5.5 Conclusion 114
5.6 Appendix 115
5.6.1 Nearest neighbour cluster size distributions 115
5.6.2 Angle cut off 115
5.6.3 Grain boundary particles 117

6 Misorientation during homogeneous nucleation of a colloidal crystal 119

6.1 Introduction 120
6.2 Methods 122
6.2.1 Sample preparation 122
6.2.2 Crystalline proportion and structure analysis 122
6.3 Results and discussion 124
6.3.1 Nucleation and growth 124
6.3.2 Intra-nuclei misorientation during nucleation 124
6.3.3 Spatial misorientation variation 128
6.3.4 Isolating a homogeneous nucleation event 128

6.4 Conclusion 132
6.5 Appendix 133
6.5.1 Bond coherence 133
6.5.2 Crystalline proportion for the isolated nucleus 133
6.5.3 Nearest neighbours 134

7 Conclusion and outlook **137**

Bibliography **139**

Chapter 1

Introduction

1.1 Colloidal dispersions

Colloidal dispersions encompass many biological and technological systems [1]. They consist of dispersions of microscopic particles with a typical size range of 10 to 1000 nm dispersed in a solvent and are often simply referred to as *colloids* [1]. A uniting feature of colloidal systems is the movement of the particles by Brownian motion, whereby the asymmetric bombardment of molecules in the solvent transfers momentum to the particles. Measurement of this very phenomenon by Perrin in 1909 [2] allowed an experimental measure of Boltzmann's constant, providing experimental evidence for the (at the time) much debated atomic nature of matter. The behaviour of colloidal dispersions is dominated by the interactions between the particle surfaces; the surface area of 1 m^3 dispersion of colloidal spheres can be in excess of 400 football pitches. Manipulation of the forces between particle surfaces produces a dramatic effect on the behaviour and properties, with examples in nature including milk, blood, river water, and others in industry such as aerosols and paint [1, 3].

Not only are colloidal dispersions important in their own right, but since the late 1980s they have been employed as model systems to explore fundamental aspects of condensed matter physics. Several characteristics enable their use as model systems. Firstly, their movement by Brownian motion allows the particles to explore configurational space. This allows the particles to reach equilibrium distributions analogous to those of atoms and molecules and to display corresponding phase behaviour [3–5]. Secondly, colloidal systems display structure on

a length scale of $\approx$ 1 μm, much larger than structures of atomic systems with a length scale of $\approx$ 1Å, allowing three-dimensionalimaging of colloidal structures at the single particle level using confocal microscopy techniques [6]. Thirdly, colloidal dispersions display slow response times of $\approx$ 1 s compared to their atomic counterparts with faster response times of $\approx$ 3 ns [7], making fast phenomena easily accessible in colloidal dispersions with relatively simple video techniques. Additionally, the interactions between the particles may be tuned to manipulate their assembly to mimic a variety of phases: for example, particle attractions can be increased by adding salt [8,9] or depletants [10,11] or suppressed by grafting polymers to their surfaces [12]. Furthermore, particle shape can be modified to introduce directional interactions, examples include rods [13,14], bananas [15], cubes [16], and dumbbells [17,18], thus, changing their phase behaviour. Finally, the particle interactions are soft so are readily manipulated with external electric [9,19], gravitational [20], and optical [21,22] fields.

Colloidal structures may also be examined using scattering techniques [23–30] to provide measurements of the global structure that are complementary to the local structure provided by CLSM measurements [31]. As a consequence of structural features on the micrometer scale, they scatter wavelengths of light in the visible spectrum strongly, a property that often makes colloidal structures appear cloudy or, in the case of periodic structures like colloidal crystals, coloured and iridescent.

1.2 Crystals

Crystals are ubiquitous in nature, with the vast majority of organic and inorganic compounds exhibiting a solid crystal phase at low temperatures where atoms are arranged in an ordered, repeating manner. They find essential use in technical applications from metals in bridge building to thin films of indium tin oxide crystals in touch screens [32,33]. Crystals have been used to reach many historically significant scientific goals. For example, the structures of DNA [34,35] and insulin [36,37] were discovered from X-ray diffraction experiments of their respective crystals.

The properties of crystalline materials may be modified to make them useful in a variety of applications. Properties such as strength, ductility and electrical conductivity can be tuned by manipulating the network of differently oriented regions, termed grains, within the crystal.

For example, grain size can be manipulated to create better and longer lasting materials, a technique that dates from early hammering and annealing of copper across the Near East (Iran, Egypt, Turkey etc.) around 2000 BC [38]. However, it has not been until modern day that the microscopic mechanisms behind the processes have been revealed. The Hall-Petch scaling law [39,40], established in the 1950s, relates the increased strength of a hammered metal to the decrease in the grain sizes. In fact, if the grain size is too small, it can have the opposite effect, where a material can exhibit superplasticity, [41,42]. Therefore, understanding of the underlying grain structure is at the heart of the machining and production of many crystalline materials.

1.3 Colloidal crystals

Crystals can also occur in the colloidal domain, both naturally and synthetically. Precious opals are a famous example of natural colloidal crystals. Their iridescent quality, originates from the interference of light with the periodic arrangement of close packed silica spheres within. Colours appear as the distance between the colloidal silica particles in the repeating pattern of the crystal is on the same length scale as the wavelengths of visible light. As such, synthetic colloidal crystals composed of colloidal spheres made in a laboratory have a similar appearance, as shown in Fig.1.1.

Because of the periodic modulation of the dielectric constant being on a length scale similar to the wavelength of visible light, they also have potential for use as three-dimensional photonic band gap crystals, [43–45]. These are materials that do not allow the propagation of photons in all directions with frequency in the visible region [45]. Crystals with photonic band gaps would find applications in a variety of situations such as low threshold lasers and wave guides with low loss bends [46]. However, it still remains a challenge to synthesise such materials on a large scale [47] due to the requirement of large grain sizes (ideally single crystal) and challenging constraints on crystal structures [48].

An early example of the scientific significance of colloidal crystals was the experimental realisation of entropic crystallisation of hard spheres [49], first proposed by early simulations [50, 51]. It turns out that when the volume fraction, the volume of spheres divided by the total volume of the dispersion, is above 0.49 entropy increases on ordering the colloidal particles in a crystalline configuration. The entropic gain from hard spheres being able to move more

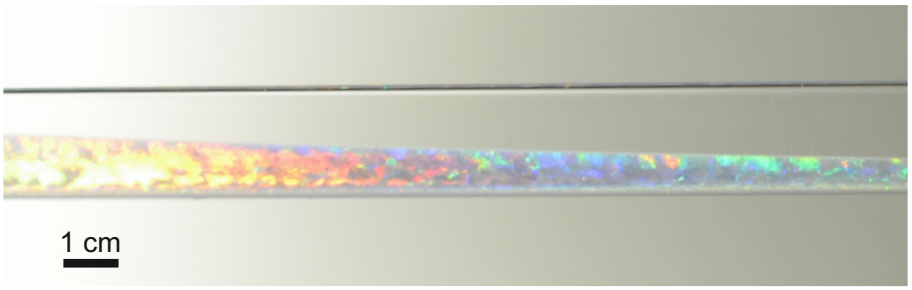


Figure 1.1: A crystal composed of colloidal organosilica spheres suspended in tetrahydronapthelene displaying iridescence similar to natural opal under white light illumination.

freely when in a crystalline arrangement than in a disordered arrangement overcomes the loss in configurational entropy. The use of colloidal crystals as model systems has continued in recent decades. Microscopy studies have revealed the microscopic arrangements of particles occurring within phenomena such as grain boundary migration [22] and nucleation [52, 53]. As explained above, colloidal systems are soft and are easily deformed. This softness is also exhibited by colloidal crystals that may be deformed using optical tweezers to carefully manipulate structures like grain boundaries [22] or to characterise their mechanical porperties [54]. Furthermore, defects occur with a small energetic penalty and therefore with great prevalence. Therefore, colloidal crystals are an ideal tool to model and study crystalline defects such as, dislocations [55] stacking faults [29], and grain boundaries [56, 57].

1.4 Scope of the thesis

Within this thesis, we address several unanswered questions of crystal physics by making use of colloidal crystals as a model system. One of the main challenges facing the realisation of photonic band gap crystals for advanced material applications is synthesising large mono-domain photonic crystals. We demonstrate that large domains of singly oriented colloidal crystal can be produced simply, by capillary action induced shear. Furthermore, we characterise the long term stability of these shear-aligned crystals within a gravitational field. We demonstrate the control of grain boundary misorientation within these crystals as the single domain breaks apart, a valuable asset for manipulation of material properties by grain boundary engineering. Next, we detail a method to fully characterise the structure of grain boundaries in three dimensions with particle level resolution in response to the absence of a robust and general means to do so. Finally, we examine the accuracy of the assumptions of classical nucleation theory by measuring structure evolution

during homogeneous crystal nucleation. By doing so we add to the discussion of why classical nucleation theory predicts nucleation rates so far from those measured in experiments [58]. To these ends, the crystallisation, deformation and grain boundaries of three-dimensional colloidal crystals are examined. We do so in real space and in reciprocal space using CLSM and SAXS, providing complementary information on the structure and dynamics of the colloidal model systems.

Firstly, in chapter 2, the theoretical background and experimental methods essential for the following chapters is detailed. The physics of colloidal dispersions is outlined with an emphasis on their crystalline phase. Following this, the structure of colloidal crystals and the appearances of their diffraction patterns are explained. Next, synthesis techniques for colloidal particles are introduced alongside techniques for imaging by microscopy. Finally, image analysis methods used to reveal the structure of the colloidal crystals from diffraction and microscopy images are discussed.

This thesis examines two instances of colloidal crystallisation, the first being crystallisation under shear. In chapter 3, shear-induced crystallisation is examined using both CLSM and SAXS techniques. Crystals with orientational order over tens of thousands of particles are produced by drawing a highly concentrated dispersion of colloidal particles into a narrow capillary. We examine the process which aligns the particles into hexagonally packed layers, and characterise the three-dimensional crystal structure.

In chapter 4, the shear-aligned crystals are examined as they undergo deformation under gravitational stress. From an initial uniform orientation, the crystal breaks up into many differently oriented regions as strain builds up towards the bottom of the crystal. However, we show that the misorientations between the grains in the resulting multi-domain crystal are not random, but share a rotation axis. Therefore, we introduce a route for controlled grain boundary misorientations. We find that the deformation behaviour is influenced by the volume fraction of colloidal particles within the dispersion, observing that the orientational break up is suppressed at higher volume fractions.

In chapter 5, a method to determine the microscopic structure of grains and the local misorientations of grain boundaries from particle coordinates is detailed. The method reveals the full grain and grain boundary network from the coordinates of particles, unlike many methods presented in the literature. After explaining the algorithmic details, the advantages of its use are

shown by application to colloidal crystals. Although we apply the method to colloidal crystals as an example, the method may be equally applied to coordinates obtained from simulations.

Finally, in chapter 6, homogeneous crystal nucleation is studied using a colloidal model system. Here, we uncover the microscopic arrangements of individual colloidal particles during crystal nucleation from the fluid. Using the method described in chapter 5, we explicitly measure the misorientations between neighbouring particles within nuclei. We find that the colloidal crystal nuclei grow as randomly hexagonal close packed crystals and show that misorientations between neighbours in nuclei at early times are higher than those at late times. Lastly, we show how misorientations within a nucleus changes within the nucleus itself and provide a spatial map of misorientations from the more ordered nucleus core to the less ordered surface.

Chapter 2

Theoretical background and experimental methods

Abstract

In later chapters, the crystallisation, deformation, and grain boundaries of three-dimensional colloidal crystals are studied. The following chapter describes the theoretical background and methods for later chapters. Firstly, the physics of colloidal dispersions is discussed with an emphasis on the crystal phase. Subsequently, the structure of colloidal crystal crystals and their interaction with light, diffraction, is detailed. Next, the synthesis of colloidal TPM particles is introduced and finally, the imaging of colloidal crystals using confocal laser scanning microscopy and small angle X-ray scattering is explained.

2.1 Physics of colloidal dispersions

2.1.1 Brownian motion

Colloidal dispersions encompass a wide range of heterogeneous systems where solid or fluid particles are dispersed within a fluid, the solvent. A colloidal dispersion contains particles, approximately 1μm in size that exhibit the spontaneous jiggling movement known as Brownian motion. This phenomena is named after Robert Brown who first observed the random motion of pollen in water under microscope magnification in 1827 [59]. It was not until early in the 20^{th} century that Einstein and Sutherland almost simultaneously developed the theory behind Brownian motion [60, 61]. It was proposed that the motion arises from collisions between the molecules in the solvent and the colloidal particles. At any one time, the impacts may not be equal on all sides of the particle resulting in momentum transfer from the solvent molecules to the particles. In 1910, Perrin experimentally observed the diffusion of colloidal particles and used the theories of Einstein and Sutherland to provide a measurement for the Boltzmann constant, [2], adding to the ever mounting evidence for the reality of atoms and molecules. To this end, Perrin used the Stokes-Einstien equation for the diffusion of a spherical particle [4]:

$$D = \frac{k_{\text{B}}T}{6\pi\eta a}, \tag{2.1}$$

which shows how the diffusion constant, D, is related to the viscosity, η, of the dispersing fluid, the temperature, T, the Boltzmann constant, k_{B}, and particle radius, a. As such, at typical temperatures and solvent viscosities, colloidal particles have a size range of 10nm -10μm However, these are by no means strict bounds. The upper bound of the colloidal length scale is blurry as Brownian motion may be experienced for much larger particles given a small viscosity and high enough temperature. At the lower end of the length scale, the smallest colloids have a size similar to macro molecules such as large polymers and proteins. A typical time scale for colloidal diffusion may be approximated by considering the relation between the mean squared displacement, $\langle r^2 \rangle$, at time, t, and the diffusion coefficient:

$$\langle r^2 \rangle = 6Dt, \tag{2.2}$$

which leads us to a typical Brownian timescale, τ_{B}:

$$\tau_{\mathrm{B}} \approx \frac{l^2}{6D}, \tag{2.3}$$

on the order of seconds, where we take $l \approx 1\mu\mathrm{m}$, as a typical colloidal particle length scale.

2.1.2 Péclet number

The competition between the thermal energy of particles and the energy in an external field such as gravity or flow is characterised by the Péclet number, P_{e}. Péclet numbers may be defined for different types of flow, two of relevance to this thesis are flow due to sedimentation as a result of gravity, and flow under shear. In chapter 3, crystallisation at a high P_{e} due to shear is studied, and in chapter 4, the break up of a colloidal crystal with high P_{e} due to sedimentation under gravity is discussed. Firstly, P_{e} for sedimentation is defined as [5]:

$$P_{\mathrm{e}} = \frac{4\pi a^4 \Delta\rho g}{3k_{\mathrm{B}}T}, \tag{2.4}$$

where $\Delta\rho$ is the difference in mass density between the particles and the dispersing solvent and g is acceleration due to gravity. Secondly, P_{e} for shear is defined as: [4]

$$P_{\mathrm{e}} = \frac{6\pi\eta a^3 \gamma'}{k_{\mathrm{B}}T}, \tag{2.5}$$

where γ' is the shear rate (with units of s^{-1}). In both cases a $P_{\mathrm{e}} > 1$ means that the energy from flow or gravity dominates the thermal energy and hence, dominates the behaviour of the colloidal dispersion.

2.1.3 Particle interactions

The character of a colloidal dispersion is dominated by the interactions between the surfaces of the colloidal particles. As such, by tuning the interactions an astounding array of behaviours may be achieved. The most important behaviour in this thesis is the ability of the colloidal dispersion to crystallise. The interaction energy between two isotropic colloidal particles is given by the pair potential, U, which can be modelled by the Derjaguin-Landau-Verwey-Overbeek (DLVO)

theory [62, 63]. The DLVO potential is often written as [1]:

$$U_{\mathrm{DLVO}}(r) = U_{\mathrm{VdW}}(r) + U_{\mathrm{rep}}(r), \tag{2.6}$$

where it describes the competition between the attractive Van der Waals forces and the repulsive forces between the charged surfaces of the colloidal particles whose centres of mass are a distance, r, apart. For a system of identical spherical particles with radii, a, large on the length scale of the interactions so that the Derjaguin approximation [1, 8] holds, we obtain the potential in a symmetric (z:z) electrolyte as [1]:

$$U_{\mathrm{DLVO}}(r) = \pi a \left(-\frac{H}{12\pi r} + \frac{64 k_{\mathrm{B}} T c_0^* \Gamma_0^2}{\kappa^2} \exp(-\kappa r) \right) \tag{2.7}$$

where the first term in brackets is the Van der Waals contribution, which has a negative sign and is therefore, attractive. The second term in the brackets is the electrostatic repulsive term, which is positive and therefore, repulsive. The parameter, H, is the Hamaker constant which describes the interaction energy between the two colloidal particles through the dispersing solvent [1, 8]. The parameter, c_0^*, is the concentration of ions in the bulk, far away from the charged particle surfaces of the colloidal particles and the parameter, Γ_0, is related to the potential at the charged surface, that is, the surface potential, Φ_0, so that $\Gamma_0 = \tanh\left(\frac{ze\Phi_0}{4k_{\mathrm{B}}T}\right)$, where z is the valance of the (z:z) electrolyte and e is the elementary charge. Finally, κ^{-1} is the Debye length, which characterises the length scale of the decay of the electrostatic repulsion, which for a (z:z) electrolyte is [1]:

$$\kappa^{-1} = \sqrt{\frac{\varepsilon_0 \varepsilon_r k_{\mathrm{B}} T}{2 z^2 e^2 c_0^*}}, \tag{2.8}$$

where ε_0 is the electronic permittivity of free space, and ε_r is the dielectric constant of the dispersing solvent. Equation 2.8 shows that κ^{-1} decreases upon increasing the concentration of electrolyte. This is because the repulsive potential at the surface of the colloidal particles is screened by counter ions that accumulate near the oppositely charged surface. In this way an electronic *double layer* is created at the colloidal particle surface. The competition between the repulsive and attractive interactions is shown in Fig.2.1a. The potentials for a stable and unstable interaction potential are marked by $U_{\mathrm{DLVO}}(1)$ and $U_{\mathrm{DLVO}}(2)$, respectively. Note that $U_{\mathrm{DLVO}}(1) = U_{\mathrm{VdW}} + U_{\mathrm{rep}}(1)$ and $U_{\mathrm{DLVO}}(2) = U_{\mathrm{VdW}} + U_{\mathrm{rep}}(2)$. For $U_{\mathrm{DLVO}}(2)$ the energetic barrier

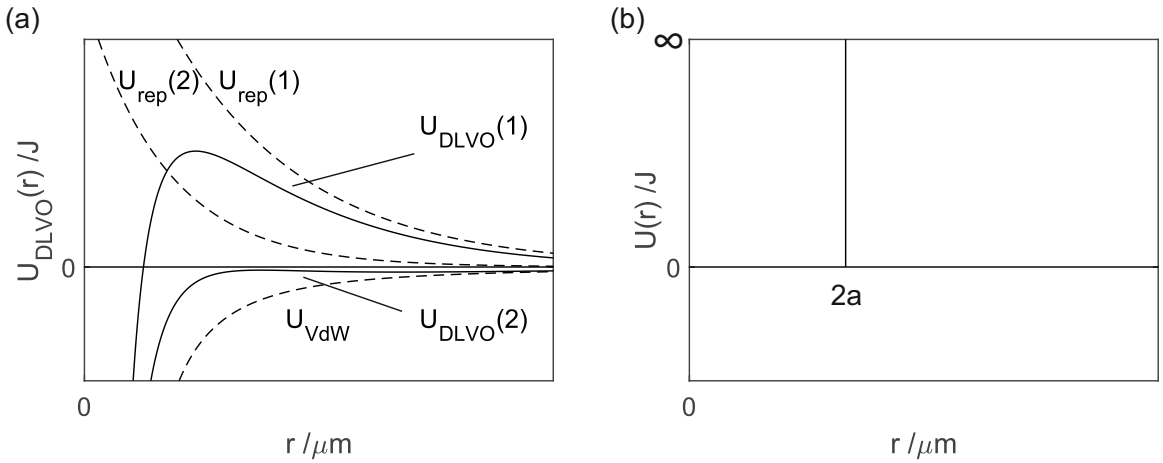


Figure 2.1: (a) Inter-particle interaction according to the DLVO potential, $U_{\mathrm{DLVO}}(1)$ and $U_{\mathrm{DLVO}}(2)$ are stable and unstable respectively. (b) Hard sphere interaction potential

for coagulation is less than $k_{\mathrm{B}}T$, therefore making the dispersion unstable to coagulation.

The interaction potential between colloidal particles can be tuned by the addition of chemical agents, for example polymers or salt. By grafting a polymer onto the surface of a colloidal particle, two particles are sterically hindered from coming into close contact. The minimum approach is increased which decreases the maximum attraction possible (less negative) from $U_{\mathrm{VdW}}(r)$, thus preventing aggregation. Adding salt decreases the repulsive potential by increasing the screening of the surface charge and, at high enough salt concentrations, the attractive Van der Waals potential dominates, causing aggregation. In fact, this is the cause of delta formation when fresh water from rivers carrying colloidal silt meets the salty (NaCl) sea water [64]. The fresh water has a low electrolyte concentration, c_0^*, and therefore, has a large κ^{-1} resulting in a larger (more positive) $U_{\mathrm{rep}(r)}$ (see Fig.2.1a $U_{\mathrm{rep}}(1)$), thus making the silt stable in solution. However, sea water has a greater electrolyte concentration, generating greater double layer screening with reduced κ^{-1}, causing $U_{\mathrm{rep}}(r)$ (see Fig.2.1a $U_{\mathrm{rep}}(2)$) to be dominated by $U_{\mathrm{VdW}}(r)$ decreasing the energetic barrier to coagulation in $U_{\mathrm{DLVO}}(r)$. The silt aggregates to produce particles with a larger radius. Therefore, P_{e} increases (see equation 2.4) and the silt sediments to create the river delta.

Colloidal particles in this thesis are suspended in apolar solvents when imaged in 3D using confocal microscopy. A more detailed discussion follows in section 2.3.4 and 2.4. Here, the surface charge is low due to the high free energy of ionisation causing particle aggregation due to Van der Waals forces. The commercial dispersant OLOA (Chevron Chemical Co.) is used as a charge control agent in colloidal systems. OLOA lowers the free energy of ionisation by providing

an enthalpic reward for ionisation, increasing Γ_0, thus stabilising the particles (see equation 2.7). However, $U_{\text{rep}}(r)$ may be suppressed by increasing the concentration of OLOA, creating more ions in solution which decreases κ^{-1} by charge screening. The mechanism behind this behaviour is possibly due to OLOA stabilising ions within inverse micelles [65, 66]. OLOA is composed mostly of polyisobutylene succinimide, however, as it is proprietary, the exact structure and charge controlling mechanism is unknown. There is also evidence for OLOA exhibiting a steric stabilisation effect, where polymers are grafted to the colloidal particle surfaces.

Another colloidal dispersion is used in chapters 5 and 6. In this case the solvent is saturated with tetrabutylammonium bromide which forms ions in solution to provide charge screening and therefore, a small κ^{-1}.

By controlling surface charge and screening, κ^{-1} can be made small compared to a and in combination with steric repulsion offered by grafted polymers, $U_{\text{DLVO}}(r)$ is well approximated by the hard sphere potential $U_{\text{HS}}(r)$:

$$U_{\text{DLVO}}(r) \approx U_{\text{HS}}(r) = \begin{cases} 0, & \text{if} \quad r > 2a \\ +\infty & \text{otherwise.} \end{cases} \tag{2.9}$$

Colloidal dispersions studied in this thesis have a hard sphere like interaction. For the colloidal TPM dispersions described in section 2.3.5 and used in chapters 3 and 4, the lack of long range repulsion is confirmed in Ref [67] where optical trapping experiments on similar colloidal dispersions with the same methodology as in Ref [68] were performed. Colloidal particles were trapped in weak optical potentials and brought into contact. Differences in the separation of the particles and the separation of the traps were found only when the traps were closer than the particle diameter, confirming their hard sphere interaction. Different methods have been employed to verify hard sphere interactions in other colloidal dispersions, similar to those used elsewhere in this thesis. For the poly(methyl methacrylate), particles discussed in chapters 5 and 6, the first peak in the radial distribution function is found to agree well with the size of the colloidal particle [69], the position of which does not change with volume fraction at high volume fractions [70], indicating a hard sphere interaction. Finally, for the silica particles discussed in chapter 5, k^{-1} was calculated to be 10 nm [57], small compared to the colloidal particle diameter of 1.6 μm. Therefore, the interaction is characterised as hard sphere.

2.1.4 Phase behaviour

The thermal agitation of colloids allows the particles to explore configurational space and to reach an equilibrium distribution analogous to those of atoms and molecules [3–5, 49]. As a result, a large array of phase behaviour is seen in colloidal systems such as gasses, liquids, gels, glasses and liquid crystals. The phase of particular interest in this thesis is the crystal phase.

For particles with hard sphere interactions, free energy is driven by entropy and the phase behaviour is entirely determined by the volume fraction, ϕ, which is given by:

$$\phi = \frac{V_{\mathrm{p}}}{V_{\mathrm{tot}}}, \tag{2.10}$$

where V_{p} is the volume of all of the particles in dispersion and V_{tot} is the total volume of the dispersion. The phase behaviour of hard spheres was initially proposed by early simulations [50,51] and experimentally confirmed by colloids with a hard sphere like interaction potential [49]. An increase in ϕ induces a phase transition to a repeating structure, known as a crystal, as shown in the phase diagram in Fig.2.2. Below $\phi = 0.49$ the colloidal particles entirely exist in a fluid-like arrangement, between $0.49 < \phi < 0.54$ the crystal and fluid co-exist and at $\phi > 0.54$ colloidal hard spheres entirely crystallise [49,51]. It may seem unusual that in this entropy driven system the ordered, crystalline state would be thermodynamically favourable over a disordered fluid at all. In fact, the crystalline phase maximises entropy at high ϕ. This is because the maximum volume fraction for a disordered arrangement of spheres is $\phi = 0.64$ whereas for a close packed crystalline phase is $\phi = 0.74$. Therefore, in the fluid at high volume fractions, the particles become jammed with their movements impeded by their neighbours. The gain in entropy associated with the particles being able to move about their lattice site outweighs the reduction in entropy from forming an ordered array from a disordered jumble of particles at volume fractions above $\phi = 0.54$, resulting in crystallisation.

2.2 Colloidal crystals

Crystals are ubiquitous in nature, with the vast majority of organic and inorganic compounds exhibiting a solid crystal phase where many atoms are arranged in an ordered, repeating manner. Likewise, colloidal crystals are composed of colloidal particles in place of the atoms or molecules.

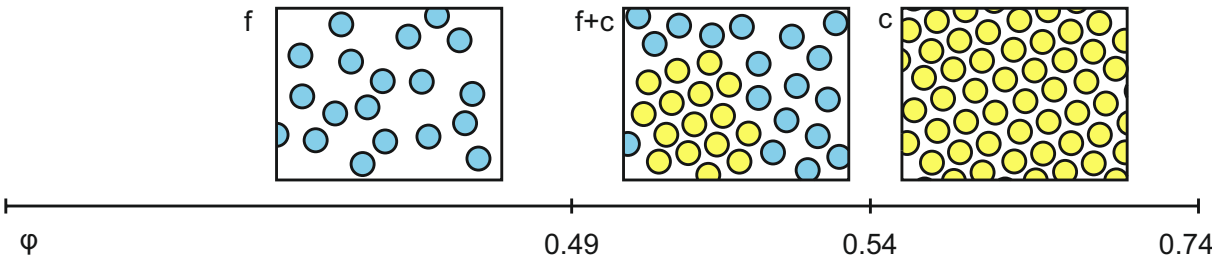


Figure 2.2: Phase behaviour of hard spheres with volume fraction, ϕ, f and c refer to fluid and crystal order respectively. Particles coloured in blue are locally fluid like and in yellow are locally crystalline.

Colloidal crystals are soft compared to their atomic counterparts. Let us consider the relationship between stress, $\frac{F}{A}$, strain, $\frac{\Delta L}{L}$ and the Young's modulus, E, of a material:

$$\frac{F}{A} = E\frac{\Delta L}{L}, \tag{2.11}$$

where F is a force normal to the area A and ΔL is the change in length from the original length of the material, L (deformation). Equation 2.11 shows that a smaller E relates to a larger deformation under an applied force. By rearranging, we arrive at an approximate expression for the Young's modulus in terms of energies and lengthscales:

$$E = \frac{FL}{A\Delta L} \approx \frac{U}{l^3}, \tag{2.12}$$

where U and l correspond to the typical energy and length scale of the system, respectively. For colloidal crystals $E \approx \frac{k_B T}{1\mu m^3}$ as opposed to $E \approx \frac{eV}{1A^{\circ 3}}$ for atomic crystals leading to a Young's modulus roughly 14 orders of magnitude smaller for colloidal crystals. This results in soft colloidal crystals that are easily deformed in external fields, for example in a gravitational field, as studied in chapter 4. Furthermore, defects occur with a smaller energetic penalty and therefore with great prevalence. Therefore, colloidal crystals are an ideal tool to model and study crystalline defects such as vacancies, stacking faults (see chapters 3, 4, 5 and 6), and grain boundaries (see chapters 5 and 6).

2.2.1 Colloidal crystal structures

Hard sphere colloidal dispersions crystallise into structures that minimise the free energy by maximising entropy. Such structures exhibit the maximum volume fraction of spheres in three dimensions, and thereby provide a relatively large free volume for particle movements at $0.49 <$

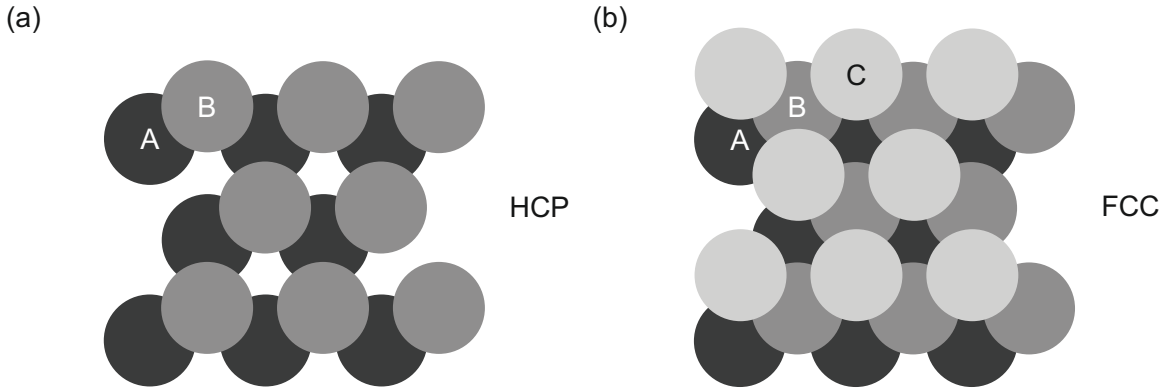


Figure 2.3: (a) and (b) show the hexagonal stacking in HCP and FCC respectively. A, B and C hexagonal layers are marked and coloured in different shades of grey.

$\phi < 0.74$, and thus, high entropy. This is achieved with so called 'close packed' structures. Close packed crystal structures contain planes of hexagonally arranged spheres. Stacking these planes so that the spheres of the layer above sits in the recesses created by the layer below results in three positions of layers with different in plane translations. If the three lateral positions are labelled A, B and C, hexagonal close packed, HCP, is formed by a repeated sequence of $...ABABAB...$ as shown in Fig.2.3a, whereas face centered cubic, FCC, is formed by a repeated sequence of $...ABCABC...$ as shown in Fig.2.3b. In chapter 3, the random hexagonal close packed, RHCP, structure is introduced, which contains a mixture of FCC and HCP. In chapters 5 and 6, the interfaces (grain boundaries) between FCC and HCP crystals will be discussed.

2.2.2 Crystal lattices

Section 2.2.1 above provided an introduction to colloidal crystal structures, however, a more detailed description enables a deeper discussion of crystal structure and diffraction. Crystals are well described by lattices, a mathematical construction of an infinitely repeating geometrical array of points in which the environment, the surrounding spatial point distribution, of each lattice point is identical. Lattices are described by lattice vectors that point along directions of repetition. The lattice vectors define edges of a unit cell which may be tessellated in space to reproduce the entire lattice. Primitive lattice vectors are those for which the unit cell contains only one lattice point. Fig.2.4a shows a hexagonal 2D lattice and two example lattice vectors $\vec{a}$ and $\vec{b}$. A unit cell is marked by the shaded region. Fig.2.4c shows the 3D hexagonal lattice unit cell and primitive lattice vectors $\vec{a}$, $\vec{b}$ and $\vec{c}$.

Colloidal crystals structures are created by adding a motif of one or many colloidal particles

onto each lattice site. These are placed at positions given by vectors pointing from the origin of a unit cell:

$$\vec{u}_j = x_j\vec{a} + y_j\vec{b} + z_j\vec{c}, \tag{2.13}$$

where x_j, y_j and z_j are fractional coordinates of the lattice vectors, and where j spans the members of the unit cell. An HCP colloidal crystal may be generated by placing a motif containing colloidal particles at positions $\vec{u}_1$ and $\vec{u}_2$ in the unit cell where the fractional coordinates are:

$$\begin{aligned}(x_1, y_1, z_1) &= (0, 0, 0) \quad \text{and} \\ (x_2, y_2, z_2) &= \left(\frac{2}{3}, \frac{1}{3}, \frac{1}{2}\right).\end{aligned} \tag{2.14}$$

Particles at positions $\vec{u}_1$ and $\vec{u}_2$ are in A and B layers respectively and $\vec{c}$ becomes twice the separation between hexagonal planes. Similarly, FCC can be produced with a motif of three colloidal particles on a hexagonal lattice. Although this is not the conventional definition (FCC is a lattice itself and can be defined more simply with other lattice vectors) the appreciation of the hexagonal lattice in FCC is useful for later discussions of randomly close packed crystals.

2.2.3 Reciprocal lattice

The reciprocal lattice is an abstract yet powerful tool in the study of the diffraction of crystals. As its name suggests, it is formed from the reciprocal of the real lattice. If $\vec{a}$, $\vec{b}$ and $\vec{c}$ are three, non co-planar primitive lattice vectors that describe a 3D lattice, then the reciprocal lattice is defined by [71]:

$$\vec{a^*} = 2\pi\frac{\vec{b}\times\vec{c}}{\vec{a}\cdot(\vec{b}\times\vec{c})}, \quad \vec{b^*} = 2\pi\frac{\vec{a}\times\vec{c}}{\vec{a}\cdot(\vec{b}\times\vec{c})}, \quad \vec{c^*} = 2\pi\frac{\vec{a}\times\vec{b}}{\vec{a}\cdot(\vec{b}\times\vec{c})}, \tag{2.15}$$

where $\vec{a^*}$, $\vec{b^*}$ and $\vec{c^*}$ are the primitive reciprocal lattice vectors. Fig.2.4b shows 2D reciprocal lattice points of the real space lattice from Fig.2.4a with primitive reciprocal lattice vectors $\vec{a^*}$ and $\vec{b^*}$ emanating from the origin of reciprocal space, o. Again, a unit cell is composed from the lattice vectors, shown shaded in grey. The 3D unit cell and reciprocal unit cell of a hexagonal lattice is shown in Fig.2.4(c) and (d) respectively. Notice that a consequence of hexagonal symmetry is that the lattice vectors $\vec{a}$ and $\vec{b}$ are not parallel to their reciprocal counterparts, $\vec{a^*}$

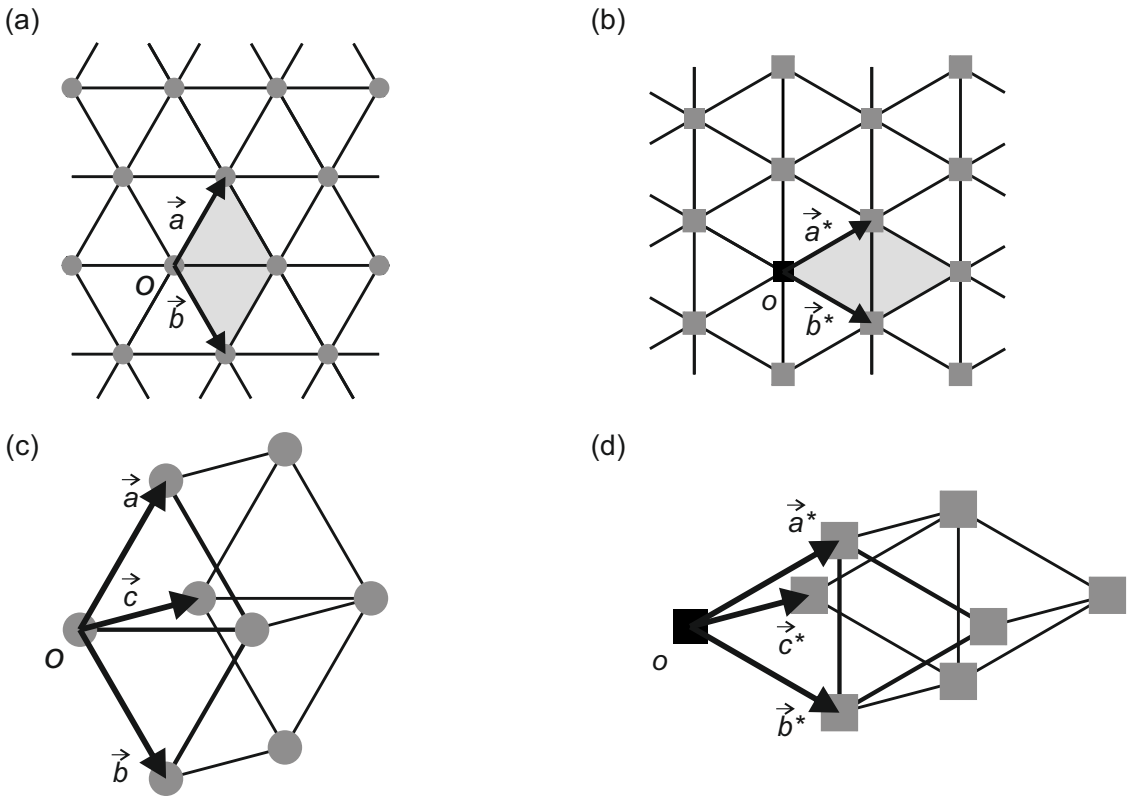


Figure 2.4: (a) 2D crystal lattice with primitive lattice vectors $\vec{a}$ and $\vec{b}$ pointing from an example unit cell origin (b) Corresponding reciprocal lattice of (a). The primitive reciprocal lattice vectors $\vec{a^*}$ and $\vec{b^*}$ are shown pointing from the origin of reciprocal space, o. (c) 3D hexagonal lattice, with primitive lattice vectors $\vec{a}$, $\vec{b}$ and $\vec{c}$. (d) Corresponding reciprocal lattice with primitive reciprocal lattice vectors $\vec{a^*}$, $\vec{b^*}$ and $\vec{c^*}$. The thickness of the lines in (c) and (d) represents the perspective.

and $\vec{b^*}$, respectively. In general, a reciprocal lattice vector $\vec{G}_{hkl}$ may be composed from a linear sum of primitive reciprocal lattice vectors:

$$\vec{G}_{hkl} = h\vec{a^*} + k\vec{b^*} + l\vec{c^*}, \tag{2.16}$$

where h, k and l are integers termed Miller indices. In the following section, (2.2.4) reciprocal lattice vectors will be used to describe the appearance of the diffraction patterns of crystals.

2.2.4 Diffraction from colloidal crystals

The diffraction of photons, electrons or neutrons allows the study of structure in a wide range of materials. Here, the interaction of photons with colloidal crystals is introduced.

The diffraction condition

When the periodic length scale of the crystalline material is approximately equal to or greater than the wavelength of the radiation, the radiation is scattered in directions away from the incident beam in accordance to the structure of the material. This happens as a result of the interference of waves as though they were reflected from different planes within the structure. Constructive interference occurs when the path difference between scattered waves is an integer number of wavelengths. The angles of constructive interference are given by the Bragg reflection condition [71]:

$$2d_{hkl} \sin\theta = n\lambda, \tag{2.17}$$

where $d_{hkl} = \frac{2\pi}{G_{hkl}}$, where $G_{hkl} = |\vec{G_{hkl}}|$, (for lowest integer multiples of h, k and l) is the separation of the planes within the periodic structure of the colloidal crystal, θ is the angle of incidence measured from the plane and λ is the radiation wavelength. Although this description illustrates the reflection condition in terms of planes of lattice points, a more detailed approach is required to deal with the spatial distribution of colloidal particles in the crystal. To this end, we start with an alternative definition of the diffraction condition considering the scattering vector, $\vec{q} = \vec{k'} - \vec{k}$, as shown in Fig.2.5. Here, $\vec{k'}$ and $\vec{k}$ are diffracted and incident wave vectors of magnitude $2\pi/\lambda$ and direction parallel to their respective propagation directions (see Fig.2.5).

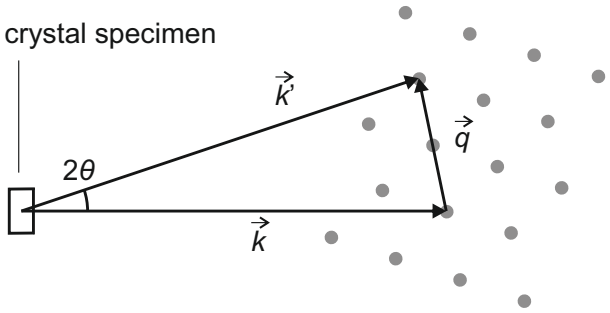


Figure 2.5: Scattering geometry showing incident wave vector $\vec{k}$, diffracted wave vector $\vec{k'}$ and the scattering vector $\vec{q}$.

The diffraction condition is given by [71]:

$$\vec{q} = \vec{G}_{hkl}, \tag{2.18}$$

where $\vec{G}_{hkl}$ is a reciprocal lattice vector from equation 2.16. This states that the possible X-ray reflections are governed by the set of reciprocal lattice vectors, shown by the grey points to the right of Fig.2.5. As such, a diffraction pattern is a map of the reciprocal lattice of a crystal. The X-ray (Bragg) reflections may be labelled with Miller indices hkl so that the reflection at $\vec{G}_{1\bar{1}0}$ may be represented as $1\bar{1}0$, where $\bar{1}$ represents -1.

Scattering intensity

For colloidal crystals, the scattering intensity, $I(\vec{q})$, may be written as proportional to the normalised form factor, $F(\vec{q})$, multiplied by the normalised structure factor, $S(\vec{q})$:

$$I(\vec{q}) \propto F(\vec{q})S(\vec{q}). \tag{2.19}$$

A derivation may be found in appendix 2.6.1. Together, the form factor and structure factor account for the spatial distribution of electron density in the crystal.

Form factor

The form factor describes the contribution of the colloidal particles themselves to the scattering intensity. For colloidal particles, the form factor is modeled as scattering from spheres of uniform electron density with equal radius, a. Provided that the X-ray refractive index of the

colloidal particle, n_{p}, and the surrounding medium, n_{m}, are very similar, the phase shift from each scattering volume element in the colloidal particle does not differ appreciably from the incident incident beam, $2ka|\frac{n_{\mathrm{p}}}{n_{\mathrm{m}}} - 1| \ll 1$, the Rayleigh-Gans-Debye approximation applies [72]. The colloidal dispersions studied in this thesis contain micrometre size colloidal particles with refractive indices such that $|\frac{n_{\mathrm{p}}}{n_{\mathrm{m}}} - 1| \approx 1 \times 10^{-6}$ [73–75], and are exposed to X-rays with energy of 8.5 keV, with wave vector $k = \frac{2\pi}{\lambda} = 4.3 \times 10^{10}$ m^{-1}. Therefore, using $a = 0.7 \times 10^{-6}$ m, $2ka|\frac{n_{\mathrm{p}}}{n_{\mathrm{m}}} - 1| = 0.06 \ll 1$, and the approximation should hold. As such, the form factor, normalised to account for electron density and particle volume and ignoring other proportionality constants, is given by the expression:

$$F(q) = \left(3\frac{\sin(qa) - qa\cos(qa)}{(qa)^3}\right)^2, \tag{2.20}$$

where $q = |\vec{q}|$. As with the electron density, the form factor is spherically symmetric. The radial decay of $F(q)$ is shown in Fig.2.6a. In a real colloidal crystal, the colloidal particles are not all of the same size. Their size distribution is quantified by their polydispersity, $p = \frac{\sigma}{a_0}$, where σ is the standard deviation in the particle radii and a_0 is the mean radius. The form factor is modified in the following way:

$$F_{\mathrm{pol}}(q, a, a_0, \sigma) = \left(\int_0^\infty 3\frac{\sin(qa) - qa\cos(qa)}{(qa)^3} D(a, a_0, \sigma)da\right)^2, \tag{2.21}$$

where the polydispersity is often accounted for using a Gaussian distribution for D, given by

$$D(a, a_0, \sigma) = \frac{1}{\sigma\sqrt{2\pi}} \exp -\frac{(a - a_0)^2}{2\sigma^2}. \tag{2.22}$$

The effect of polydispersity is to reduce the depths of the form factor minima, as shown for a $p = 0.075$ colloidal dispersion in Fig.2.6b.

Structure factor

The structure factor describes the contribution of the location of the colloidal particles within the crystal to the scattering intensity:

$$S(\vec{q}) = \frac{1}{M}\left|\sum_j^M e^{i\vec{q}\cdot\vec{r}_j}\right|^2, \tag{2.23}$$

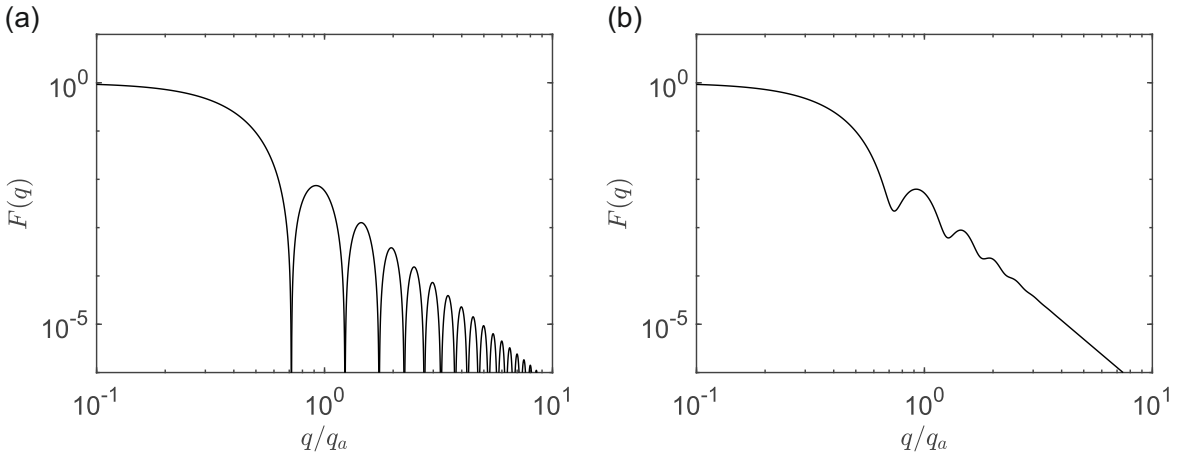


Figure 2.6: (a) Form factor for monodisperse spheres of uniform electron density, $q_a = \frac{2\pi}{a}$ (b) Form factor for spheres with a normal distribution polydispersity, $p = 0.075$.

where r_j points to the position of one of M colloidal particles in the crystal. The factor $\frac{1}{M}$ ensures the total integrated structure factor is independent of the number of particles in the crystal. For perfectly periodic crystals, the structure factor may be written in terms of N unit cells in the crystal [71]:

$$S(\vec{q}) = \frac{N^2}{M}\left|\sum_j^{M/N} e^{i\vec{q}\cdot\vec{u}_j}\right|^2, \tag{2.24}$$

where u_j is defined in equation 2.13. Following the reflection condition of equation 2.18 when the scattering vector is equal to a reciprocal lattice vector:

$$\begin{aligned}\vec{q}\cdot\vec{u}_j &= \vec{G}_{hkl}\cdot\vec{u}_j \\ &= (h\vec{a^*} + k\vec{b^*} + l\vec{c^*})\cdot(x_j\vec{a} + y_j\vec{b} + z_j\vec{c}) \\ &= 2\pi(hx_j + ky_j + lz_j),\end{aligned} \tag{2.25}$$

and thus the structure factor becomes:

$$S(hkl) = \frac{N^2}{M}\left|\sum_j^{M/N} e^{i2\pi(hx_j+ky_j+lz_j)}\right|^2, \tag{2.26}$$

with each member of the unit cell contributing the the phase of the structure factor. Diffraction peaks of high diffracted intensity appear at reciprocal lattice positions. However, colloidal crystals often crystallise in a random hexagonal close packed, RHCP, structure with no periodicity along the $\vec{c}$ direction, along which the unit cell becomes infinitely long. In chapter 3, the

structure factor of RHCP crystals will be discussed in more detail.

The above shows that colloidal particle position, size and size distribution all modify the intensities of the reciprocal lattice peaks. In some situations, the particle positions can create destructive interference to delete some of the reciprocal lattice points at so called systematic absences. In colloidal crystals, diffraction peaks can also disappear if the $\vec{q}$ corresponds to a minimum in the form factor (see Fig.2.6).

2.2.5 Small angle X-ray scattering

Chapters 3 and 4 use small angle X-ray scattering to measure structure in colloidal crystals. When the structural features are large compared to the wavelength of interacting radiation, the angle of scattering is small. Colloidal particles are larger than the wavelength of X-rays and therefore, the scattering occurs at small angles. Synchrotron X-rays are emitted from the acceleration of relativistic electrons achieved by deflecting their velocity in a magnetic field of a bending magnet. The electrons are held in the storage ring in a near circular loop by an array of bending magnets accelerating electrons at many positions on the ring providing many sources of X-rays. Fig.2.7 shows a schematic of synchrotron X-rays setup for use in small angle X-ray scattering. On the left, the electrons from the storage ring loop enter the bending magnet and emit a fan of X-rays with a range of frequencies. Next, X-ray optics remove unwanted frequencies and guide the beam to the sample. After interaction with the sample, the X-rays travel down an evacuated flight path to a detector. Small angle scattering results in the diffracted beam being very close to the direct beam. A beam stop, typically a small piece of lead, is placed to block the direct beam to avoid saturating and damaging the detector.

Experimental setup

The B16 beamline at Diamond Light Source, Didcot, UK, was set up for SAXS measurements. A multilayer monochromator was used in this experiment to select x-rays with photon energy of 8.5 keV. The beam was focused using 3 beryllium compound refractive lenses installed in front of the sample to produce a converging beam that was focused at the detector position. For the experiments we used the Photonic Science ImageStar9000 CCD detector and a Medipix4 detector. Samples in flat capillaries where mounted horizontally on a sample stage tower allowing for

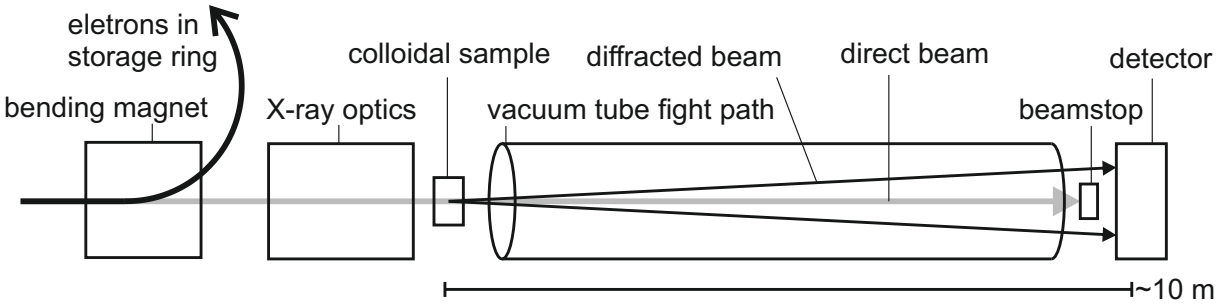


Figure 2.7: Schematic of key components of synchrotron radiation setup for small angle X-ray scattering.

computer-controlled 3D translations and rotations of the sample. The sample-detector distance was roughly 8.5 meters.

2.3 Synthesis of colloidal TPM spheres

This section details the synthesis of colloidal dispersions discussed in chapters 3 and 4. They are composed of colloidal 3-(trimethoxysilyl)propyl methacryalte, TPM, spheres. Firstly, the conventional synthesis is described, followed by a description of modifications to decrease synthesis time, to increase yield and to improve the fluorescent dyeing of the particles.

2.3.1 Conventional synthesis method

Colloidal spheres may be synthesised by spontaneous emulsion polimerisation of 3-(trimethoxysilyl)propyl methacryalte, TPM [76, 77]. The general reaction scheme starts with the hydrolysis of insoluble TPM oil in a basic aqueous solution where the methoxy groups attached to the silicon atom are exchanged for hydroxyl groups. The resulting hydrolysed TPM is water soluble. Long branched oligomers condense from the solution as an emulsion of monodisperse colloidal spheres dispersed in an aqueous solution. The droplets are stabilised by a negative charge at their surface, thus, preventing aggregation. Addition of α-azo-isobutyronitrile, AIBN, polymerises the droplets by thermally induced free radical polimersiation of the alkene groups. This forms carbon carbon bond cross links between the oligomers turning the droplet solid.

The size of the TPM particles can be tuned to between ≈ 100 nm and ≈ 2 µm in diameter by controlling the volume fraction of TPM (the volume of TPM oil divided by the total volume

of the solution of base and TPM oil) and the number of particle nuclei during condensation. The colloidal particles grow from small nuclei created at the early stages of condensation to form an emulsion. Increasing the number of nuclei by decreasing the pH decreases the final diameter of the particles [77] as the total volume of TPM is shared between more nuclei. The number of nuclei is not only affected by pH but also by stirring rate, geometry of reaction vessel and the brand and batch of TPM. Therefore, one is required to calibrate the size of TPM particles to their particular reagents and reaction apparatus. As such, recipes for TPM spheres are only a guide. Conveniently, particles can be grown from smaller nuclei until the desired size is reached. This is referred to as *seeded growth*. During the growth stage, samples from the reaction vessel can be extracted to measure droplet size. Seeded growth is particularly useful in creating particles larger than 2 μm and particles with diameters up to 5 μm have been produced.

2.3.2 Pre-hydrolysis of TPM oil

The synthesis may be modified to pre-hydrolyse the TPM oil in an acidic solution before mixing with a basic solution. Again, the method of mixing affects the size of the particle, however, there are significant advantages to synthesising particles like this. Firstly, The reaction scheme from TPM hydrolysis to sphere condensation takes roughly half the time, about 2h total. Secondly, the yield of TPM spheres is greater per volume of TPM oil, as the TPM fully hydrolyses in the acidic solution. Thirdly, the volume of the reaction vessels required is smaller, allowing for a greater yield of spheres per reaction volume.

In a typical synthesis of 2 μm diameter TPM spheres, pre-hydrolysed TPM is made by adding 1 ml of TPM oil (Arcos Organics, 98 %) to a solution of 4.75 ml of H_2O and 0.25 ml of 10 mM HCl. The solution is stirred for 1hours or until the solution becomes clear. The resulting hTPM solution is passed through a hydrophilic syringe filter to remove any residual TPM oil. In to a 50 ml beaker (internal diameter 38 mm) containing 10ml of 0.028% by weight NH_3 (aq) with a 15 by 5 mm magnetic stirrer bar at 600 rpm, the filtered hTPM solution is poured with one swift motion (final pH $\approx$ 10). The solution goes cloudy as the TPM oligomer droplets nucleate. Stirring for 1h completes the droplet growth. At this stage, the particles may be fluorescently dyed as explained in the following section (2.3.3). Finally, particles are cross-linked by increasing the stirring rate to 900 rpm and adding a pinch ($\approx 0.01\ g$) of AIBN, stirring for 5 minutes then placing in a preheated 80 $^{\circ}C$ oven for 5 hours.

Once the particles are cross linked, their size and polydispersity are determined by scanning electron microscopy, SEM. SEM images are taken under vacuum and cause the colloidal TPM particles to shrink by roughly 10% compared to their size when swollen in solution [67]. As the presence of large or small particles can hamper the crystallisation of a colloidal dispersion, in fact, a polydispersity of $p \leq 0.1$ is required for hard sphere crystallisation [78], repeated centrifugation and decanting steps are employed to remove large and small particles from the size distribution which decreases p. Typically, the small particles may be removed from a roughly 2µm diameter colloidal particle dispersion by discarding the supernatant after spinning at $900g$ for 9 minutes, repeated twice. The large particles are removed after spinning at $50g$ for 1 minute which is repeated 8 times.

2.3.3 Homogeneous fluorescent labelling of colloidal TPM particles

Imaging using confocal laser scanning microscopy, CLSM, requires firstly, a fluorescent contrast between the colloidal particles and the suspending medium, achieved by adding a fluorescent dye to either. The conventional particle dyeing procedure described in the literature [76] produces particles where some are much brighter than the others. However, the more evenly distributed the dye amongst the particles, the better the particle identification from CLSM images (see section 2.5). When the CLSM image is convoluted with the Gaussian kernel, the particles that are much brighter than their neighbours dominate the surrounding particles hindering their identification, effectively deleting them from the image.

The procedure for dyeing the colloidal particles as described in the work by Liu et al [76] was modified by changing the dye solvent from dimethyl sulfoxide, DMSO, to acetone so that the colloidal particles were dyed more uniformly. Fig.2.8a and b shows the fluorescence signal from a confocal micrsocopy image from colloidal particles dyed with a DMSO and acetone solution, respectively. Histograms of the integrated brightness of each colloidal particle are given in Fig.2.8c and d. Fig.2.8d shows a more even distribution in the acetone dyed colloidal particles as compared to the distribution in Fig.2.8c for the DMSO dye solution. The uniform dyeing is a result of acetone being insoluble in the aqueous solution containing the oligomerised TPM droplets. When the dye is dispersed in DMSO, high concentrations of dye result at positions where the dye solution is dripped into the reaction vessel, producing a small number of very bright particles.

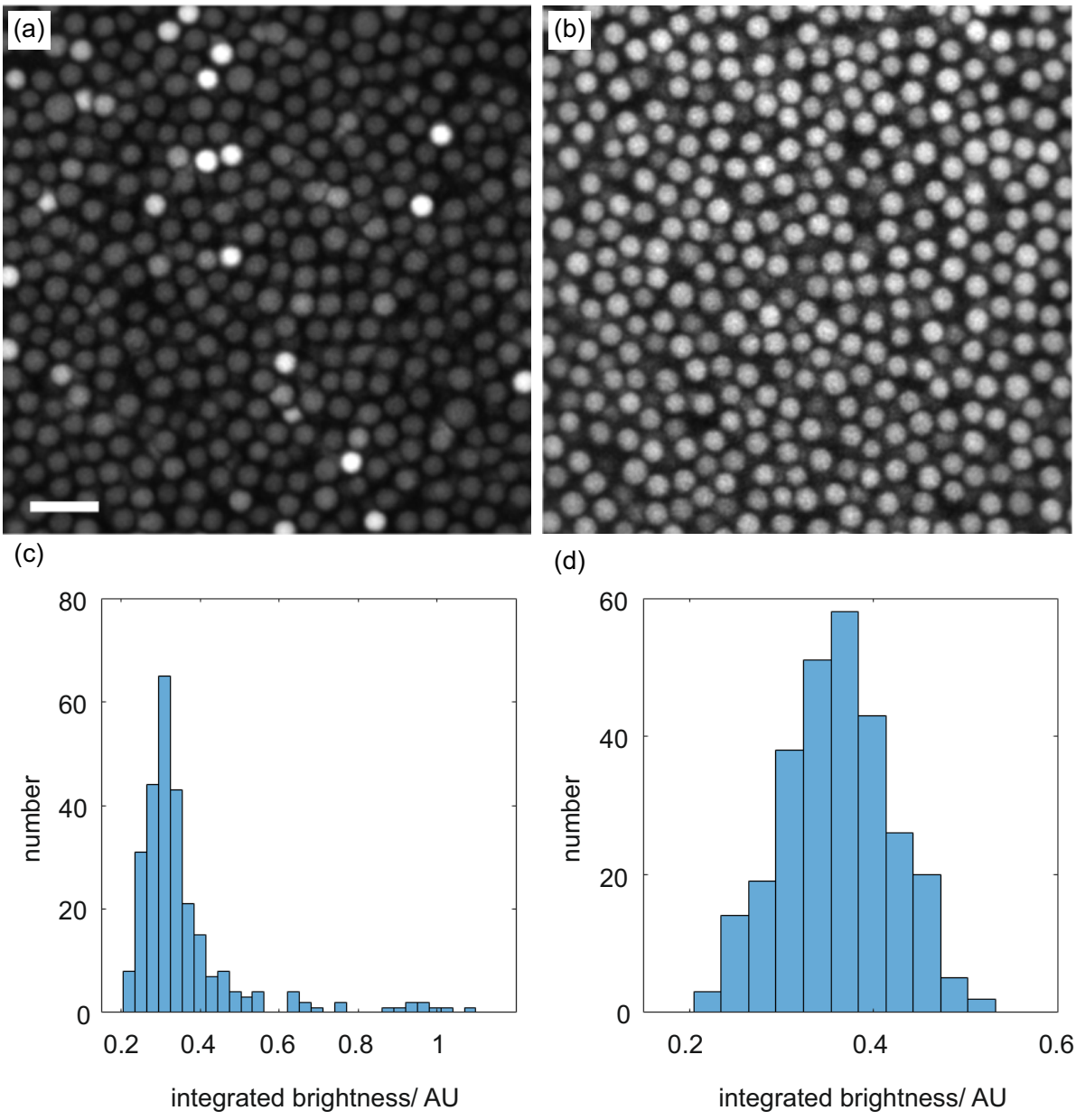


Figure 2.8: (a) and (b) show confocal microscope images of ≈ 2 µm diameter colloidal particles dyed with a RITC-APS in DMSO solution and a RITC-APS acetone solution respectively. Scale bar is 5 µm, and both (a) and (b) have the same scale. (c) and (d) show the distributions of the integrated brightness (in arbitrary units, AU) of the colloidal particles dyed with a RITC-APS in DMSO solution and a RITC-APS acetone solution respectively

The dye solution is prepared as follows, combine 15ml of acetone with 2 mg of rhodamine-B isothiocyanate, RITC and 2 µl of 3-aminopropyl trimethoxysilane, APS and stir in the dark in a closed 25 ml glass vessel for 24 hours to produce rhodamine-B isothiocyanate 3-aminopropyl trimethoxysilane, RITC-APS. The particles are dyed just before they are cross linked. Firstly, 2.02 ml of 5% by weight pluronic F-108 (a sterically stabilising co-polymer) is added dropwise over 5 minutes. After 30 minutes of stirring (600 revolutions per minute), add 400 µl of Acetone RITC-APS dye solution 100 µl at a time at 15 minute intervals. The solution is left to stir for 30 minutes to allow the dye to link with the TPM particles.

2.3.4 Solvent transfer

The second requirement for confocal laser scanning microscopy is refractive index matching of the particles and the suspending medium. The refractive index of TPM can vary from synthesis to synthesis but is always ≈ 1.5 [77]. Mixtures of trichloroethylene, TCE, tetralin, TTL and cis-decalin, DCL, are used to match the refractive index. An approximately 45:55 ratio of TCE:TTL or a 2:3 ratio of DCL:TTL may be used. The density of the TCE/TTL mixture more closely matches the density of the DCL/TTL mixture and is used when a smaller effect of gravity (lower Péclet number) is desired.

Solvent transfer exchanges the liquid phase of the colloidal dispersion and is performed by a series of centrifugation and decanting steps. Care must be taken not to spin the centrifuge too quickly, as irreversible aggregation may occur. Importantly, transfer of colloidal TPM particles with pluronic-F108 grafted to the surface from aqueous to apolar organic solvents requires the intermediate transfer through ethanol. The hydrophilic tails of the F-108 co-ploymer trap a layer of water at the surface, causing irreversible aggregation in apolar solvents. Transfer to ethanol dissolves the water, removing it from the colloidal particle surface. Typically, the solvent transfer involves spinning the colloidal dispersion at 700 g for 7 minutes, removing the supernatant and redispersal in ethanol through vortexing and sonication. This is repeated 5 times and then, the colloidal dispersion is heated in ethanol at 80 °C for 12 hours to dissolve the remaining water. Then, a further two cycles of centrifuging, decanting and re-dispersing in ethanol ensures all water is removed from the particle surfaces. The next steps to transfer into organic solvents follow similarly.

Dispersions of colloidal TPM spheres in pure TTL and DCL are not stable. This is because

the charge on the particle surface is much lower due to the high free energy of ionisation in such apolar solvents, as discussed previously. The charge control agent OLOA (Chevron Chemical Co.) is used to stabilise the particles. TCE is slightly polar, therefore, particles become slightly charged on its addition. A nearly hard sphere potential is achieved with OLOA concentrations between 2% and 5% by weight of solvent in TTL or refractive index matched solutions of TTL and TCE or TTL and DCL. Lowering the OLOA concentration to 0.5% by weight results in a softer more repulsive potential by lowering the charge screening effect possibly due to a lower concentration of inverse micelles in solution. In this thesis two formulations of OLOA are used: OLOA(11,000) and OLOA(1,200). Although the exact composition of each is unknown they behave very similarly in the dispersions of colloidal TPM studied in this thesis.

2.3.5 Colloidal dispersions

Colloidal dispersions with approximately hard sphere interactions are used in this thesis. Specifically, three slightly different dispersions of TPM spheres are condisered. Dispersion A consists of 1.5μm diameter spheres suspended in tetralin, TTL, with 2% by weight OLOA(1,200) charge control agent. In dispersion B, slightly smaller colloidal spheres of 1.4μm diameter are suspended in a refractive index matched dispersion of decalin, DCL, and tetralin in an approximately 2:3 volume ratio. OLOA(11,000), a slightly different formulation, is added to 5% by weight. Dispersions A and B contain colloidal spheres with an approximate hard sphere interaction where the Debye length is much smaller than the diameter of the particles, less than 0.1μm [67, 76]. Dispersion C is similar to B, being suspended in a DCL-TTL mixture, however, with larger and fluorescently labelled (see section section 2.3.3) particles and with the OLOA concentration lower at 0.5% by weight, so that the particles display a longer (but still short) range repulsive interaction. These changes allow for individual particles to be resolved using CLSM. The samples are summarised in table 2.1.

Type	Diameter /μm	p	Interaction	Use	Solvent	[OLOA] /%
A	1.5	0.058	hard sphere like	SAXS	TTL	2
B	1.4	0.049	hard sphere like	SAXS	2 DCL : 3 TTL	5
C	2.1	0.060	soft repulsive	CLSM	2 DCL : 3 TTL	0.5

Table 2.1: Colloidal samples for flow-aligned colloidal crystal experiments, where p is polydispersity.

2.4 Confocal laser scanning microscopy

2.4.1 General principle

Three-dimensional images of colloidal dispersions are produced by confocal laser scanning microscopy, CLSM. The technique is powerful as it enables the resolution of individual colloidal particles, providing detailed local information about colloidal dispersions. This technique combines point-by-point laser illumination with the optical sectioning capabilities of confocal microscopy, a technique first described by Minksy in 1957 [79] where out of focus light is supressed by the use of pinholes. Fig.2.9a shows a ray diagram displaying the principle of optical sectioning. Light from a fluorescing point at the focal point of the objective lens refracts through the objective lens and the tube lens to the conjugate focal point. A pinhole placed at the conjugate focal plane suppresses out of focus light (dotted line), improving the imaging resolution. This principle is included in the setup for an inverted laser scanning confocal microscope, where a pinhole is placed at the conjugate focal plane of imaging as shown in Fig.2.9b. Included in the setup is a point laser source which travels through the optics to excite fluorophores at a (diffraction limited) point in the sample. The emitted light travels through the same optics until a dichroic mirror separates the path of the longer wavelength fluorescence light from the illumination laser light. A 2D raster scan image of the sample is built from imaging different positions of the sample by using a set of scanning mirrors. If the refractive index of the colloidal particles and the suspending medium is the same, the emitted light is not scattered as it leaves the sample, allowing contrast at focal planes deep within the sample. Moving the position of the objective lens along the optical axis, closer to the sample, increases the focal depth (only limited by the working distance of the microscope objective), thus, creating a 3D image.

2.4.2 Experimental microscope setup

The confocal microscopy experiments were carried out using a Thorlabs confocal 8 kHz resonant point scanner mounted on an Olympus IX73 microscope. The microscope was equipped with an Olympus Plan Apochromat oil immersion objective with 60 times magnification and a numerical aperture of 1.42, identical to reference [68]. A typical field of view is 0.1 mm^3.

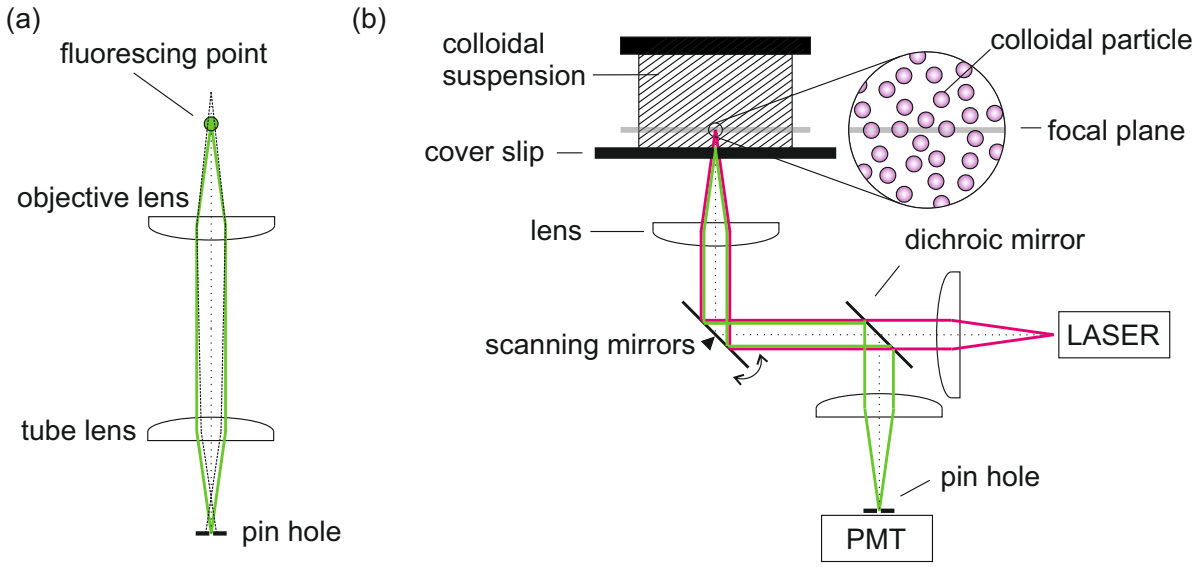


Figure 2.9: (a) Ray diagram showing the principle of optical sectioning. (b) Ray diagram for an inverted confocal microscope allowing imaging of a colloidal sample. The position of the photomultiplier tube is marked as PMT.

2.5 Image analysis

The image analysis techniques described by Crocker and Grier [80] enable the determination of coordinates of bright spots on a dark background. As such, they can be used to find the coordinates of fluorescent particles suspended in a non-fluorescent medium from CLSM images (see Fig.2.10a-c), or diffraction peaks from diffraction images (see Fig.2.10d-f).

The routines firstly perform a high and low band pass filter of the image. The low band pass removes the noise on the length scale of the pixel grid and the high band pass convolutes the image with a Gaussian kernel with width at half height approximately equal to the radius of the spots. This has the effect of smoothing the intensities as shown in Fig.2.10b and e. Secondly the local maxima pixels are identified, those that are surrounded by pixels that are less bright. Finally, coordinates are calculated from a weighted average of the pixels within a user defined radius of each local maximum pixel, where the radius is set just larger than the radius of the bright spot. Fig.2.10c and f show the coordinates overlayed as red cricles on the bright spots in the image. The weighted averages allow coordinates to be found with precision greater than the resolution of the pixel grid [80]. In other words, the coordinates may be at fractional pixel values. Undesirable pixel biasing occurs when the frequency distribution of fractional coordinates is uneven. This shows the influence of the underlying pixel grid on the

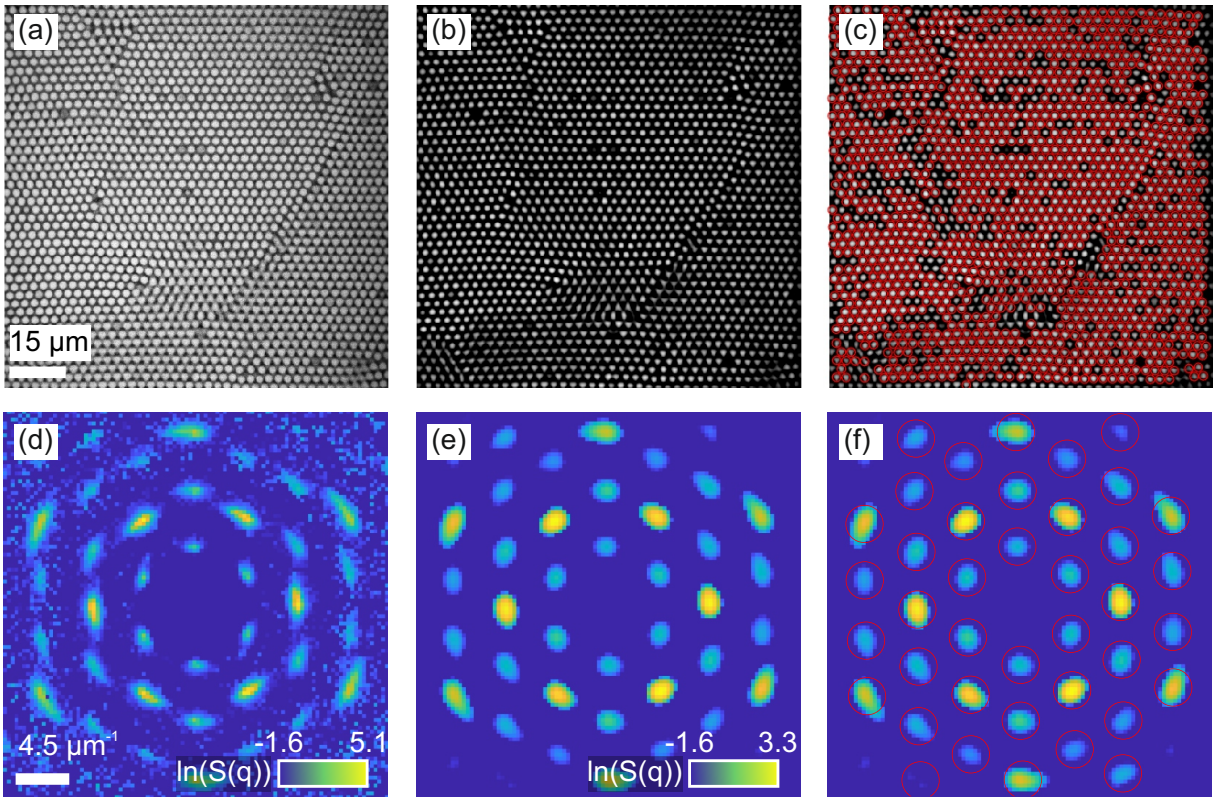


Figure 2.10: (a) 2D (xy) confocal micrsocopy slice of a 3D colloidal crystal composed of ≈2 μm TPM spheres. (b) Band pass filter applied to (a). (c) Features found and overlayed on the band pass filtered image. Note that particles with a z coordinate greater than 1 μm from the xy plane of the image are not plotted. (d) 2D structure factor (see section 3.6.2 for details) for a shear-aligned colloidal crystal as discussed in chapters 3 and 4. Note that the natural logarithm for each pixel value is calculated over which a linear colour map is applied. (e) Band pass filter applied to (d). (f) Peak locations sit at the centre of each red circle. The colour map is identical to panel (e).

bright spot coordinates, thus, limiting the accuracy of the coordinates. Pixel biasing is usually remedied by adjusting the Gaussian kernel width. The Gaussian convolution reduces the pixel bias resulting in more accurate coordinate positions. The integrated brightness of each colloidal particle is calculated from the sum of the pixel values within a user defined radius of the centre of the particle.

2.6 Appendix

2.6.1 Derivation of colloidal crystal scattering intensity

The X-ray scattering intensity is essentially given by the Fourier transform of the electron density [81]. The scattering intensity, $I(\vec{q})$, is proportional to the scattering amplitude multiplied

by its complex conjugate, denoted by $A^*(\vec{q})$, so that:

$$I(\vec{q}) \propto A^*(\vec{q})A(\vec{q}), \tag{2.27}$$

where the scattering amplitude, $A(\vec{q})$, is the Fourier transform of the electron density [71,82]:

$$A(\vec{q}) = \int dV \rho(\vec{r}) e^{-i\vec{q}\cdot\vec{r}}, \tag{2.28}$$

where $\rho(\vec{r})$ is the electron density and $\vec{r}$ is a real space vector. We may write the electron density at $\vec{r}$ as the superposition of electron density of each particle j of the crystal [71]:

$$\rho(\vec{r}) = \sum_{j}^{M} \rho_j(\vec{r} - \vec{r}_j), \tag{2.29}$$

where $\vec{r}_j$ points to the centre of particle j and $\rho_j(\vec{r} - \vec{r}_j)$ defines the contribution of particle j at position $\vec{r}$. The scattering amplitude may then be written as:

$$\begin{aligned} A(\vec{q}) &= \sum_{j}^{M} \int dV \rho_j(\vec{r} - \vec{r}_j) e^{-i\vec{q}\cdot\vec{r}} \\ &= \sum_{j}^{M} \int dV \rho_j(\vec{r} - \vec{r}_j) e^{-i\vec{q}\cdot\vec{r}_j} e^{-i\vec{q}\cdot(\vec{r}-\vec{r}_j)}. \end{aligned} \tag{2.30}$$

This may be rewritten in terms of the form factor amplitude, $f_j(\vec{q})$, so that:

$$A(\vec{q}) = \sum_{j}^{M} f_j(\vec{q}) e^{-i\vec{q}\cdot\vec{r}_j}, \tag{2.31}$$

where f_j, is the Fourier transform of the electron density of member, j, of the crystal:

$$f_j(\vec{q}) = \int dV \rho_j(\vec{p}) e^{-i\vec{q}\cdot\vec{p}}, \tag{2.32}$$

with $\vec{p} = \vec{r} - \vec{r}_j$ [71]. In the case of a colloidal crystal composed of chemically identical colloidal particles, the form factor amplitudes are identical for each member j. Therefore, we may drop the subscript j and write the amplitude in terms of the form factor amplitude, $f(\vec{q})$, and structure factor amplitude, $s(\vec{q})$, in the following manner:

$$A(\vec{q}) = f(\vec{q})s(\vec{q}), \quad \text{where}$$
$$s(\vec{q}) = \sum_{j}^{M} e^{-i\vec{q}\cdot\vec{r}_j}. \tag{2.33}$$

Using equation 2.27, we arrive at an expression for the scattering intensity, here written in terms of the normalised form and structure factors:

$$I(\vec{q}) \propto F(\vec{q})S(\vec{q}), \quad \text{where}$$
$$F(\vec{q}) = f^*(\vec{q})f(\vec{q}), \quad \text{and}$$
$$S(\vec{q}) = \frac{1}{M}s^*(\vec{q})s(\vec{q}). \tag{2.34}$$

Together, the form factor and structure factor account for the spatial distribution of electron density in the colloidal crystal.

Form factor

The form factor describes the contribution of the colloidal particles themselves to the scattering intensity. For colloidal particles the form factor is modelled as scattering from spheres of uniform electron density with equal radius, a. Accordingly, $\rho(\vec{p}) = \frac{C}{V_\mathrm{s}}$, where C is a constant corresponding to the number of electrons in the sphere and $V_\mathrm{s} = \frac{4\pi a^3}{3}$ is the volume of a sphere. As such, the form factor amplitude is evaluated as the Fourier transform:

$$f(\vec{q}, a) = \int dV_\mathrm{s} \frac{3C}{4\pi a^3} e^{-i\vec{q}\cdot\vec{p}}, \tag{2.35}$$

which, normalised to account for electron density and particle volume and ignoring other proportionality constants, is given by the expression:

$$f(\vec{q}, a) = 3\frac{\sin(qa) - qa\cos(qa)}{(qa)^3}, \tag{2.36}$$

where $q = |\vec{q}|$.

Chapter 3

Colloidal crystallisation induced by shear from capillary action

Abstract

We study crystallisation under shear as a result of capillary action. Using confocal microscopy and small angle X-ray scattering, we find that drawing a high volume fraction dispersion of colloidal particles into a flat and narrow capillary creates a large random hexagonal close packed, RHCP, crystal with long-range orientational order over tens of thousands of colloidal particles. We see that shear leaves its fingerprint on the crystal structure by stretching lattice constants along shearing directions. Confocal microscopy reveals detailed local structure with single particle resolution in separate hexagonal close packed and face centered cubic layers. We also examine regions where two walls of the capillary meet, observing that competing shear directions create differently oriented planes of particles. Then, we verify the crystal structure using small angle X-ray scattering goniometer scans. By examining the intensity variation along Bragg rods using Wilson theory [83], we uncover the ratio of face centered cubic to hexagonal close packed within the RHCP structure. We also show that crystallisation is initiated from hexagonal planes forming at the capillary walls, where shear is highest, followed by epitaxial crystal growth from the hexagonal layers acting as templates after shear is stopped. This produces a single orientation RHCP crystal spanning the entire volume of the capillary.

3.1 Introduction

Shear processes arise whenever a fluid travels across a surface or inside a pipe. As such, shear has great significance anywhere liquid is transported, spanning a wide range of fields from food manufacture [84], to the geological study of tectonic plates [85]. Several phenomena are observed during material shear such as shear thickening [86] and thinning [87], where viscosity increases or decreases respectively with shear rate, or shear banding [88, 89], where spatial discontinuities in viscosity arise. Importantly, the action of shear has structural effects on materials with examples including the formation of nano-emulsions [90] and promoting the crystallisation of colloidal dispersions [91].

Often, shearing phenomena arise in complex fluids, where one material is dispersed inside another [92]. Colloidal dispersions are complex fluids that enable the visualisation of the structural perturbation during shear [93–96], shedding light on the mechanisms behind the phenomena. These dispersions contain large micrometer sized particles suspended in a solvent [1] that exhibit slow response times [7] and achieve high Péclet numbers at low shear rates, thus, facilitating the resolution of structures and dynamics at the single particle level using microscopy techniques [3]. Additionally, sheared colloidal dispersions act as a model for sheared molecular systems as molecular dynamics simulations suggest many similarities between colloidal dispersions sheared at modest rates and atomic systems sheared at large rates [97].

Much attention has been given to ordering effects of flow on colloidal dispersions. Shear flow may induce the ordering of anisotropic particles [98–100] with ramifications for ceramic manufacture [98]. Shear flow may also order isotropic particles into crystalline phases [93, 96] and is of particular interest due to the ability to manipulate shear to affect the crystal structure [93, 101], to significantly accelerate crystallisation [91], and to create large domains of coherent orientation and low defect density [102]. These features are often desirable for advanced material applications and are crucial for the fabrication of photonic band gap crystals [103]. However, many of these studies concentrate on structural effects during shear, and do not monitor the effect on crystallisation after shear has stopped.

Many studies couple microscopy with shearing parallel plates [87, 93, 95, 101, 104] to observe structural changes during shear. However, we exploit capillary action through a flat walled capillary to produce shear. The crystallisation mechanism, the crystal structure and the orienta-

tion of the shear-aligned crystals is probed using a combination of small angle X-ray scattering, SAXS, and confocal laser scanning microscopy, CLSM. These techniques provide complementary information at the global and local (single particle) scales, respectively. Confocal microscopy reveals the detailed local structure and orientation of separate hexagonal close packed and face centered cubic layers oriented with shear profiles. We verify the crystal structure using small angle X-ray scattering goniometer scans. Subsequently, using Wilson theory [83], we uncover the ratio of face centered cubic to hexagonal close packed within the RHCP structure from the structure factor variation along Bragg rods. Finally, we use small angle X-ray scattering to characterise crystalline order within and between the hexagonal planes of particles during crystallisation. Thus, we reveal that crystallisation initiates from hexagonal planes of particles sliding over each other at the capillary walls, followed by epitaxial crystallisation to produce a single orientation RHCP crystal spanning the entire capillary volume.

3.2 Theory

3.2.1 Random hexagonal close packed crystal structure

Section 2.2.1 explained how hard sphere colloidal dispersions crystallise into HCP or FCC structures. The difference in free energy between the lower energy FCC and higher energy HCP is very small on the order of $10^{-3}k_{\mathrm{B}}T$ per particle [105]. Therefore, colloidal crystals often contain a mixture of FCC and HCP structures. When the stacking is a random sequence of A, B and C layers, the crystal structure is called random hexagonal close packed, RHCP. A small section of an RHCP crystal containing three hexagonal layers is illustrated in Fig.3.1a. Although this structure may be described by 2D hexagonal lattices with (primitive) lattice vectors $\vec{a}$ and $\vec{b}$, there is no repeated sequence of A, B or C layers normal to the hexagonal planes. Therefore, $\vec{c}$ is defined between hexagonal layers, not between lattice points. Note that $\vec{c}$ is distorted to appear longer for diagram clarity. The lack of periodicity parallel to $\vec{c}$ smears some of the reciprocal lattice points into features called Bragg rods, marked by the grey lines in the reciprocal structure factor illustrated in Fig.3.1b, but other reciprocal lattice points remain as sharp peaks called Bragg spots, marked by the closed black circles. These Bragg spots are at reciprocal lattice positions shared by both the HCP and FCC structures and remain sharp regardless of the stacking sequence. The primitive reciprocal lattice vectors are shown in Fig.3.1b; notice

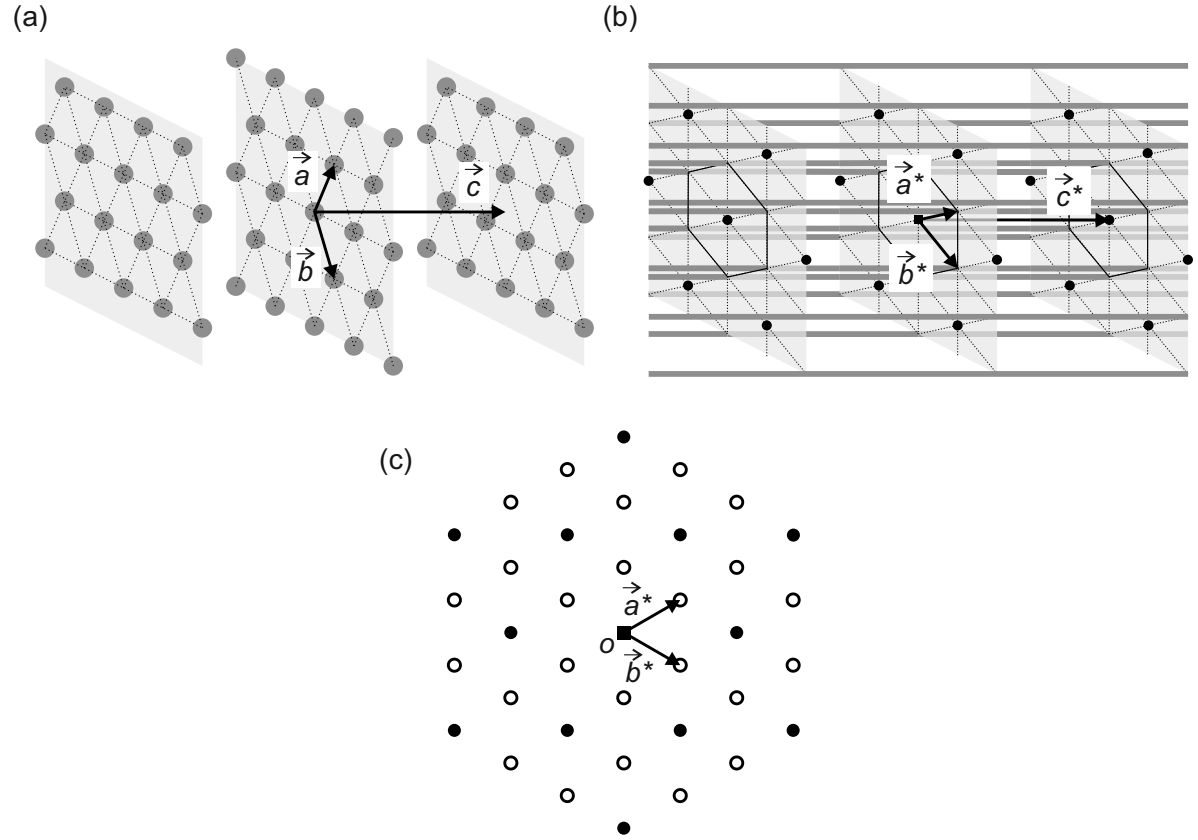


Figure 3.1: (a) Randomly stacked hexagonal layers within an RHCP crystal (here only three are shown). (b) Corresponding reciprocal lattice for a RHCP crystal. The closed black circles correspond to Bragg spots, while the grey lines represent Bragg rods. The origin of reciprocal space is marked by the black square. (c) A perspective view of a section of the reciprocal structure, normal to the planes containing Bragg spots. Open and closed markers represent Bragg rods and spots respectively.

how the primitive lattice vectors $\vec{a^*}$ and $\vec{b^*}$ point towards Bragg rod positions and how $\vec{c^*}$ points between the planes containing hexagonally arranged Bragg spots. A view normal to $\vec{c^*}$ is shown in Fig.3.1c, and shows the spatial relationship between Bragg spots (closed circles) and Bragg rods (open circles) in the $\vec{a^*}\vec{b^*}$ plane. Bragg rods and spots may be distinguished by their Miller indices, h and k. Reciprocal lattice vectors, $\vec{G}_{hkl}$ (equation 2.16), with $h-k \neq 3n$ and $h-k = 3n$ where n is an integer, point to Bragg rods and spots, respectively. Note that for spots, l is an integer, but for rods, l may take intermediate values as they are smeared in reciprocal space.

3.2.2 Quantifying stacking disorder: Wilson theory

The stacking disorder normal to the hexagonal planes affects how the structure factor of the Bragg rods is smeared parallel to $\vec{c^*}$. Wilson theory [83] models the structure factor variation with Miller index l for Bragg rods, $S(l)$. $S(l)$ varies with the stacking parameter α, which varies

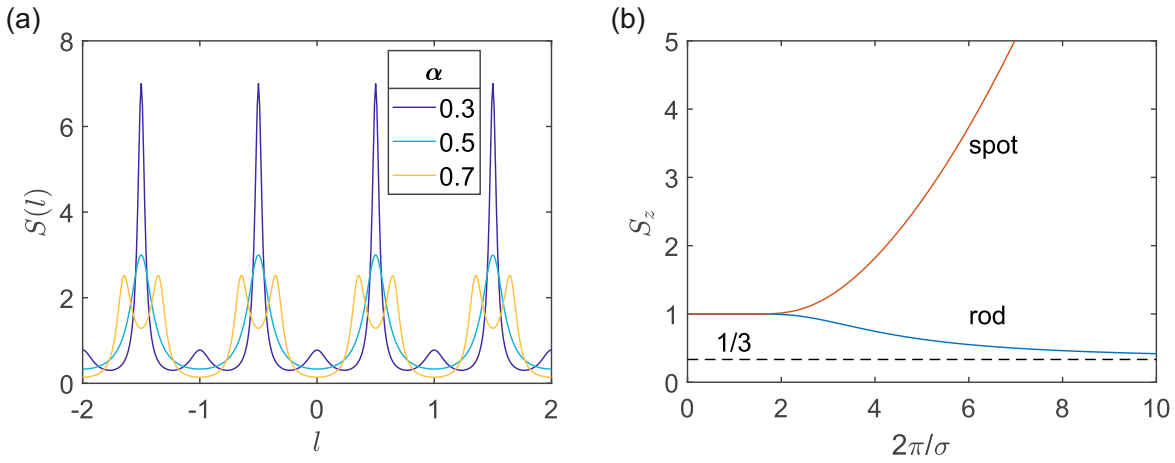


Figure 3.2: (a) Variation of structure factor with Miller index l for Bragg rods for RHCP crystals with various α. (b) Variation of inter-layer structure factor, S_z, (at $l = 0$) with $\frac{2\pi}{\sigma}$ (larger value means more inter-layer order), for Bragg rods and spots.

between $\alpha = 0$ for entirely HCP stacking, through $\alpha = 0.5$ for equal proportions of FCC and HCP (RHCP), to $\alpha = 1$ for entirely (twinned) FCC. $S(l)$ takes the form [83]:

$$S(l) = -1 + \frac{\frac{3}{2}Q_{\mathrm{e}}}{1 - \rho_{\mathrm{E}} \exp(2i\pi l)} + \frac{\frac{3}{2}Q_{\mathrm{e}}}{1 - \rho_{\mathrm{E}} \exp(-2i\pi l)} + \frac{\frac{3}{2}Q_{\mathrm{o}}}{1 - \rho_{\mathrm{O}} \exp(2i\pi l)} + \frac{\frac{3}{2}Q_{\mathrm{o}}}{1 - \rho_{\mathrm{O}} \exp(-2i\pi l)}, \tag{3.1}$$

where

$$Q_{\mathrm{e}} = \frac{1 + 2\rho_{\mathrm{O}}}{3(-\rho_{\mathrm{E}} + \rho_{\mathrm{O}})} \quad \text{and}$$
$$Q_{\mathrm{o}} = \frac{1 + 2\rho_{\mathrm{E}}}{3(-\rho_{\mathrm{O}} + \rho_{\mathrm{E}})}, \tag{3.2}$$

where

$$\rho_{\mathrm{E}} = \frac{1}{2}\left(-\alpha + \sqrt{4 - 8\alpha + \alpha^2}\right) \quad \text{and}$$
$$\rho_{\mathrm{O}} = \frac{1}{2}\left(-\alpha - \sqrt{4 - 8\alpha + \alpha^2}\right). \tag{3.3}$$

Fig.3.2a shows three curves for Bragg rods at different values of α. The peaks change their position and height with α. In section 3.4.1, this model is used to calculate the proportion of HCP to FCC stacking in the flow-aligned colloidal crystals.

3.2.3 Lateral displacement of hexagonal layers: modified Wilson theory

We may modify Wilson theory to account for correlations between the translational positions of successive hexagonal layers along z. In other words, we account for the discrepancy in plane translation for successive A layers, n layers apart. To this end, the structure factor may be split into the contributions:

$$S(\vec{q}) = S_z(\vec{q})S_{||}(\vec{q}), \tag{3.4}$$

where $S_z(\vec{q})$ and $S_{||}(\vec{q})$ are the inter-layer and intra-layer structure factors respectively. Intra-layer order increases as particles in hexagonal layers align more closely with a 2D hexagonal lattice and as the number of parallel hexagonal layers increases. This increase in order results in an increase in $S_{||}(\vec{q})$ for both Bragg rods and spots at integer values of h and k. Inter-layer order increases when the correlations between successive A, B or C hexagonal layers increases. In other words, when the lateral positions of successive A layers (or B or C) becomes more similar. For Bragg rods and spots in an RHCP crystal with $\alpha = 0.5$ and at $l = 0$, this increase in inter-layer order has opposing effects on the structure factor. For Bragg rods, the inter-layer structure factor at $l = 0$ is:

$$S_z^{\text{rod}} = \frac{2 - \exp(-\frac{\sigma^2}{2})}{2 + \exp(-\frac{\sigma^2}{2})}, \tag{3.5}$$

and for Bragg spots:

$$S_z^{\text{spot}} = \frac{1 + \exp(-\frac{\sigma^2}{2})}{1 - \exp(-\frac{\sigma^2}{2})}, \tag{3.6}$$

where the parameter, σ, quantifies the inter-layer disorder, and is the standard deviation in lateral displacement of a hexagonal layer in a random direction within the layer (see appendix 3.6.1 for more details). A decrease of σ results in an increase of S_z^{spot} and a decrease for S_z^{rod}, as shown in Fig.3.2b. For Bragg rods, S_z^{rod} decays to $\frac{1}{3}$ for an RHCP ($\alpha = 0.5$) crystal containing hexagonal layers perfectly arranged in A, B or C lateral positions. A derivation for the above is found in appendix 3.6.1.

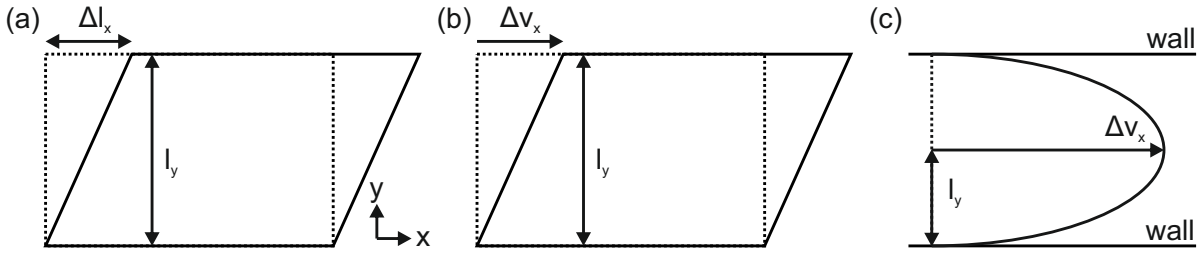


Figure 3.3: Illustration of (a) shear strain, γ, (b) shear strain rate, γ', and (c) flow inside a container with parallel walls.

3.2.4 Shear strain

In this chapter, we study shear induced colloidal crystallisation and here we introduce the key concepts. Shear strain, γ, is the strain component co-planar with the cross section of a material, as illustrated in Fig.3.3a. The shear strain rate, γ', is the first derivative of the shear strain with respect to time. It may be thought of as difference in velocities over a normal direction, as illustrated in Fig.3.3b. Shear strain is dimensionless whereas shear strain rate has dimensions of s^{-1} and are defined as:

$$\gamma = \frac{\Delta l_x}{l_y} \quad \text{and}$$
$$\gamma' = \frac{\Delta v_x}{l_y}, \tag{3.7}$$

where Δl_x is change in length normal to l_y and where Δv_x is change in velocity normal to l_y, as illustrated in Fig.3.3a and b. Material flow in a container with non-slip boundary conditions, where material at the wall is stationary, produces shear in the material. Flow between two flat parallel walls of a capillary is illustrated in Fig.3.3c, where the parabolic flow profile creates shear, similarly to in Fig.3.3b. Note that this flow profile creates a greater shear rate at the walls to that in the centre of the container. Key directions in three-dimensional shear flow are the velocity, velocity gradient and vorticity directions. In Fig.3.3b and c these directions are parallel to the x, y and z (out of the plane of the page) directions, respectively.

3.3 Methods

3.3.1 Colloidal samples

The colloidal TPM dispersions type A, B and C (see section 2.3.5) are used in this study.

3.3.2 Flow-aligned crystal preparation

High volume fraction, $\phi \approx 0.4$, colloidal dispersions are produced by spinning down the colloidal dispersion in a centrifuge. Approximate volume fractions are achieved by assuming the sediment of colloidal particles is randomly packed with a volume fraction of $\phi = 0.64$ [106]. As much supernatant as possible is removed before measuring the mass of sediment. Then, the additional volume of supernatant needed to produce a target volume fraction is calculated from the mass density of the solvent and the TPM particles. Details for the calculation are found in appendix 3.6.4. Note that the volume fraction within the capillary is also measured from lattice constant and particle size measurements as explained later.

The colloidal sediment is re-suspended using sonication with ultrasound and vortexing. Next, a capillary with internal dimensions of 0.1 mm by 2 mm by $\approx$ 30 mm is filled with the dispersion. The capillary is placed into the colloidal dispersion which enters by capillary action. The capillary is kept approximately horizontal to mitigate the slowing effect of gravity on the advance of the dispersion. The ends of the capillary are subsequently sealed with two component epoxy glue. A photograph of an example crystal inside a capillary is shown Fig.3.4d, where Bragg scattering is clearly visible owing to the presence of crystalline planes. The colloidal dispersion takes $\approx$ 25 s to fill a capillary $\approx$ 30 mm in length. Using, $l_y = 0.05$, $\Delta v_x = 1.18$ mms^{-1} (see equation 3.7) and a fluid viscosity equal to the viscosity of tetralin, $\eta = 2 \times 10^{-3}$ Pa s, the shear Péclet number is calculated to be $P_e = 18$, using equation 2.5. This is much greater than unity, showing that flow dominates Brownian motion during capillary filling.

3.3.3 Crystal structure determination

Both small angle X-ray scattering, SAXS, and confocal microscopy, CLSM are used to reveal the three-dimensional crystal structure and its orientation within the capillary. The structural

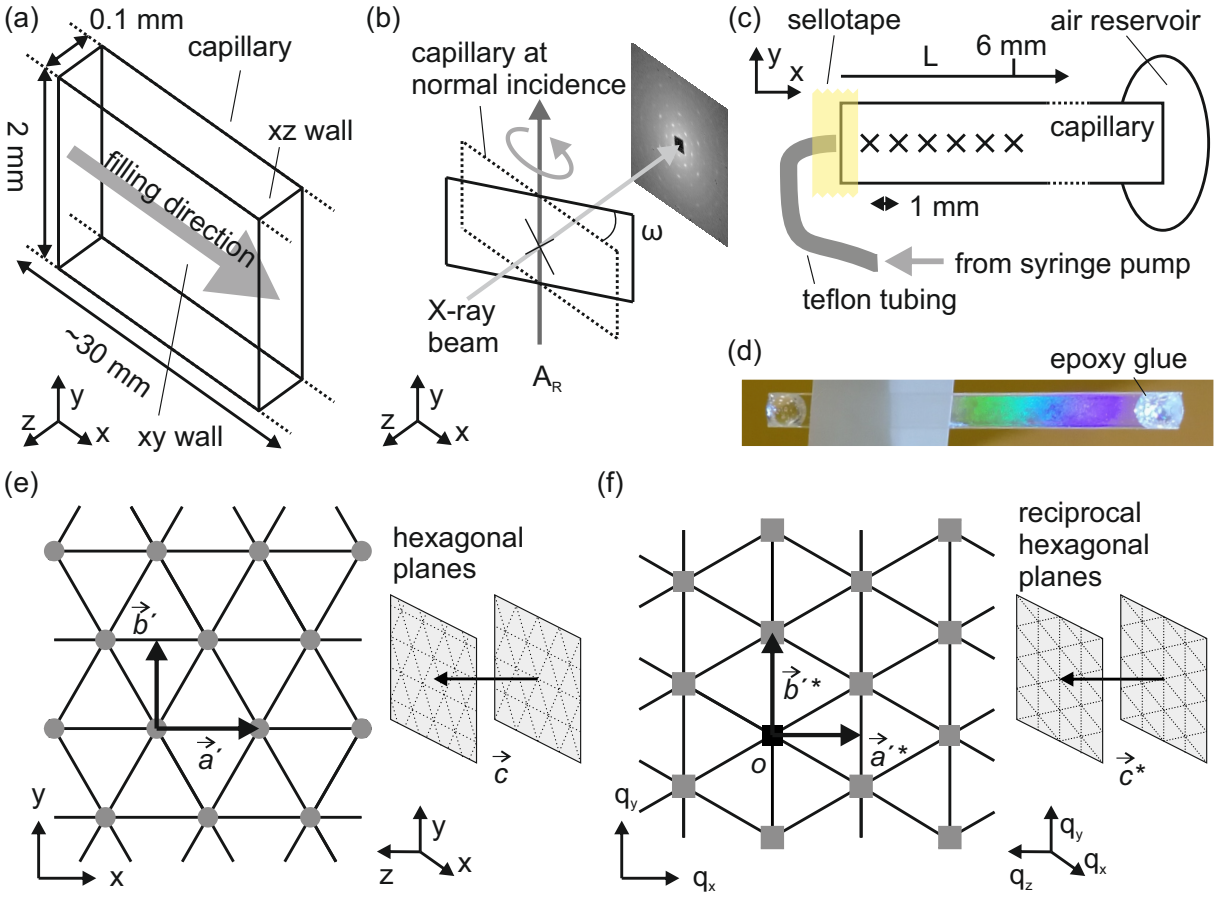


Figure 3.4: (a) Schematic of the dimensions of the capillary and the attached laboratory frame where the x axis points along the direction of filling. (b) Setup for the goniometer scan showing the geometric relationship between the X-ray beam, the rotation axis, A_{R}, and the capillary. For normal incidence, $\omega = 0°$. The detector position is represented by the diffraction pattern in the top right. (c) Setup for imaging during crystallisation. The irradiated positions are marked by the black crosses. (d) The external appearance of a flow-aligned crystal where the Bragg scattering is clearly visible as a spectrum of colours. (e) and (f) show the real and reciprocal lattices respectively. Alternative lattice and reciprocal lattice vectors respectively are marked, which are parallel to the real and reciprocal laboratory frame axes shown in the bottom left corners (a 2D unit cell is created by a' and $2b'$).

parameters that are measured are lattice constants, defined below, and the stacking parameter, α, as defined previously. SAXS and CLSM are complementary techniques as SAXS provides average information over a large field of view, whereas CLSM provides particle level resolution but at a smaller field of view.

The three-dimensional structure in reciprocal space of a crystal composed of a $\phi = 0.42$ type A colloidal dispersion is measured using SAXS. Each two dimensional small angle diffraction image shows a slice through reciprocal space. By taking many slices at different angles of incidence, the three-dimensional reciprocal structure may be revealed. This is achieved by a goniometer scan, for which the experimental set up is illustrated in Fig.3.4b. The X-ray beam travels through the crystal (contained within the capillary) to produce a diffraction pattern on a detector. The capillary is rotated around the axis A_{R} through a range of angles $-70^{\circ} \leq \omega \leq 70^{\circ}$ where ω is the angle the capillary makes with the normal X-ray incidence plane, and diffraction images are taken every 1°. Goniometer scans are performed over a 3×3 square grid or irradiation positions over 1 mm^2 area. A background goniometer scan of a capillary containing no colloidal particles but just solvent is subtracted from each image, we do not take a dark image. Reciprocal space is calibrated using the diffraction pattern of dry rat tail collagen [107]. Then, a calculated form factor is removed from each image to reveal the structure factor in 3D. Details of the method are found in appendix 3.6.2. The experiments were carried out during two experimental sessions at the experimental beam line, B-16, at Diamond Light Source, Didcot, UK. Preliminary experiments were carried out at the Dutch-Belgian beam line, BM26, at ESRF in Grenoble, France.

The three-dimensional structure in real space of crystals composed of a $\phi = 0.37$ type C colloidal dispersion is found using the CLSM set up described in section 2.4.2. The step size in z was set to be the same as the pixel size in x and y to ensure cubic voxels which simplifies the analysis. The axial aberrations are negligible because the difference in refractive index between the glass of the sample container, the microscope objective immersion oil, and the colloidal dispersion (all ≈ 1.5) is small, further simplifying the construction of particle coordinates. From the microscopy images, the particle coordinates are identified using the Crocker-Grier method as explained in section 2.5. HCP and FCC structures were identified locally using the method detailed in chapter 5, which finds whether HCP or FCC is the best match for the first coordination shell of each particle. If neither is a good match, the particle is

assigned as neither and is considered amorphous (fluid-like structure).

Lattice constants

Lattice constants are lengths of lattice vectors. For chapters 3 and 4, it is worthwhile defining constants from lattice vectors whose directions are parallel to the dimensions of the capillary as oriented in the laboratory frame. The capillary is oriented in the laboratory frame as illustrated in Fig.3.4a where x is parallel to the direction of filling to which y and z are both normal. Therefore, the large flat walls of the capillary are the xy walls, and the smaller, narrower walls are the xz (see Fig.3.4a). The lattice vectors are shown in Fig.3.4(e) where $\vec{a'}$ and $\vec{b'}$ are parallel to the laboratory frame axes, x and y, respectively. The lattice constants a', b' and c, are the lengths of $\vec{a'}$, $\vec{b'}$ and $\vec{c}$ respectively. The dashes indicate that $\vec{a'}$ and $\vec{b'}$ do not point in the same direction as the conventional primitive lattice vectors $\vec{a}$ and $\vec{b}$, as shown in Fig.3.1a. Lattice constant $\vec{c}$ has no dash as it points in the same direction as convention: between hexagonal planes of particles, as shown in Fig.3.1a. From CLSM measurements, these lattice constants are calculated from the vectors of the nearest neighbours relative to the central particle, as described in appendix 3.6.3a. Since $\vec{a'}$ and $\vec{b'}$ and $\vec{c}$ (see Fig.3.4e) are orthogonal to each other, equation 2.15 simplifies and lattice constants can be calculated from reciprocal lattice constants from SAXS images using:

$$a' = \frac{2\pi}{a'^*}, \quad b' = \frac{2\pi}{b'^*}, \quad c = \frac{2\pi}{c^*}, \tag{3.8}$$

where $\vec{a'^*}$ and $\vec{b'^*}$ are illustrated in Fig.3.4f. The constants a' and b' and c are calculated from the coordinates of the structure factor peaks from the goniometer scans as described in appendix 3.6.3b.

Stacking parameter

The stacking parameter, α, may be measured from both the SAXS goniometer scans and from confocal microscopy. From confocal microscopy, α, is the ratio of the number of locally FCC particles to locally HCP particles:

$$\alpha = \frac{N_{FCC}}{N_{HCP} + N_{FCC}}. \tag{3.9}$$

From the SAXS goniometer scans, α is measured from structure factor variations of Bragg rods with Miller index l, calculated following the method in appendices 3.6.2 and 3.6.3. For each Bragg rod, the stacking parameter, α, satisfies:

$$\min_{\alpha,M} \sum_{i}^{N} (G(\alpha, l_i) - S_{\mathrm{m}}(l_i))^2, \quad \text{where,}$$
$$G(\alpha, l_i) = MS(\alpha, l_i), \tag{3.10}$$

where $S(\alpha, l_i)$ is defined in equation 3.1, where $S_{\mathrm{m}}(l_i)$ is the structure factor at one of N l_i values from the goniometer scan and where M is a scaling factor accounting for experimental conditions such as X-ray source intensity, illuminated volume and detector distance.

3.3.4 Crystallisation mechanism

Finally, we characterise the crystallisation mechanism. To this end, diffraction patterns were observed as a $\phi \approx 0.4$ type B colloidal dispersion entered the capillary and for a short time afterwards during crystallisation. A syringe pump pushed the colloidal dispersion through teflon tubing until it reached the entrance of the capillary. The dispersion then entered the capillary by capillary action, until the flow stopped when the capillary was full of the dispersion, taking roughly 25 s. There was no tight seal between teflon tubing and the capillary to prevent the pump from pushing the solution out the other end of the capillary. A large reservoir of air prevented the hazardous solvent vapour escaping but provided minimal resistance to fluid entering the capillary. Diffraction patterns were taken at normal incidence over six positions in x near the entrance of the capillary and were spaced 1mm apart half way up the capillary height in y, as shown in Fig.3.4c. The distance L is measured from the capillary entrance. Each exposure was 1 s, allowing for quick cycle through the measurement positions by translating the capillary on a stage. The structure factor is calculated from the diffraction patterns as described previously.

3.4 Results and discussion

3.4.1 Crystal structure and orientation

The flow-aligned crystals show striking iridescent Bragg scattering where the colour varies smoothly with viewing angle due to a single crystal orientation (see Fig.3.4d). The lattice constants, stacking parameter and crystal orientation within the capillary are measured using CLSM and SAXS, revealing a random hexagonal close packed, RHCP, crystal structure with a single orientation on the order of $\approx 1 \times 10^4$ particle diameters.

Confocal microscopy measurements

The local structure of the crystal is probed by CLSM where several fields of view (0.001 mm^3) were imaged. Fig.3.5a shows the typical appearance of an xy plane in the bulk of the crystal. This image shows that the hexagonal planes of the crystal are parallel with the xy laboratory frame where the 2D hexagonal lattice orientation has $\vec{a'}$ and $\vec{b'}$ parallel to laboratory frame axes x and y respectively, as shown in Fig.3.4e. The appearance is the same at other depths in z and fields of view. This observation agrees with several other studies where shear of colloidal dispersions results in hexagonal planes aligning within the velocity vorticity (here xy) plane [95,104,108–112] with the close packing direction parallel to the velocity (x) direction corroborating previous observations at high shear [104, 108–110, 113]. Fig.3.5b shows a reconstruction of the particle coordinates for a field of view in the centre of the capillary spanning the entire internal 0.1 mm length in z. The arrangement is typical and is reproduced in other fields of view. The FCC or HCP are coloured in blue or red respectively and create stripes of alternating colour along the yz and xz faces showing changes in stacking sequence normal to the xy plane. The stacking parameter is measured as $\alpha = 0.54$, revealing a RHCP structure with slight preference for FCC. This preference for FCC may be due to slight mechanical perturbations during the transport of the crystals to the microscope and during mounting, as observed by Martelozzo et al. [114] in similar RHCP colloidal dispersions.

The high spatial resolution of CLSM enables detailed imaging at a field of view close to the xz walls of the capillary. A perspective looking along the filling direction (see Fig.3.4a) is shown in Fig.3.5c. Here, the orientation of the hexagonal layers changes to be parallel to its

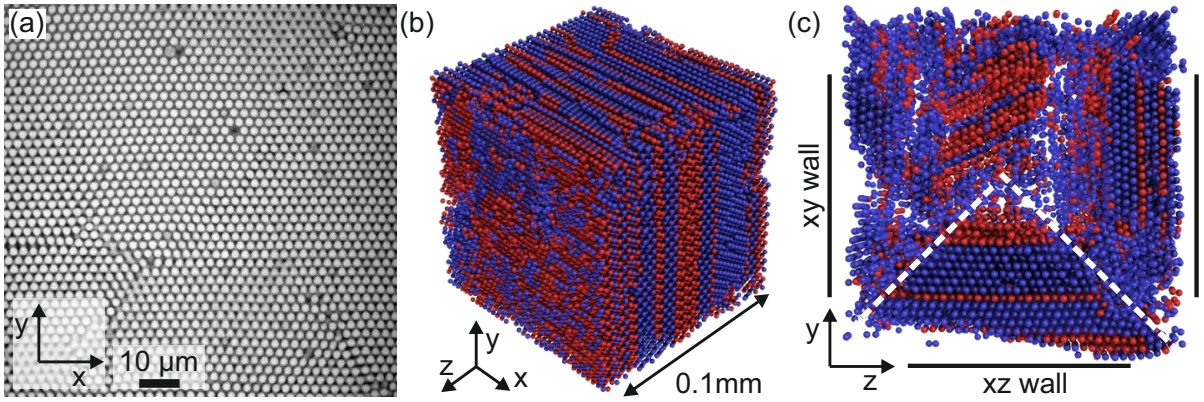


Figure 3.5: (a) CLSM image of colloidal crystal in the xy plane. (b) Shows a reconstruction of the colloidal particles in the centre of the capillary from their coordinates obtained using CLSM. Particles with FCC and HCP local environment are marked in blue and red respectively. (c) Shows a volume at the edge of the capillary. The perspective has been modified to more easily see how the hexagonal layers are aligned.

closest wall; the dotted lines mark the change in hexagonal plane orientation and are at 45° to the walls. This shows that the hexagonal layers align wherever the shear rate is highest. The high confinement along z (0.1mm) and large, flat xy walls results in the alignment parallel to the xy planes dominating the hexagonal plane orientation. Another hexagonal plane orientation exists at the top middle of Fig.3.5c, possibly due to competing epitaxial growth orientations from the two wall orientations.

The lattice constants, as defined in Fig.3.4e, are measured as $a' = 2.5898 \pm 2 \times 10^{-4}$ μm, $b' = 2.3231 \pm 2 \times 10^{-4}$ μm and $c = 2.1513 \pm 2 \times 10^{-4}$ μm, where the error is the standard error (details in appendix 3.6.3). For an RCHP crystal with isotropic nearest neighbour separation, the lattice parameters should have the ratios $\frac{b'}{a'} = \frac{\sqrt{3}}{2}$ and $\frac{c}{a'} = \sqrt{\frac{2}{3}}$. However, the observed ratio $\frac{b'}{a'} > \frac{\sqrt{3}}{2}$ and $\frac{c}{a'} > \sqrt{\frac{2}{3}}$. The higher ratios show that the crystal structure is stretched in z and y, consistent with the notion of crystallisation via shear where hexagonal planes slide over one another to increase c and where lines of particles within the hexagonal planes slide over each other to increase b'. Using a particle radius of 1.05μm (see table 2.1 type C) and the lattice constants above, $\phi = 0.37$. It is likely that the volume fraction of the fluid-crystal coexistence region is suppressed below $\phi_\chi = 0.49$ due to the short range repulsions on the TPM particles [76], supported by the fact that these crystals persist indefinitely within the capillary once formed.

SAXS measurements

Next, we characterise the crystal structure using SAXS. Fig.3.6a shows the 2D scattering intensity image at $\omega = 0$, i.e. the X-ray beam is normal to the xy walls of the capillary for a type A (see table 2.1) colloidal crystal. The Bragg spots and rods show the same hexagonal arrangement as shown in Fig.3.1c, revealing that the hexagonal planes of particles are parallel to the xy walls (see Fig.3.4). The orientation of the reciprocal lattice within the planes shows that $\vec{a'^*}$ and $\vec{b'^*}$ are parallel to the reciprocal laboratory frame axes q_x and q_y, respectively (see Fig.3.4f)

The full 3D structure of the crystals is revealed using many 2D slices through reciprocal space from SAXS goniometer scans. Example 2D slices of the structure factor at normal incidence, $\omega = 0°$, and at $\omega = -32°$ are shown in Fig.3.6b and c, respectively. Several Bragg spots with the same h and k at different l indices are visible in these two images; the 110 and 111 spots are marked as examples. Fig.3.6d shows the variation of $S(\vec{q})$ against q_z for $11l$ Bragg spots from a goniometer scan. The local maxima define the q_z coordinates of the Bragg spots, which are plotted in 3D in Fig.3.6f. The orientation of the Bragg spots is equivalent to the orientation seen in the CLSM image in Fig.3.5b.

To measure the stacking parameter, α, the variation in the structure factor as a function of l, $S(l)$, is measured for Bragg rods (see appendix 3.6.2 for details). An example $S(l)$ variation for a Bragg rod is shown in Fig.3.6e. The solid line represents the measured $S(l)$ and the dotted lines show the fit with Wilson theory with α and M that satisfy equation 3.10. The mean stacking parameter, $\alpha = 0.55 \pm 0.04$, reveals a RHCP structure with a slight preference for FCC, agreeing with the measurements from CLSM. Note that goniometer scans of similarly prepared crystals exhibit similar α values, slightly greater than 0.5. Once again, the FCC preference may be a result of the mechanical perturbations during transport and mounting of the sample for imaging.

From the goniometer scans, we also determine the lattice constants which are measured to be $a' = 1.796 \pm 0.004$ µm, $b' = 1.567 \pm 0.007$ µm and $c = 1.488 \pm 0.004$ µm. The errors are the standard error calculated as described in appendix 3.6.3. Once more, the ratios are larger than the values for perfect RHCP crystals; $\frac{b'}{a'} > \frac{\sqrt{3}}{2}$ and $\frac{c}{a'} > \sqrt{\frac{2}{3}}$, due to the stretching effect of shear along the $\vec{b'}$ and $\vec{c}$ lattice directions, supporting the observation from CLSM. Using a particle

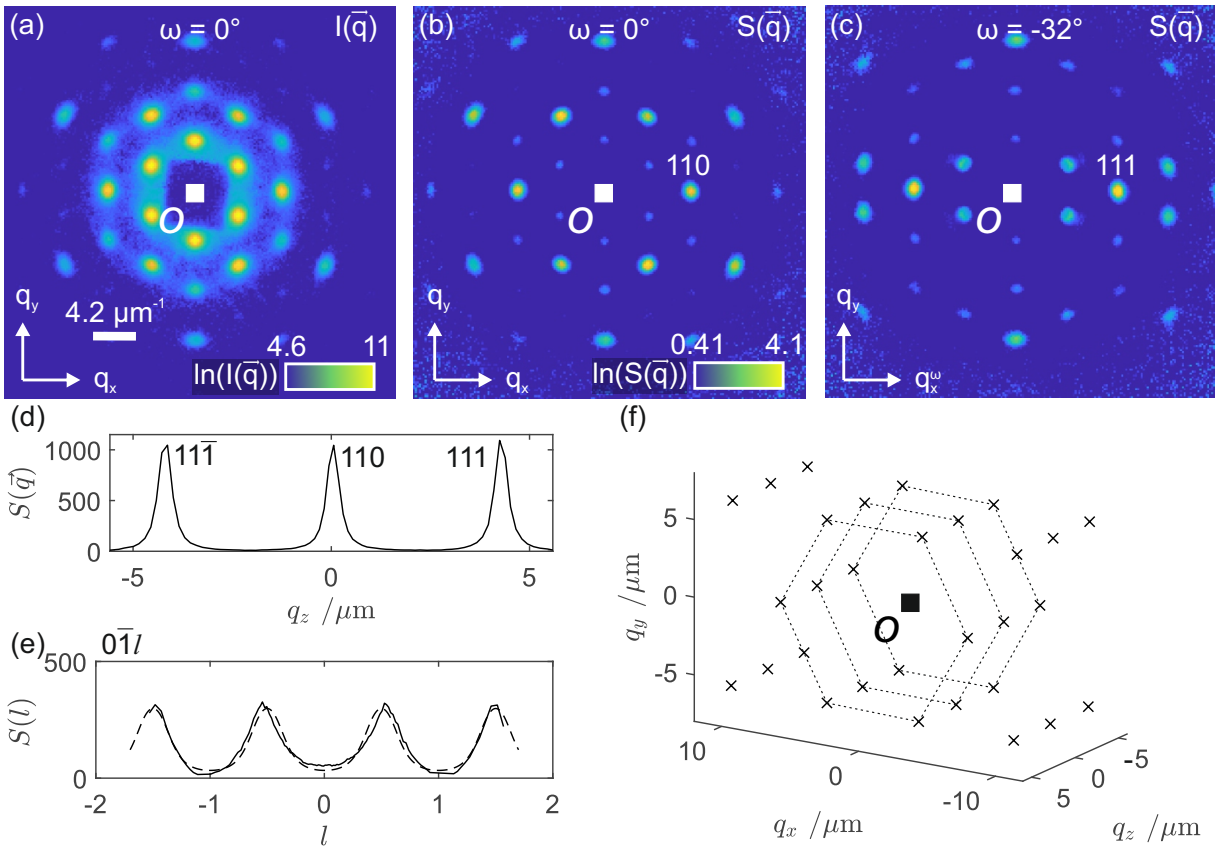


Figure 3.6: (a) 2D $I(\vec{q})$ diffraction image at $\omega = 0°$. (b) and (c) 2D $S(\vec{q})$ at $\omega = 0°$ and $\omega = -32°$ respectively. The colours are plotted on a logarithmic scale; (b) and (c) share the same colour map. The white squares in (a), (b) and (c) mark the origin of reciprocal space. (d) $S(\vec{q})$ variation with q_z for a $11l$ Bragg spot where each peak corresponds to the spot position. (e) Shows $S(l)$ variation with l for a $0\bar{1}l$ Bragg rod as the solid line. The dotted line shows the Wilson theory curve for calculated α and M. (f) 3D arrangement of Bragg spots uncovered from the goniometer scan. The dotted lines connect first order spots in the same q_xq_y plane (same l) to guide the eye and the black square marks the origin of reciprocal space. Note that the spots at $q_x = q_y = 0$, $q_z = \pm\frac{2\pi}{c}$ are not present as a consequence of the limited goniometer scan angles.

radius of 0.75 μm (see table 2.1 type A), and the lattice constants measured from the SAXS goniometer scans, we calculate the volume fraction as $\phi = 0.42$. Again, due to the charge and the persistence of the crystals, this is likely above the fluid-solid co-existence volume fraction. As with all crystals prepared in the way described above, the volume fraction is slightly higher than the target volume fraction during sample preparation.

3.4.2 Structure evolution during crystallisation

The mechanism of crystallisation was examined by measuring SAXS diffraction patterns as the colloidal dispersion entered and flowed through the capillary. To this end, diffraction images were taken at normal incidence at several distances, L, from the capillary entrance, as shown

in Fig.3.4c, during capillary filling. The structure factor, $S(\vec{q})$, was extracted from diffraction images by dividing by the form factor (see appendix 3.6.2 for details). The structure factor at $L = 6$ mm, shortly after the solution entered the capillary at $t = 5.1$ s is shown in Fig.3.7a. Note that the solution takes $t \approx 5$ s to travel 6 mm inside the capillary. The concentric rings around the centre of reciprocal space indicate an amorphous arrangement of particles. Subsequently, peaks appear quickly within several seconds as the particles begin to crystallise under shear. At $t \approx 25$ s, flow in the capillary stops as the dispersion reaches the other open end of the capillary. A snapshot of the structure factor shortly after shear stops at $t = 3.1$ minutes is shown in Fig.3.7b. The diffraction peaks show that crystallisation with hexagonal symmetry has occurred. The innermost, primary ring is still visible at low q in the structure factor showing that both crystalline and liquid like arrangements of particles co-exist. This means that the shear initiated during capillary action is not great enough to promote crystallisation throughout the capillary. It is likely that the hexagonal layers form at the xy walls of the capillary, where shear is highest, similarly to the observations in CLSM studies of colloidal crystallisation under shear [95]. Gradually, the ring disappears and the existing peaks become clearer and more numerous at high q as the dispersion crystallises throughout the capillary, as shown in the late time structure factor in Fig.3.7c.

Next, we characterise the inter and intra-layer ordering of the hexagonal layers during crystallisation. We do so through examination of the structure factor over time. Fig.3.7d shows the time dependence of Bragg spots with t for several L positions. Here, $\langle S^{\mathrm{spot}} \rangle$ is the mean integrated structure factor peak intensity for the 1^{st} order Bragg spots, as marked in Fig.3.7c. Figure 3.7d shows that as time evolves, the Bragg spot structure factor increases, and does so similarly for all positions in the capillary. This suggests either an increase in inter-layer ordering, where the translational positions of A, B and C layers become more established, or an increase in intra-layer ordering, where the particles within a hexagonal layer align more closely with the hexagonal lattice, or both. Recall that an increase in inter or intra-layer order increases the value of the inter or intra-layer structure factors S_z^{spot} or $S_{||}^{\mathrm{spot}}$, respectively (see equation 3.6 and Fig.3.2b), and therefore, increases the Bragg spot structure factor (at $l = 0$) so that $S^{\mathrm{spot}} = S_z^{\mathrm{spot}} S_{||}^{\mathrm{spot}}$ (see equation 3.4). We see evidence for intra-layer ordering from the formation of hexagonally arranged diffraction peaks as time progresses, as shown in Fig.3.7a-c. Note that the duration of the $\langle S^{spot} \rangle$ plots are shorter for lower L positions because glue from the sellotape fixing between the teflon tube and the capillary dissolved and diffused into the

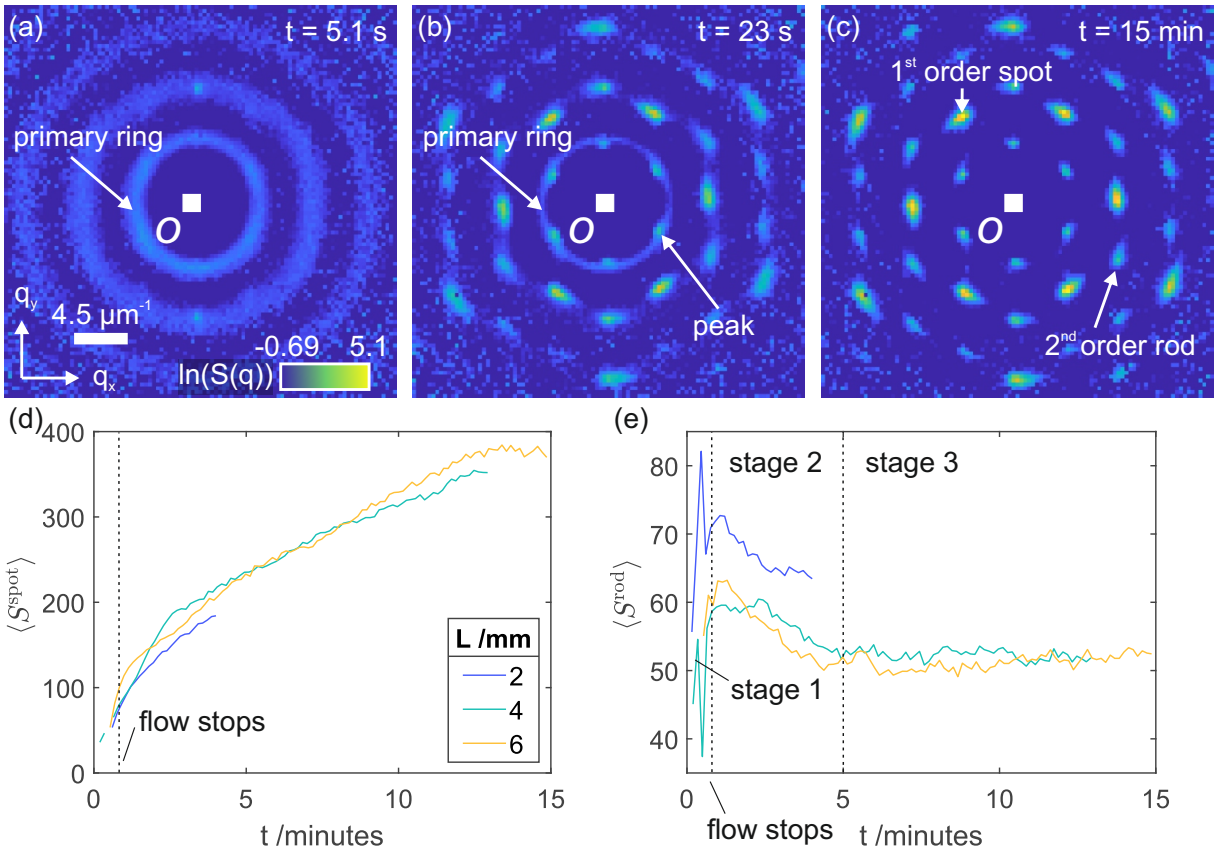


Figure 3.7: (a), (b) and (c) show 2D structure factors for flow-aligned crystallisation at $L = 6$mm at successive times. (d) Variation in the average structure factor for first order Bragg spots, $\langle S^{\text{spot}} \rangle$, with time t. (e) Variation in the average structure factor for second order Bragg rods, $\langle S^{\text{rod}} \rangle$, with time t.

capillary. As the glue reached higher L over time, it caused a depletion interaction disrupting the crystalline order. Any affected positions were discarded from the analysis.

To examine the inter-layer ordering, we measure the structure factor for Bragg rods, as plotted in Fig.3.7e. Here, $\langle S^{\text{rod}} \rangle$ is the mean integrated structure factor peak intensity for the 2$^{\text{nd}}$ order Bragg spots, as marked in Fig.3.7c. Three distinct stages are observed in the Bragg rod structure factor. Firstly, between $t = 0$ s and $t \approx 25$ s, the structure factor increases sharply, secondly, between $t \approx 25$ s and $t = 5$ minutes, it decreases before thirdly, from $t = 5$ minutes onward, it reaches a plateau. These stages are a consequence of the competition between the opposing effects of increasing inter and intra-layer order on the Bragg rod structure factor, $S^{\text{rod}} = S_z^{\text{rod}} S_{||}^{\text{rod}}$ (see equation 3.4). An increase in inter-layer order decreases the inter-layer structure factor for Bragg rods, as shown by equation 3.5 and Fig.3.2b. This opposes the increase in the structure factor afforded by the increase in intra-layer order. Therefore, during the first stage where the Bragg rod structure factor, $\langle S^{\text{rod}} \rangle$, increases, the gains in intra-layer order out-compete any gains in inter-layer order. Next, during the second stage where the

Bragg rod structure factor decreases, increasing inter-layer order dominates. This reveals that the hexgaonal planes that are initially formed have poor inter-layer order. This poor inter-layer order is due to layers sliding over one another under the shear near the walls during flow. In the third and final stage, the increases in inter and intra-layer order have equal effects on the structure factor. In this stage, the particles find lattice positions on the surface of the crystal and, in the absence of flow, establish inter and intra-layer order simultaneously.

We examine the effect of increasing the width of the capillary on the crystallisation. Diffraction patterns were measured as the same colloidal dispersion entered a capillary with internal z dimension twice as long at 0.2 mm. The structure factor evolution with time is similar to as shown in Fig.3.7a-c. However, the primary ring persists for a much longer time as shown by the structure factor at $t = 15$ minutes in Fig.3.8a. Next, we measure the structure factor change with time to monitor the inter and intra-layer ordering during crystallisation. The evolution of the structure factor with time for Bragg spots is similar for the wider capillary as for the narrower one, as shown in the inset of Fig.3.8b. However, the Bragg rod structure factor evolution with time is different. Here, we see a two stage process. Firstly, in stage one, we see that the Bragg rod structure factor, $\langle S^{\mathrm{rod}} \rangle$, increases between $t = 0$ and $t \approx 4.5$ minutes. In the second stage, after $t \approx 4.5$ minutes, the structure factor reaches a plateau. Note that $\langle S^{\mathrm{rod}} \rangle$ is again measured from the 2^{nd} order Bragg rods. The absence of the decay tells us that epitaxial crystal growth from the hexagonal layers occurs simultaneously with the establishment of inter-layer order between the shear-aligned hexagonal layers. The reason why we do not see a decay in the structure factor just after flow stops in the wider capillary is because the proportion of particles aligned in hexagonal layers during shear is lower. Therefore, the decrease in the inter-layer structure factor, S_z^{rod}, afforded by the increase in inter-layer order is out-competed by the increase in the intra-layer structure factor, $S_{||}^{\mathrm{rod}}$, as a result of the greater proportion of particles epitaxially crystallising into hexagonal layers.

In summary, the crystallisation mechanisms in the wider and thinner capillaries follow the same steps, where crystallisation is induced at the walls, and then propagates epitaxially into the bulk of the dispersion. However, the proportion of the crystal that is aligned by shear is lower in the wider capillary.

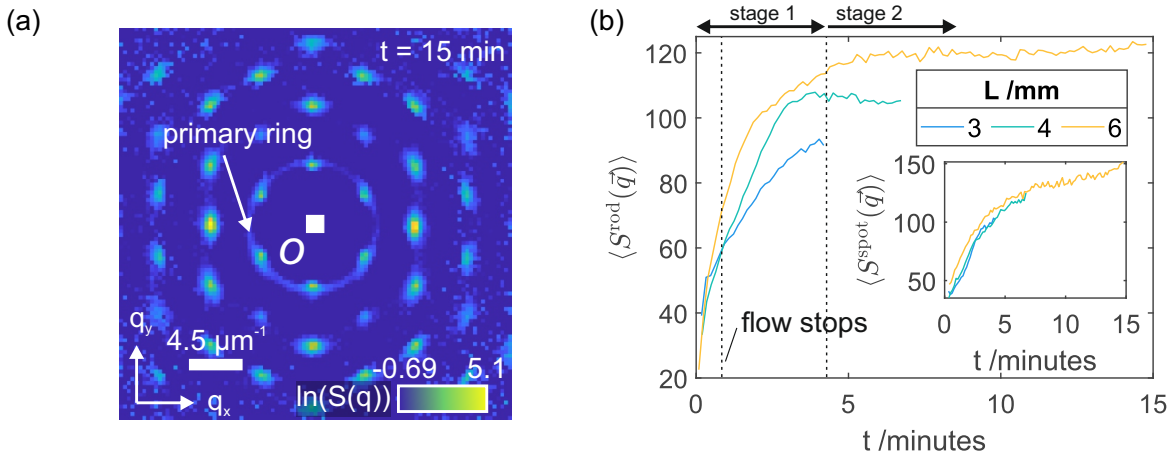


Figure 3.8: (a) 2D structure factor 15 minutes after capillary filling at $L = 6$. (b) Variation in the average structure factor for second order Bragg rods, $\langle S^{\mathrm{rod}} \rangle$, with time t. The inset shows $\langle S^{\mathrm{spot}} \rangle$ variation with time.

3.5 Conclusion

We have shown that large and singly oriented domains of random hexagonal close packed crystals can be produced by capillary action on a high volume fraction colloidal dispersion. Details of the local RHCP crystal structure were afforded by CLSM measurements, in particular allowing the visualisation of competing shear profiles on the crystal orientation. Global structure was uncovered by SAXS measurements, where goniometer scans revealed the three-dimensional reciprocal structure, supporting the measurements of the direct space structure from CLSM. SAXS also uncovered the mechanism of crystallisation: we measured the evolution of crystalline order between and within the hexagonal planes by comparing the structure factor time evolutions of Bragg rods and spots. Our measurements reveal the RHCP crystallisation pathway within the capillary, where, at the walls at early time crystallisation is dominated by the action of shear, aligning particles into hexagonal planes that slide over each other. After flow stops and shear ceases, we see then that the shear aligned hexagonal planes establish hexagonal stacking A, B and C positions, in tandem with crystallisation via epitaxy from the hexagonal layers. We suggest that aligning colloidal crystals using shear generated by capillary action may prove useful for the manufacture of photonic band gap crystals.

3.6 Appendix

3.6.1 Derivation of Wilson theory for lateral displacement correlations

We may modify Wilson theory to account for correlations between the translational positions of successive hexagonal layers along z. To this end, we start by defining the position of particle i in layer n as:

$$\vec{r}_{i,n} = \vec{r}_{i,0} + n\hat{z}d_{001} + \vec{\delta}_{||,n}, \tag{3.11}$$

where $\vec{r}_{i,0}$ is the position of the corresponding particle in layer 0, $\hat{z}$ is a unit vector parallel to the z axis, d_{001} is the separation between hexagonal layers and $\vec{\delta}_{||,n}$ is a vector within a hexagonal plane, responsible for the transition from an A layer to a B or C hexagonal layer. Recall that the structure factor for M particles is defined as:

$$S(\vec{q}) = \frac{1}{M}\left|\sum_{j}^{M} e^{i\vec{q}\cdot\vec{r}_j}\right|^2, \tag{3.12}$$

which may be written for particles in layers:

$$S(\vec{q}) = \frac{1}{M}\left|\sum_{n}^{N}\sum_{i}^{M/N} e^{i\vec{q}\cdot\vec{r}_{i,n}}\right|^2. \tag{3.13}$$

Substitution using equation 3.11 yields:

$$\begin{aligned} S(\vec{q}) &= \frac{1}{N}\left|\sum_{n}^{N} e^{i\vec{q}\cdot(n\hat{z}d_{001}+\vec{\delta}_{||,n})}\right|^2 \frac{N}{M}\left|\sum_{i}^{M/N} e^{i\vec{q}\cdot(\vec{r}_{i,0})}\right|^2 \\ &= S_z(\vec{q})S_{||}(\vec{q}), \end{aligned} \tag{3.14}$$

where $S_z(\vec{q})$ and $S_{||}(\vec{q})$ are the inter-layer and intra-layer structure factors respectively. The intra-layer structure factor is essentially non zero at integer values of h and k, see the random hexagonal close packed reciprocal structure in figure 3.1c. The inter-layer structure factor is modulated by the correlations between the layers and is of interest to us. Let $\vec{q}$ be the sum of

its components perpendicular and parallel to the hexagonal layers:

$$\vec{q} = \vec{q}_z + \vec{q}_{||}. \tag{3.15}$$

At normal incidence $\vec{q}_z = 0$, and the inter-layer structure factor can be written as:

$$S_z(\vec{q}) = S_z(\vec{q}_{||}) = \frac{1}{N}\left|\sum_n^N e^{i\vec{q}_{||}\cdot\vec{\delta}_{||,n}}\right|^2. \tag{3.16}$$

Using $|A|^2 = A^*A$ we may write this as a double sum:

$$S_z(\vec{q_{||}}) = \frac{1}{N}\sum_n^N\sum_{n'}^N e^{i\vec{q_{||}}\cdot(\vec{\delta}_{||,n}-\vec{\delta}_{||,n'})}, \tag{3.17}$$

which describes the averaging over possible layer arrangements from a randomly chosen layer n. The exponent depends only on the relative position between the two layers. For large number of layers, N, we can reduce this to N times the same single sum and replace the complex exponent by its statistically averaged value using the results of Wilson theory [83].

$$S_z(\vec{q}) = S_z(h,k) = \sum_{n=-\infty}^{\infty}\left(P_A(n)e^{i0} + P_B(n)e^{i2\pi(h-k)/3} + P_C(n)e^{-i2\pi(h-k)/3}\right), \tag{3.18}$$

where $P_A(n)$ is the probability of having layer n in the same lateral position as the first layer, and where $P_B(n)$ and $P_C(n)$ are the probabilities of a lateral shift between the two layers that produce an B or C layer, relative to the first layer. Here, $\vec{q}$ is restricted to reciprocal lattice peaks. Using the results for a randomly close packed hexagonal crystal (with stacking parameter $\alpha = 0.5$) we get the results for the probabilities:

$$\begin{aligned} P_A(n) &= \frac{1}{3} + \frac{2}{3}\left(-\frac{1}{2}\right)^{|n|} \\ P_B(n) &= \frac{1}{3} - \frac{1}{3}\left(-\frac{1}{2}\right)^{|n|} \\ P_C(n) &= P_B(n). \end{aligned} \tag{3.19}$$

To the structure factor we can add an additional term that modulates the positional correlation between the two layers:

$$S_z(h,k) = \sum_{n=-\infty}^{\infty} \left(P_A(n)e^{i0} + P_B(n)e^{i2\pi(h-k)/3} + P_B(n)e^{-i2\pi(h-k)/3} \right) \langle e^{i\delta\phi_n} \rangle, \tag{3.20}$$

where $\delta\phi_n$ is the additional phase shift associated with a random translational shift of the hexagonal layers. We can model $\delta\phi_n$ to be a symmetric random displacement, so its expectation value:

$$\langle \delta\phi_n \rangle = 0. \tag{3.21}$$

Furthermore, the random shift is independent of the shift in the previous layer, and the distribution in the phase differences between successive layers, $\delta\phi_{\Delta n}$, follows a normal distribution. to behave like a random walk. Therefore:

$$\langle \delta\phi_n^2 \rangle = |n| \langle \delta\phi_{\Delta n}^2 \rangle \equiv |n|\sigma^2, \tag{3.22}$$

where σ is the standard deviation in the distribution of the magnitudes of the random displacements. As such, there are equal contributions to the positive and negative imaginary part so:

$$\langle e^{i\delta\phi_n} \rangle = \langle \cos(\delta\phi_n) \rangle, \tag{3.23}$$

and can be written as a Taylor expansion:

$$\langle \cos(\delta\phi_n) \rangle = \sum_{k=0}^{\infty} \frac{(-1)^k}{(2k)!} \langle (\delta\phi_n)^{2k} \rangle. \tag{3.24}$$

Assuming a Gaussian distribution of $\delta\phi_{\Delta n}$, we can use the expression for the central moments:

$$\begin{aligned} \langle (\delta\phi_n)^{2k} \rangle &= |n|^k \langle (\delta\phi_{\Delta n})^{2k} \rangle \\ &= |n|^k \sigma^{2k} (k-1)!! \\ &= |n|^k \sigma^{2k} \frac{(2k)!}{2^k k!}, \end{aligned} \tag{3.25}$$

where $n!!$ is a double factorial, and σ is the standard deviation in the additional random lateral shift between successive layers. Substituting this result in equation 3.24 we arrive at:

$$\langle \cos(\delta\phi_n) \rangle = \sum_{k=0}^{\infty} \frac{(-1)^k}{k!} \left(\frac{|n|\sigma^2}{2} \right)^k , \tag{3.26}$$

which is equal to the Taylor expansion of an exponential. Therefore,

$$\langle e^{i\delta\phi_n} \rangle = \exp\left(-\frac{|n|\sigma^2}{2} \right). \tag{3.27}$$

Bragg rods

For Bragg rods $(h-k) \neq 3n$ where n is an integer, $e^{i2\pi(h-k)/3} = e^{i2\pi/3}$ so equation 3.20 becomes:

$$\begin{aligned} S_z^{\text{rod}} &= \sum_{n=-\infty}^{\infty} \left(P_A(n) - P_B(n) \right) \langle e^{i\delta\phi_n} \rangle \\ &= \sum_{n=-\infty}^{\infty} \left(-\frac{1}{2} \right)^{|n|} \langle e^{i\delta\phi_n} \rangle \\ &= \sum_{n=-\infty}^{\infty} \left(-\frac{1}{2} \right)^{|n|} \exp\left(-\frac{|n|\sigma^2}{2} \right). \end{aligned} \tag{3.28}$$

The sum is even, having the same value for positive and negative values of n. Therefore, it can be rewritten as:

$$S_z^{\text{rod}} = 2 \sum_{n=0}^{\infty} \left(-\frac{1}{2} \exp\left(-\frac{\sigma^2}{2} \right) \right)^n - 1, \tag{3.29}$$

where the subtraction of 1 removes the effect of double counting at $n = 0$, at which the value is equal to 1. We may use the result for the sum of convergent geometric series to evaluate the sum term. The sum of a geometric series may be represented as:

$$\sum_{n=0}^{\infty} ar^k = \frac{a}{1-r}, \tag{3.30}$$

which is convergent for $|r| < 1$. In our case $r = -\frac{1}{2}\exp(-\frac{\sigma^2}{2})$, fulfilling the convergence condition since σ is always a positive number, and $a = 2$. Therefore, we may rewrite equation 3.29 as:

$$\begin{aligned} S_z^{\text{rod}} &= \frac{4}{2 - \exp(-\frac{\sigma^2}{2})} - 1 \\ &= \frac{2 - \exp(-\frac{\sigma^2}{2})}{2 + \exp(-\frac{\sigma^2}{2})}. \end{aligned} \tag{3.31}$$

Bragg spots

Similarly, we evaluate $S(h,k)$ for Bragg spots where $(h-k) = 3n$. For this case $e^{i2\pi(h-k)/3} = e^{i2\pi}$ and equation 3.20 becomes:

$$\begin{aligned} S_z^{\text{spot}} &= \sum_{n=-\infty}^{\infty} 1\langle e^{i\delta\phi_n}\rangle \\ &= \sum_{n=-\infty}^{\infty} \exp\left(-\frac{|n|\sigma^2}{2}\right). \end{aligned} \tag{3.32}$$

Again, the function is even with n so we can write this as a convergent geometric series:

$$\begin{aligned} S_z^{\text{spot}} &= 2\sum_{n=0}^{\infty}\left(\exp\left(-\frac{\sigma^2}{2}\right)\right)^n - 1 \\ &= \frac{2}{1 - \exp\left(-\frac{\sigma^2}{2}\right)} - 1 \\ &= \frac{1 + \exp(-\frac{\sigma^2}{2})}{1 - \exp(-\frac{\sigma^2}{2})}. \end{aligned} \tag{3.33}$$

3.6.2 Structure factor calculations

The structure factor gives information about the arrangement of colloidal particles within the crystal. In scattering experiments, only the scattering intensity is measured which, as shown in equation 2.34, is a combination of the form factor and the structure factor. The form factor may be calculated from the particle radius and polydispersity (see table 2.1) as given in equation 2.21. Then, the structure factor may be calculated by $S(\vec{q}) = I(\vec{q})/F(\vec{q})$. The calculation is modified to account for a scaling, M, between the measured intensity and the multiplication of the normalised structure and form factors. An intensity contribution, B, from the internal,

molecular structure of the TPM particles is taken to be constant for the small scattering angles. Thus we calculate the structure factor by dividing the normalised intensity $I_N(\vec{q})$ by the form factor as follows:

$$S(\vec{q}) = \frac{I_N(\vec{q})}{F(\vec{q})}$$
$$I_N(\vec{q}) = (I(\vec{q}) - B)/M. \tag{3.34}$$

The values of B and M are those that satisfy the condition:

$$\min_{B,M} \sum_i (G(B, M, q_i) - 1)^2, \quad \text{where,}$$
$$G(B, M, q_i) = \frac{I(q_i) - B}{MF(q_i)}, \tag{3.35}$$

where i runs over the set of user defined high q values. Here, the structure factor oscillates about and decays to 1. $I(q_i)$ and $F(q_i)$ are averaged intensities within a shell of user defined thickness, centered at q_i. $I(q_i)$ is calculated from the pixel grid of intensities from the 2D diffraction image after subtraction of a background image of a capillary containing only solvent, rescaled to account for the sample adsorption. Similarly, $F(q_i)$ is calculated from a 2D form factor (see equation 2.21) using the same pixel grid and centre of reciprocal space as the diffraction image. This (radial) average is calculated as:

$$A(q_i) = \frac{1}{N} \sum_j^N \left(A_j(q_i)\right), \tag{3.36}$$

where A represents either I or F and where j spans the pixels within user defined range of q_i. It is worth noting here that $A(q)$, where A may represent I, F or S, represents the radial average and is calculated from an image by considering the pixel grid in the following way.

$$A(q) = \{A(q_i)\}, \tag{3.37}$$

where i spans the set of user defined q value bins over the field of view.

The locations of the structure factor peaks within a 2D structure factor image are found using the Crocker-Grier method (see section 2.5). To avoid incorrect peak detection, local maxima below half of the mean pixel value are ignored. The value of the structure factor is calculated from the integrated brightness over an area approximately equal to the peak area.

Goniometer scan

For goniometer scans, the values of B and M are calculated from normal incidence diffraction patterns and applied to each diffraction image in the goniometer scan to find the two dimensional structure factor using equation 3.34 at each goniometer image. For each image in a goniometer scan, the (q_x^ω, q_y) peak coordinates are calculated. The q_y axis is parallel to the goniometer rotation axis and the real laboratory frame axis y. The goniometer scan rotates the crystal so that q_x rotates out of the plane of the SAXS image. As such, the q_x axis becomes q_x^ω, which is normal (90° clockwise) to the q_y axis where the superscript, ω, refers to the goniometer rotation angle. These coordinates are tracked across each image of the goniometer scan using the Crocker Grier tracking method to provide structure factor variation with rotation angle. These variations will later be used to define the reciprocal lattice vector $\vec{c^*}$ and to determine the stacking parameter, α. Coordinates are converted to the reciprocal laboratory frame frame where the (q_x, q_y, q_z) axes are respectively parallel to (x, y, z) axes, as shown in Fig.3.4, and are calculated using:

$$(q_x, q_y, q_z) = (q_x^\omega \cos(\omega), q_y, q_x^\omega \sin(\omega)). \tag{3.38}$$

This provides tracks of positions in space along q_z with associated structure factor values.

Determination of Bragg spots and rods

The structure factor variation with q_z of Bragg spots is used to measure length of reciprocal lattice vector $c^* = |\vec{c^*}|$ whereas the variation for Bragg rods provides a measure for the stacking parameter, α. Therefore, rods and spots must be identified. The (q_x, q_y) coordinates of the first order peaks define the $\vec{a^*} = (q_x^a, q_y^a)$ and $\vec{b^*} = (q_x^b, q_y^b)$ reciprocal lattice vectors. The indices h and k are determined from each coordinate as the multiples of $\vec{a^*}$ and $\vec{b^*}$:

$$(q_x, q_y) = h(q_x^a, q_y^a) + k(q_x^b, q_y^b). \tag{3.39}$$

Once the h and k values are known, the peak coordinates are split up into Bragg rods, $h-k \neq 3n$, and Bragg spots, $h - k = 3n$.

Bragg rod $S(l)$ from $S(\vec{q})$

For Wilson theory, $S(l)$ is extracted from $S(\vec{q})$ by converting the q_z coordinate to fractions of the Miller index l:

$$l = \frac{q_z}{c^*}, \tag{3.40}$$

where c^* is calculated as:

$$c^* = \frac{1}{N}\sum_{i}^{N} \frac{q_{z,l,i}}{l} \quad \text{for} \quad l \neq 0. \tag{3.41}$$

Here, $q_{z,l,i}$ are q_z coordinates of the Bragg spots in the same goniometer scan and where i runs over the N coordinates with $l \neq 0$. The Bragg spot q_z, l coordinates are the local maxima in the $S(\vec{q})$ against q_z for each track (see Fig.3.6d). The value of l is determined by binning reciprocal space but as a consequence of the goniometer scan only running between $-70° < \omega < 70°$, only spots with $-1 < l < 1$ are observed.

3.6.3 Lattice constant calculation

CLSM

The 12 closest nearest neighbours within a cut off distance equal to the first minimum in the radial distribution function are calculated. Then, the relative neighbour positions from their respective central particles are calculated by subtracting the coordinates of the central particles. This is followed by a spatial binning to find distributions of relative lattice constants shown in Fig.3.9. Points more than two standard deviations from the mean are rejected, and then the mean is recalculated.

SAXS

The constants a' and b' are calculated as the mean value from the coordinates of the structure factor peaks q_x and q_y respectively at normal incidence, $\omega = 0$, for both Bragg rods and spots.

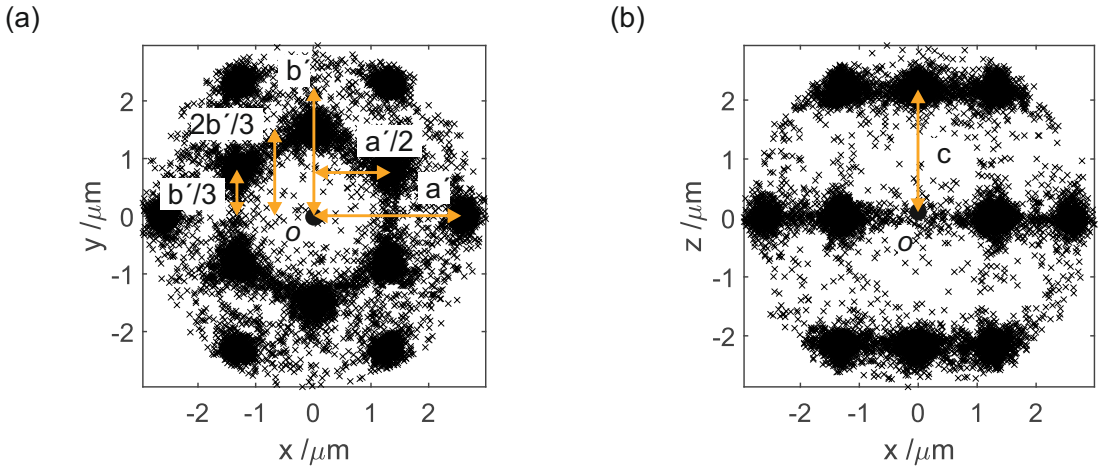


Figure 3.9: (a) and (b) show xy and xz projections of nearest neighbours relative to their parent. The parent is not shown but sits at the origin. The lattice constants are marked.

They are calculated as:

$$a' = \frac{1}{N}\sum_{i}^{N}\frac{2\pi h'}{q_{x,i}} \quad \text{for} \quad h' \neq 0 \quad \text{and}$$
$$b' = \frac{1}{M}\sum_{i}^{M}\frac{2\pi k'}{q_{y,i}} \quad \text{for} \quad k' \neq 0, \tag{3.42}$$

where h' and k' are integers (Miller indices for $\vec{a'}$ and $\vec{b'}$) and i runs over the N q_x or M q_y coordinates with non zero h' or k' values respectively. The values of h' and k' for each structure factor peak is determined by binning reciprocal space coordinates. The lattice constant c is calculated from the sharp structure factor peaks along the q_z coordinate of Bragg spots. Equation 3.41 is modified to give the result for c:

$$c = \frac{1}{N}\sum_{i}^{N}\frac{2\pi l}{q_{z,l,i}} \quad \text{for} \quad l \neq 0. \tag{3.43}$$

Standard error

The equations above give values for the population mean lattice constants. The standard error is calculated as:

$$\varepsilon = \frac{\sigma}{\sqrt{N}}, \tag{3.44}$$

where σ is the population standard deviation and N is the number of measurements. For a' and b', the number of measurements corresponds to N and M as described above for equation 3.42, and for c, N is as defined for equation 3.43. The errors reported as:

$$\langle x \rangle \pm \varepsilon, \tag{3.45}$$

where $\langle x \rangle$ is the population mean.

3.6.4 Approximate volume fraction calculation

The volume fraction is approximated during sample preparation using the following method. After a colloidal sediment is produced by centrifugation, solvent is added to the solution to reach the target volume fraction, ϕ_t. The volume of added solvent is:

$$\begin{aligned} V_\mathrm{add} &= \frac{0.64}{\phi_\mathrm{t}} - V_\mathrm{s} \quad \text{where,} \\ V_\mathrm{s} &= \rho_\mathrm{s} m_\mathrm{s}, \end{aligned} \tag{3.46}$$

where 0.64 is the maximum volume fraction for randomly arranged spheres [106], V_s the volume of the sediment, ρ_s the mass density of the sediment and m_s the mass of the sediment. The mass, m_s, is calculated by balance and subtracting the mass of the container. The density is approximated by:

$$\rho_s = 0.64\rho_\mathrm{TPM} + 0.36\rho_\mathrm{solv}, \tag{3.47}$$

Where $\rho_\mathrm{TPM} = 1.235\mathrm{gcm}^{-3}$ [76] and ρ_solv is the weighted average of the pure mass densities of the constituent solvents. For the colloidal samples detailed above, $\rho_\mathrm{TTL} = 0.973\mathrm{gcm}^{-3}$ and $\rho_\mathrm{DCL} = 0.896\mathrm{gcm}^{-3}$. The contribution of OLOA to the density is neglected.

Acknowledgements

The experiments were co-performed with T. Yanagishima and A. V. Petukhov. Special thanks to A. V. Petukhov for help with modified Wilson theory, and to I. P. Dolbnya for preparing the unique microradian X-ray diffraction setup at B-16, Diamond Light Source, Didcot, UK.

Chapter 4

Deformation under gravity of shear-aligned colloidal crystals

Abstract

Large, single orientation domains of random hexagonal close packed colloidal crystals break up into many crystalline regions as they deform under a gravitational field. Herein, we characterise the crystal rotations and lattice deformations within the crystal using a combination of confocal microscopy and small angle X-ray scattering. We find that the crystal rotations are not random, but share a common misorientation axis, providing a route to generate exclusively tilt grain boundaries. We examine the mechanism of crystal rotation and suggest that crystal rotation occurs from high shear strain rates via the cooperative motion of colloidal particles.

4.1 Introduction

Colloidal dispersions are a useful model system for the study of many physical phenomena such as nucleation [115], grain growth [52], epitaxy [116] and the dynamics of grain boundaries [117]. Slow particle dynamics and the ability to resolve locally colloidal particles using microscopy techniques [118] provide advantages over atomic and molecular systems, where phenomena occur at inaccessibly small time and length scales. Colloidal systems are soft, with a Young's modulus of colloidal crystals being approximately 14 orders of magnitude lower than for atomic systems (as demonstrated in section 2.2) and are, therefore, easily deformed in external fields, such as gravity. As a result, colloidal crystals provide an ideal model system to study structure evolution during crystal deformation.

Since the 1980s [108, 119] colloidal dispersions have also been employed to study physical phenomena under shear such as shear thinning and thickening [87], banding [101, 120], crystallisation [91, 94–96, 104] and melting [95]. A particularly appealing aspect of using shear to manipulate structure on the colloidal scale is the ability to produce large colloidal crystal domains with controlled orientation and crystal structure [93, 104, 119], especially with the view to create photonic band gap crystals [103]. While most measurements of the effect of shear on structure occur during shear [87, 95, 96, 101], studies of structure evolution after the shear is terminated are limited. It is essential to characterise the long term properties of such structures for use in advanced material applications, as the structures formed by shear are often far from equilibrium [121].

Previously, we examined the crystallisation of colloidal dispersions under shear produced by capillary flow in a narrow and flat walled capillary using small angle X-ray scattering, SAXS, and confocal microscopy, CLSM. We examined the crystal structure during shear and shortly after the termination shear to reveal an RHCP crystal structure with single orientation domains containing $\approx 1{\times}10^4$ particles. Herein, we employ SAXS and CLSM to monitor structural changes of the same crystals over a longer timescale of tens of hours, long after the termination of shear. We see a change in crystal lattice constant and in the proportion of FCC to HCP with the RHCP crystal. In some instances, we see that the crystals break up from one RHCP crystal orientation into many under the influence of gravity. In this case the colloidal crystals provide a model system to examine the mechanism of RHCP crystal fracture. We show links between crystallite

rotation, crystal lattice constant changes over time and space, and confinement from the capillary walls. We also observe that crystal rotations share a rotation axis. Therefore, the deformation of shear aligned RHCP crystals produces RHCP polycrystals containing exclusively tilt type grain boundaries, i.e. those where the rotation axis sits in the grain boundary plane. This synthesis route to tilt polycrystals should facilitate systematic experiments relating misorientations of tilt boundaries to their physical properties, such as stiffness or mobility.

4.2 Methods

We extended the study of the shear-aligned RHCP colloidal crystals from chapter 3 to observe their structure over time, after the termination of shear. As such, the experimental methods are similar, using a combination of SAXS and CLSM techniques to reveal complementary structural information. The capillary is oriented so that the hexagonal planes in the RHCP crystal structure are parallel to the xy walls (see Fig.4.1a) of the capillary and that gravity, $\vec{g}$, is (anti)parallel to the y axis and the $\vec{G}_{1\bar{1}0} = \vec{a^*} - \vec{b^*}$ reciprocal lattice vector (see equation 2.16 and reciprocal lattice vectors are defined in Fig.3.1c), as shown in Fig.4.1b. Note that the orientation of the RHCP crystal within the capillary was revealed in section 3.4.1.

4.2.1 Colloidal samples

Colloidal samples identical to the previous chapter were used, and are summarised in table 4.1, reproduced from chapter 2.

Type	Diameter /μm	p	Interaction	Use	Solvent	[OLOA] /%
A	1.5	0.058	hard sphere like	SAXS	TTL	2
B	1.4	0.049	hard sphere like	SAXS	2 DCL : 3 TTL	5
C	2.1	0.060	soft repulsive	CLSM	2 DCL : 3 TTL	0.5

Table 4.1: Colloidal samples for flow-aligned colloidal crystal experiments, where p is polydispersity.

4.2.2 Crystal rotations

We observe that the single RCHP crystal breaks apart into many domains exhibiting different crystallite rotations. The rotations of the crystallites are characterised using SAXS and CLSM.

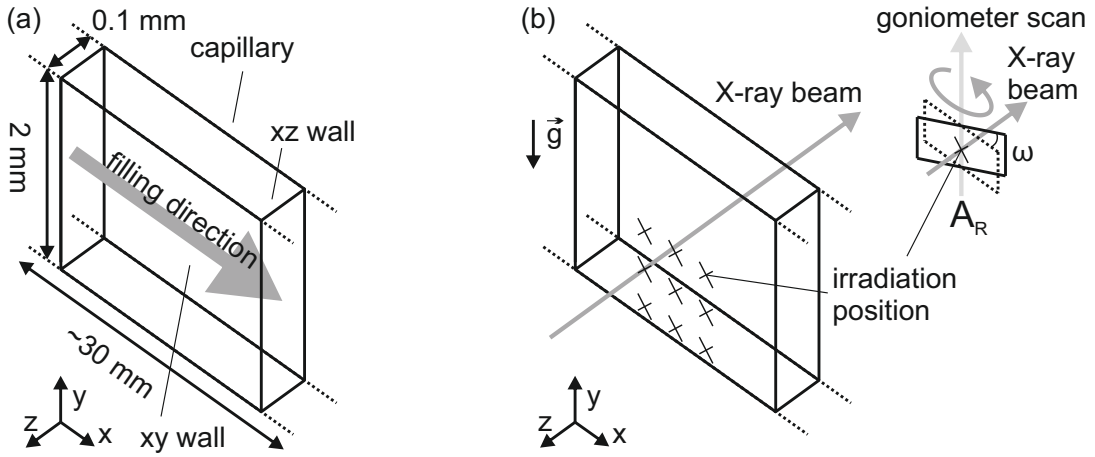


Figure 4.1: (a) Experimental set up, showing the capillary oriented in the laboratory frame. The filling direction, and the shape of the capillary controls the orientation of the RHCP crystal inside. (b) X-ray scattering geometry. The black crosses indicate irradiation positions and the grey arrow marks the X-ray beam path. The inset at the top right shows the goniometer scan geometry to resolve the 3D reciprocal crystal structure.

Firstly, the movement of the Bragg spots obtained from goniometer scans (see appendix 3.6.2) at positions on a 3 by 3 grid spanning 1 mm $\times$1 mm in the crystal (see Fig.4.1b) are used to identify crystallite rotations. The Crocker Grier tracking method [80] is used both to find trajectories of the reciprocal lattice points and to register reciprocal lattice point sets at each time to allow orientation measurement using the Kabsch algorithm [122]. The positions of the set of reciprocal lattice points at time t and their corresponding pairs at initial time form the input to the Kabsch algorithm. Note that we modify the Kabsch algorithm to fix the centre of rotation at the origin of reciprocal space instead of at the centre of mass of the reciprocal lattice points. In this way, the rotation calculation is robust against missing reciprocal lattice points. Secondly, crystal rotations are calculated using CLSM, but using a different method. The local orientation of crystalline particles is measured following the method described in detail in chapter 5. In brief, a point set registration algorithm matches a reference FCC or HCP nearest neighbour cluster to a specimen nearest neighbour cluster. The clusters are found from the coordinates of particles obtained from Crocker-Grier particle identification [80] from CLSM images. The orientation of each nearest neighbour cluster is identified and then separated into volumes of single orientation known as grains. Following this, the relative orientation (misorientation) between the grains at the initial and final time reveals the rotation.

4.2.3 Lattice constant strain

Goniometer scans are repeated over time at different positions in the crystal to measure the laboratory frame lattice constants, a', b' and c, as defined in section 3.3.3 and as shown in Fig.4.1b. The capillary is oriented in the laboratory frame identically to before, (see Fig.4.1a), and the laboratory frame lattice constants are calculated from goniometer scans following the same methods described in the previous chapter (see appendix 3.6.2 and 3.6.3). The strain in lattice constant a', $\epsilon_{a'}$, is calculated as:

$$\epsilon_{a'} = \frac{a' - a'_0}{a'_0}, \tag{4.1}$$

where a' is the mean value[1] at time t over all positions at the same height in y, and a_0 is the mean value at initial time over all positions which is approximated from the first goniometer scans from each of the 9 positions[2] in x and y. A negative or positive value of $\epsilon_{a'}$ corresponds to a compression or expansion respectively. The lattice constant strains are calculated in an identical fashion for b' and c.

4.2.4 Stacking parameter

The stacking parameter, α, was measured over time and space by performing SAXS goniometer scans at several positions in the crystal (see Fig.4.1b). Each goniometer scan is performed identically to before (section 3.3.3), where the rotation angle spans $-70^\circ \leq \omega \leq 70^\circ$ about a rotation axis parallel to y and diffraction images are taken every 1°, as illustrated to the right of Fig.4.1b. The analysis of the reciprocal structure was performed using Wilson theory, as described in section 3.3.3, applying equation 3.10.

4.3 Results and discussion

This section is organised as follows. Firstly, we characterise the crystal deformation by examining the rotations of the crystallites. Secondly, we examine the evolution of the lattice constants and

[1] We find that lattice constants evaluated from individual positions at the same height in y have values within the standard error of each other over the duration of the experiments.

[2] The 9 goniometer scans take $\approx$ 15 minutes each, totalling $\approx$ 2 hours per cycle, which is small on the time scale of the experiment so should give a good approximation of the initial lattice constant.

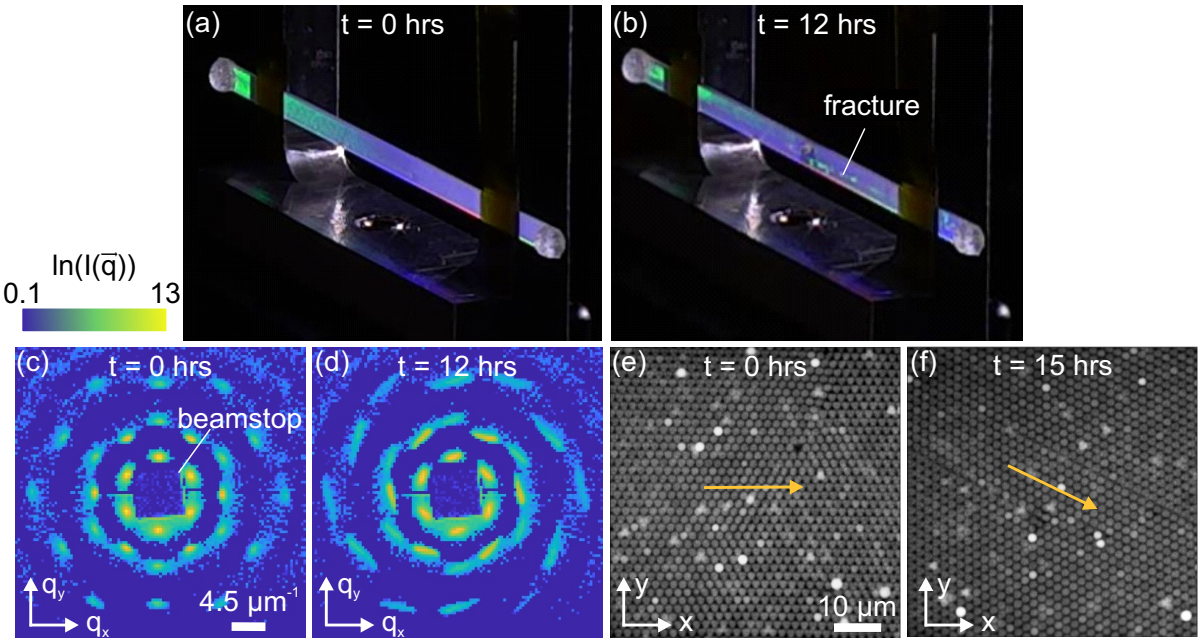


Figure 4.2: Photograph of the Bragg scattering from an example crystal (a) at initial time and (b) at late time, 12 hours. (c) and (d) show an example of the diffraction intensity patterns obtained at normal incidence at initial and final time time respectively. The colour bar relates to both panels (c) and (d). (e) and (f) show CLSM xy slices at initial and final time respectively. The arrows show the close packing direction [96] of the 2D hexagonal layers.

the volume fraction over time and space. Thirdly, we describe a model for the mechanism which links the crystallite rotations to the local changes in the lattice constants. Finally, we apply Wilson theory to the Bragg rods to evaluate the change in the hexagonal stacking parameter, α, over time.

4.3.1 Crystal rotations

A colloidal crystal with a $\phi_0 = 0.41$ (type A) is positioned as illustrated in Fig.4.1a. Photographs of the initial and late time appearance are shown in Fig.4.2a and Fig.4.2b respectively. We see a change from a uniform Bragg scattering effect at early times (Fig.4.2a) to one with a non-uniform appearance (Fig.4.2b) after 12 hours. The change in appearance is the result of crystal fracture where the single domain RHCP crystal has rotated to produce domains of different orientation, scattering different wavelengths of light in different directions. Fig.4.2c and d show corresponding diffraction patterns[3] at initial and late times. Closer inspection of the diffraction pattern in Fig.4.2d reveals that diffraction peaks are circumferencially smeared and extend to either side of their counterparts in Fig.4.2c. This reveals that within the irradiated volume, both

[3]These patterns are from a type B crystal, but are qualitatively similar to those from a type A crystal.

clockwise and anticlockwise rotations about the z axis are observed. Note that the majority of the crystal has rotated clockwise as evidenced by the clockwise skew in intensity of the smeared peaks. Crystal rotation is also seen in direct space. Figures 4.2e and f show xy slices from CSLM images of a $\phi_0 = 0.37$ (type C) colloidal crystal. Rotation of the hexagonal planes within the RHCP crystal can be seen, and two snapshots of the crystal structure in the xy plane are shown in Fig.4.2e and f. To guide the eye, the close packing direction [96] has been marked on each image.

The SAXS and CLSM images in Fig.4.2c-f suggest that the crystallite rotation axis is normal to the image plane, however these 2D images do not reveal the entire 3D rotation. To confirm the axis of rotation, the rotations are measured from the 3D structure in direct and reciprocal space. In reciprocal space, rotations of the 3D Bragg spots are measured, an example of which at $y = 0$ mm is shown in Fig.4.3a. The black spots show the initial positions and the arrows represent their movements over 15 hours. The dotted lines are to guide the eye to the orientation of hexagonal planes of Bragg spots. The mean of the normalised vectors representing the rotation axes was calculated, as described in section, 4.2.2 as $(-0.067, 0.013, -1.0)$ and the direction of the rotation axis is plotted as the grey arrow in Fig.4.3a. The standard deviation in the components of the normalised rotation axes over the entire field of view is small: $(-0.016, 0.035, 9.6 \times 10^{-4})$ suggesting that all rotation axes are approximately parallel to the laboratory frame z axis, i.e. perpendicular to the hexagonal planes of particles in the crystal. Although the rotation axes are parallel, the rotation angle varies at different positions in the crystal due to differing individual crystallite rotations. The common rotation axis and multiple rotation angles suggests that a polycrystal containing entirely tilt grain boundaries is produced during the rotational fracture of these shear-aligned RHCP colloidal crystals.

The rotational fracture is corroborated by CLSM experiments of a type C colloidal crystal with a $\phi_0 = 0.37$. Fracture events observed using CLSM support what is seen in the SAXS measurements. The mean rotation over 15 hours for the nearest neighbours (see section 5.3.1 of chapter 5 for the definition) of the FCC part of the RHCP crystal is shown in Fig.4.3b. The black crosses indicate the original starting position and the black arrows shows their movement. The dotted lines are a guide to the eye to the hexagonal planes. The mean normalised rotation axis was calculated from the misorientation between the FCC grains at initial time t_0 and at time t to be $(0.080, 0.00041, 1.0)$ which lies close to parallel with the laboratory frame z axis,

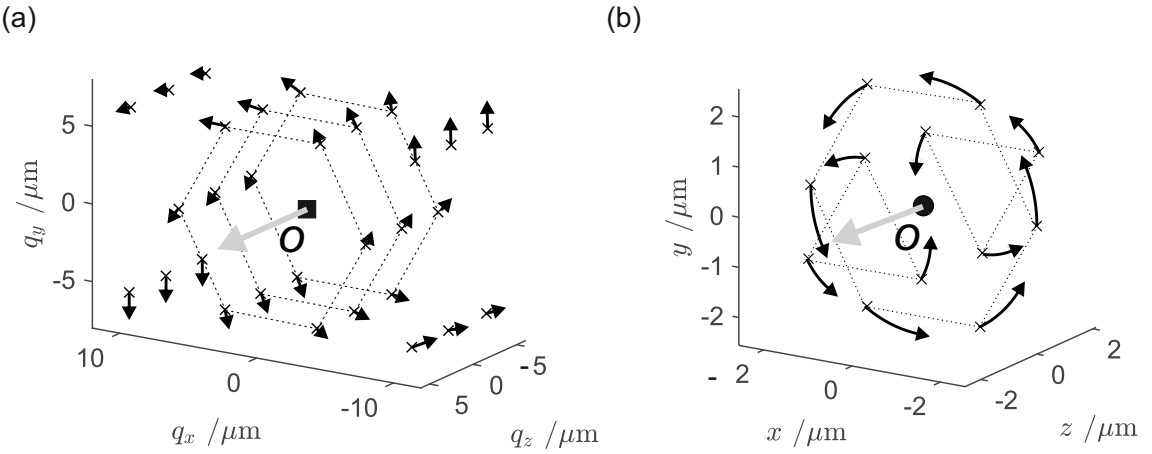


Figure 4.3: (a) SAXS measurement of rotation axis. 3D Bragg spot rotation at $y = 0$ mm for a $\phi_0 = 0.42$ type A crystal. Black arrows represent movement of tracked reciprocal lattice peaks over time, grey arrow shows the mean rotation axis. Total rotation at this position was 6.29°. The dotted lines are to guide the eye to the orientation of the hexagonal planes of Bragg spots. (b) CLSM measurement of rotation axis for a $\phi_0 = 0.37$ type C crystal. Here, the mean rotation axis in grey is shown pointing from the centre of an FCC nearest neighbour cluster. The black arrows show the rotation of these points over an angle of 27.1°.

agreeing with the observations from SAXS.

4.3.2 Evolution of lattice constants and volume fraction

Next, the deformation of the crystal is characterised by examining the changes in the laboratory frame lattice constants, a', b' and c (as defined in section 3.3.3). These lattice constants are measured in three dimensions as the crystal deforms under gravity using goniometer scans as shown in Fig.4.1b. The evolution of the lattice constant strains (see equation 4.1) over time for several heights in y are shown in Fig.4.4a-c. The lattice constants change from their original values of $a' = 1.796 \pm 0.004$ µm, $b' = 1.567 \pm 0.007$ µm and $c = 1.488 \pm 0.004$ µm, with a strong dependence on y which is (anti)parallel to gravity. Note that these results are for the same crystal as in the SAXS measurements from section 3.4.1. The lattice constants higher in the crystal i.e. at larger y values, shrink successively after a lag time of about 6 hours. The contraction occurs due to the movement of the crystal parallel to the y axis under gravity, resulting in a compression at the bottom of the crystal. The compression may be monitored by calculating the volume fraction at each position in y. By combining the lattice constants we may calculate the volume fraction as:

$$\phi = \frac{4\pi r^3}{3a'b'c}, \tag{4.2}$$

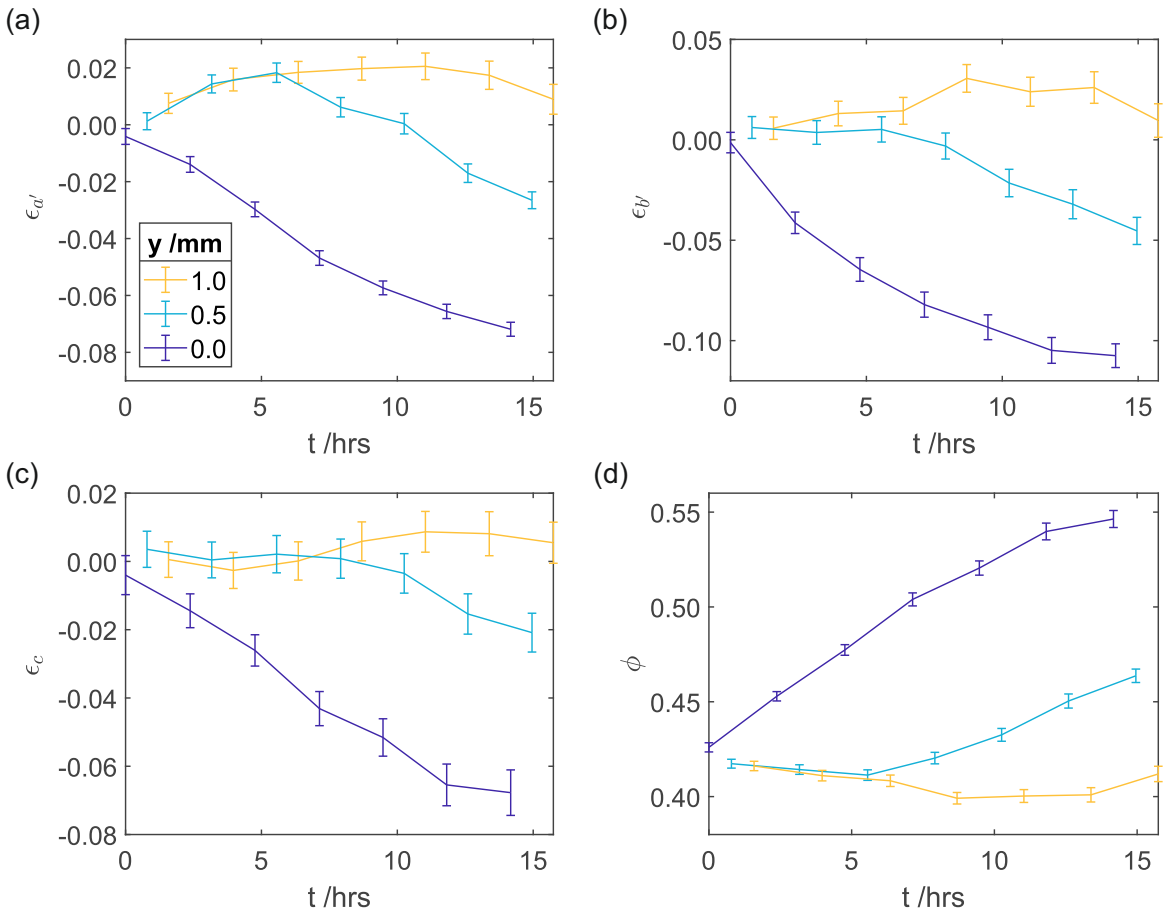


Figure 4.4: (a) - (c) Time evolution of lattice constant strains $\epsilon_{a'}$, $\epsilon_{b'}$ and ϵ_c respectively. Measurements are taken at several heights in y. (d) Volume fraction, ϕ, evolution with time. These results are for a type A colloidal crystal with $\phi_0 = 0.42$. Measurements are taken at several heights in y. The error bars show the standard error and details of the calculation are given in appendices 3.6.3 and 4.5.1.

and its time evolution is plotted in Fig.4.4d. We see that the volume fraction increases quickly at the bottom of the crystal and slightly decreases higher up in the crystal at $y = 0.5$ mm before increasing after a lag time of $t \approx 6$ hours. After another 6 hours, we see the volume fraction at $y = 1.0$ mm increasing. Increases in volume fraction at successive y positions is indicative of a densification front moving through the crystal. We can determine the speed of the densification front from the inflection points of the volume fraction curves to calculate a speed of 2.8×10^{-8} ms^{-1}.

We propose that the densification of the crystal is a result of the sedimentation of the crystal. If this is true, the sedimentation velocity of the particles, u_c, must be greater than the densification front velocity, as the motion of the densification front is driven by sedimenting particles arriving at the front's surface. However, as these particles arrive, the volume fraction of this region increases, hindering the advancement of the front. The sedimentation velocity of

particles in the crystal may be approximated by the volume fraction modified Stokes velocity [5],

$$u_c = \frac{2g\Delta\rho r^2}{9\eta}(1-\phi)^{-K_2}, \tag{4.3}$$

where g is acceleration due to gravity, $\Delta\rho$ is the difference in mass densities between the solvent and the colloidal particles, r is the radius of the particle, η is the viscosity of the solvent, ϕ is the volume fraction and K_2 is a constant specific to the colloidal dispersion [5]. From equation 4.3, it is clear that the sedimentation velocity decreases with increasing ϕ and sensitively depends on K_2, which is reported to be $-6 < K_2 < -1$ for similar colloidal dispersions [5]. As equation 4.3 applies to a colloidal fluid, we only use it here to obtain a rough estimate for the sedimentation velocity of the particles in our crystal. Using $r = 0.75 \times 10^{-6}$ m, $\phi = 0.4$, η for tetralin $= 1.9 \times 10^{-3}$ kgm^{-1}s^{-1}, $\Delta\rho = 0.33 \times 10^{-3}$ kgm^{-3} and $K_2 = -1$ we find a lower bound for the velocity of, $u_c \approx 1.8 \times 10^{-7}$ ms^{-1}. This is quicker than the densification front speed, indeed suggesting that the densification is driven by sedimentation.

Notably, we observe a slight expansion of lattice constants and a decrease in volume fraction high up in the crystal. We believe this is due to the displacement of solvent from the bottom of the crystal upwards, thereby reducing the volume fraction high in the crystal. Here, the particles have more space and are therefore, positioned at a greater distance from their neighbours. Finally, we note that the behaviour of the lattice constants is also governed by the confinement from the capillary walls. Before the densification front reaches $y = 0.5$ mm, the crystal displays a positive Poisson ratio where a' increases as b' decreases (see Fig.4.4a and b). As b' shrinks slightly under the action of gravity, a' being orthogonal to the force from the weight of the crystal above, correspondingly expands. However, there is no expansion along the other orthogonal direction parallel to c at $y = 0.5$ mm (see Fig.4.4c), likely due to high confinement along z, the shortest dimension of the capillary, hindering the crystal's expansion.

In summary, we have shown that deformations occur heterogeneously throughout the crystal, where lattice constant strain depends sensitively on y position. In the following section, we discuss how lattice constant changes lead to crystal rotations, and explain why crystal rotations occur with rotation axes parallel to the z axis exclusively.

4.3.3 Crystal rotation mechanism

In this section, we first introduce a model for the rotation mechanism. Secondly, we test the model by examining the crystal deformation and rotations with greater spatial resolution and by inspecting the model's predictions.

Model

We propose that the crystal rotation is a result of shear created by the gradient in the strain in a' (parallel to x), $\epsilon_{a'}$, (see equation 4.1) with respect to y. As shown in Fig.4.4a, at the bottom of the crystal ($y = 0.0$ mm), $\epsilon_{a'}$ reaches -0.02 after approximately $t = 4$ hours, whereas higher up in the crystal (at $y = 0.5$ mm) it takes approximately $t = 15$ hours to reach this value. This alone does not provide evidence for the generation of shear within the crystal, it only describes the average strain for each unit cell within the irradiation volume. However, the observation of crystal rotations (see section 4.3.1) shows that colloidal particles exhibit cooperative motion within the crystal. Therefore, it is likely that many particles move cooperatively parallel to x as $\epsilon_{a'}$ decreases. A greater magnitude of $a' - a'_0$ and therefore, $\epsilon_{a'}$ (see equation 4.1) leads to greater cooperative motion. As a consequence, a shear is produced when $\epsilon_{a'}$ is not uniform along y, i.e. there is a gradient in $\epsilon_{a'}$ with respect to y, as illustrated in Fig.4.5c. We express the local shear, $\gamma_{a'}$, in the crystal as:

$$\begin{aligned} \gamma_{a'} &= \frac{\Delta a'}{\Delta y} \quad \text{where,} \\ \Delta a' &= a'_j - a'_i \\ \Delta y &= y_j - y_i, \end{aligned} \tag{4.4}$$

where a'_i and a'_j are lattice constants at the successive y positions y_i and y_j, respectively. The example for $i = 1$ and $j = 2$ is illustrated in Fig.4.5c where the cooperative motion amplifies the shear from each of the N unit cells, and leads to crystal rotation, as shown in Fig.4.5d. Therefore, we suggest that rotations occur with axes parallel to z for large enough values of $N\gamma_{a'}$, where N is the number of cooperatively moving unit cells.

We may use the model to explain why we observe no rotations with axes parallel to x even though we observe gradients in the strain in c (parallel to z), ϵ_c, with respect to y (see

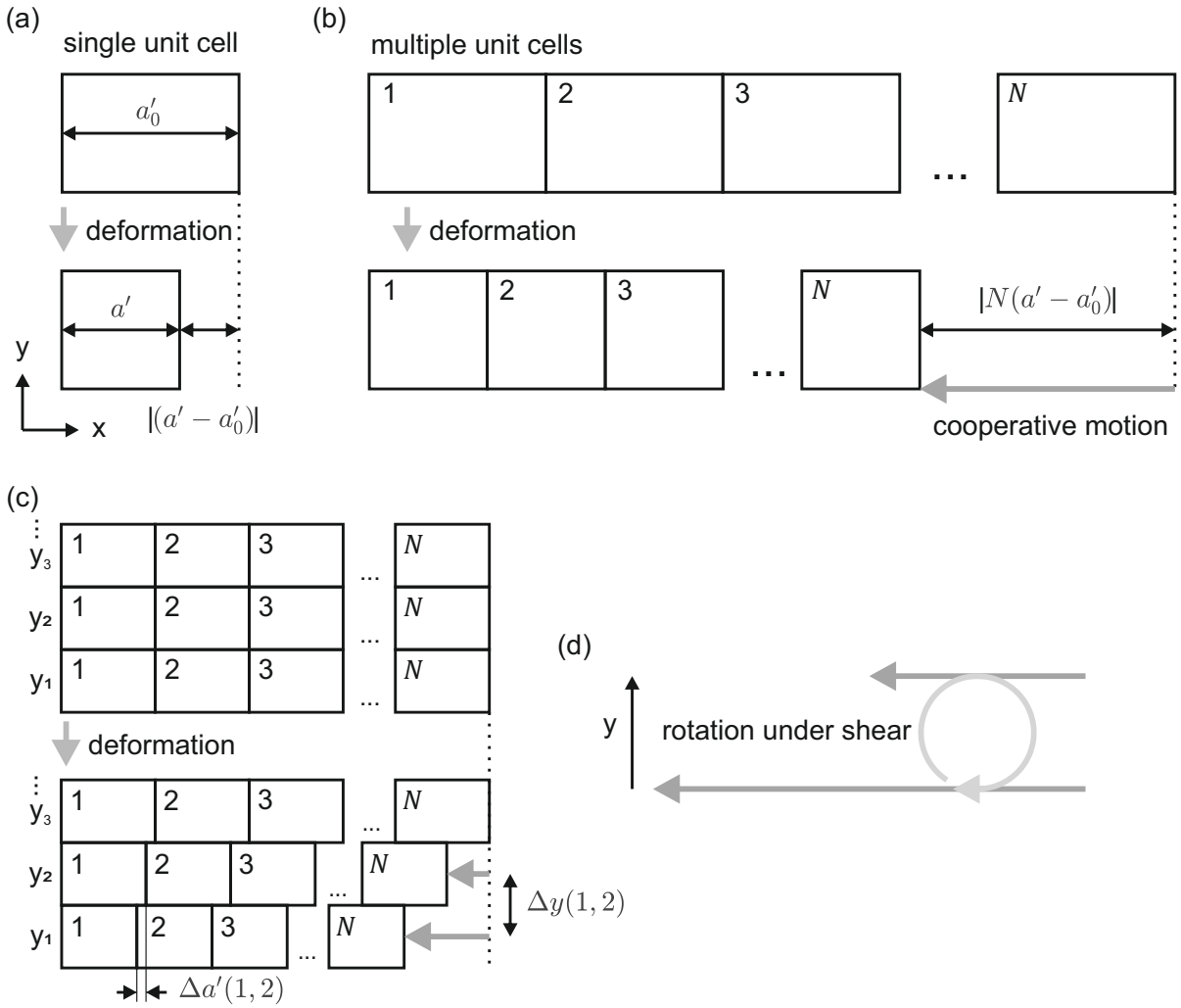


Figure 4.5: Model for crystal rotation under local shear strain. (a) Strain in lattice constant a' for a single unit cell. (b) Strain in lattice constant for multiple unit cells moving cooperatively to create a flow. (c) Cooperative motion flows of different magnitudes for different strains. (d) Rotational motion initiated by shear.

Fig.4.4c). According to the model, we expect rotations for a large value of $M\gamma_c$, where M is the number of cooperatively moving unit cells in the z direction and γ_c is the local shear strain along the z direction. Similarly to in equation 4.4, $\gamma_c = \frac{\Delta c}{\Delta y}$, where Δy is the change in height, as defined equation 4.4 and accordingly, Δc is the change in lattice constant over this height so that $\Delta c = c_j - c_i$. We see from Fig.4.4a and c, that the strains $\epsilon_{a'}$ and ϵ_c have similar time and y dependencies, so we let $\Delta a \approx \Delta c$ and therefore, $\gamma_{a'} \approx \gamma_c$. From this we can infer that no rotations with axes parallel to x are observed because the dimension of the capillary in z is small (0.1 mm) and therefore, M is small resulting in small $M\gamma_c$ and therefore, negligible rotations. Furthermore, we see no gradient in $\epsilon_{b'}$ with respect to x as each irradiated position in x at the same y resulted in values of b' within error of each other. Therefore, we do not observe shear and correspondingly we expect no rotation. As such, we only consider shear resulting from $\epsilon_{a'}$ in the following discussion.

Spatial distribution of shear strain

We measure the lattice constant a' with increased spatial and temporal resolution, allowing the detailed measurement of $\gamma_{a'}$ over space and time. To this end, the crystal deformation under gravity experiments were repeated. However, the X-ray beam was aligned and fixed parallel to the axis of rotation, enabling the measurements of $\epsilon_{a'}$ and crystal rotation angle without the need for slow goniometer scans. Thus, the time spent at each position is cut from ≈ 15 minutes to ≈ 1 s. Diffraction images were taken over time at positions with increased spatial resolution in an 11×15 grid ($x \times y$) spanning 2.0 mm $\times 1.4$ mm. As such, $\Delta y = 0.1$ mm. A type B crystal of $\phi_0 = 0.39$ was used in the following experiments.

The spatial distribution of lattice constant strain is revealed by colouring the individual strain values at each x and y position, $\epsilon_{a'}(x, y)$, at time $t = 12$ hrs in Fig.4.6a. It is clear that there is a strong dependence in y for the lattice strain. The time evolution of $\epsilon_{a'}$ is presented in Fig.4.6b, where the different lines represent different times in the experiment. We see a time and height dependence that supports the observations in Fig.4.4a, where $\epsilon_{a'}$ decreases most quickly at the bottom of the crystal, but expands slightly higher up. The higher spatial resolution shows that the highest gradient in $\epsilon_{a'}$ with respect to y and therefore, highest shear strain, is at the bottom of the crystal.

Next, we explicitly measure $\gamma_{a'}$ using equation 4.4 to observe its spatial distribution.

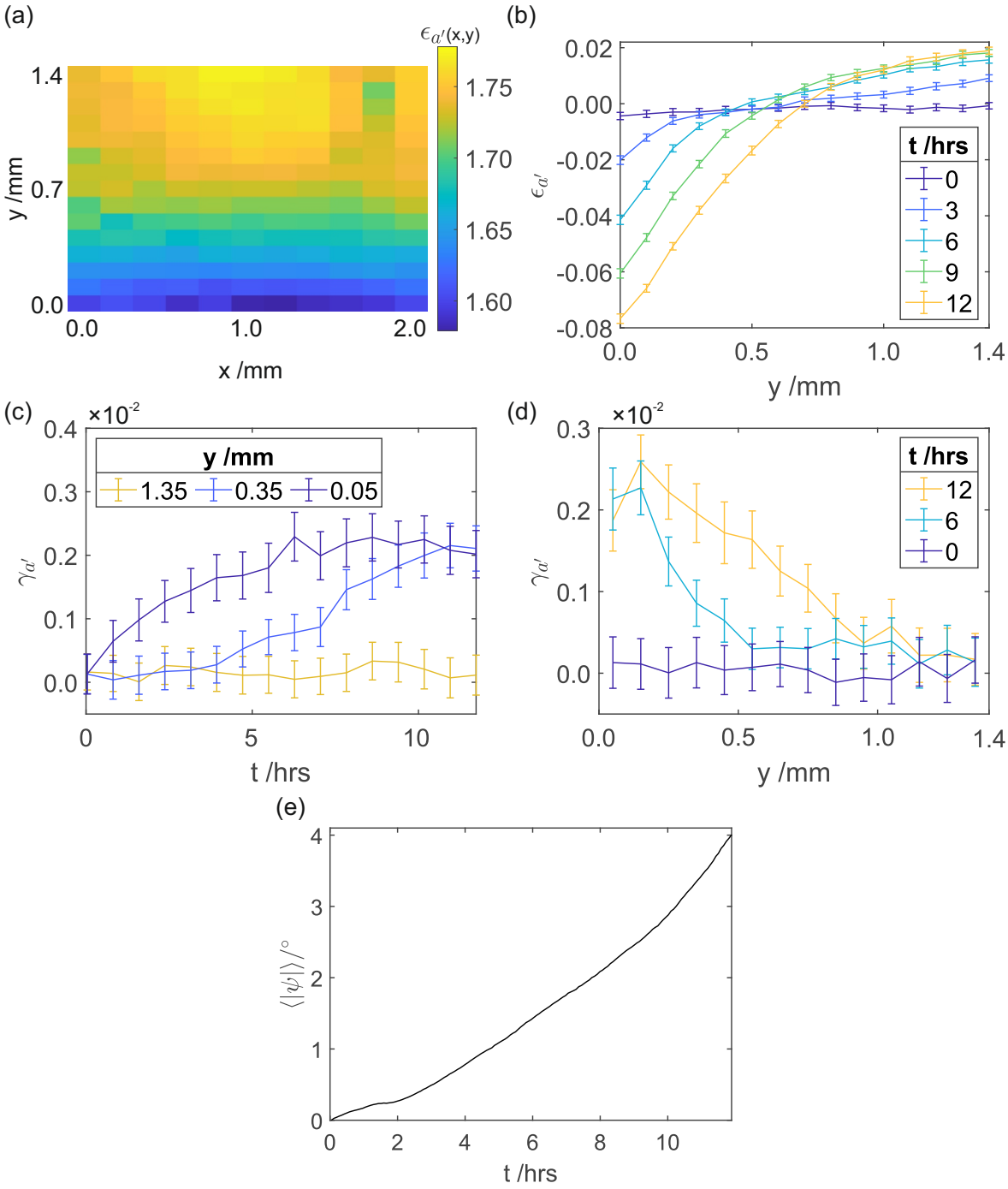


Figure 4.6: (a) Strain in lattice constant a' for each irradiation position in the xy grid. The value at each position is given a colour as indicated by the colour bar. (b) Lattice constant strain against y for different times in the experiment. (c) Local shear strain against time for different y. (d) Local shear strain against y at different times. The above results are for a type B colloidal crystal $\phi_0 = 0.39$. The shear strain is measured between successive a' measurements, 0.1 mm apart in y, and the standard error is calculated as described in appendix 4.5.1. (e) Mean rotation angle magnitude for the field of view as a function of time.

Fig.4.6c and d show the local shear strain as a function of time for separate y positions and as a function of y for different times, respectively. The value of shear strain increases most quickly near the bottom of the crystal, $y = 0.05$ mm and then reaches a plateau at a shear strain of $\gamma_{a'} \approx 2 \times 10^{-2}$. Slightly higher in the crystal at $y = 0.35$ mm, the shear strain rises after a lag time of $t \approx 4$ hrs, and then rises to a similar plateau value $\gamma_{a'} \approx 2 \times 10^{-2}$. The lag time is again due to the speed at which the densification front rises through the crystal. High up in the crystal, at $y = 1.35$ mm, the local shear strain stays constant and small throughout the experiment. The densification front does not reach this height by the end of the experiment and, therefore, no local shear strain occurs. To examine the onset of rotations in the crystal we measure the rotation at each position. The average rotation magnitude in the field of view, $\langle|\psi|\rangle$ is plotted against time in Fig.4.6e. Importantly, Fig.4.6e shows that rotations begin at early time, when local shear strain is only exhibited at the bottom of the crystal, as shown in Fig.4.6c. Therefore, shear at the bottom of the crystal is responsible for rotations, and as such, will be examined for different initial volume fractions of crystals in section 4.3.5.

4.3.4 Spatial distribution of crystal rotation

Next, we examine the spatial distribution of rotations over the entire field of view. The rotation angles at individual positions in the $x \times y$ grid at $t = 12$ hours are shown in Fig.4.7a. Both clockwise and anticlockwise rotations, positive and negative ψ, respectively, are observed across the field of view. Looking at the rotations at the bottom of the crystal at $y = 0$ mm, we see both positive and negative values of ψ which are a result of cooperative motion in different directions. Therefore, cooperative motion on a length scale roughly equal to the width of the field of view, 2.0 mm (see Fig.4.7a) is required to initiate fracture. Consequently, the number of cooperatively moving unit cells, N, observed in crystallite rotation is on the order of magnitude of $N = \frac{2.0\times10^{-3}\text{ m}}{a'} = \frac{2.0\times10^{-3}}{1.8\times10^{-6}} \approx 10^3$ unit cells (see section 3.4.1 for evaluation of a'). This is roughly an order of magnitude larger than the number of unit cells parallel to z, being $\frac{0.1\times10^{-3}\text{ m}}{1.5\times10^{-6}\text{ m}} \approx 10^2$ unit cells, corroborating the lack of rotations observed with axes parallel to the x axis. Since a' corresponds to one particle separation we can express N equivalently as the number of cooperatively moving particles. The distribution in rotation angles shown in Fig.4.7a shows that rotations occur high up in the crystal, in spite of the low local shear (see Fig.4.6c and d). Furthermore, the mean rotation angle magnitude at each height (see Fig.4.7b) shows that

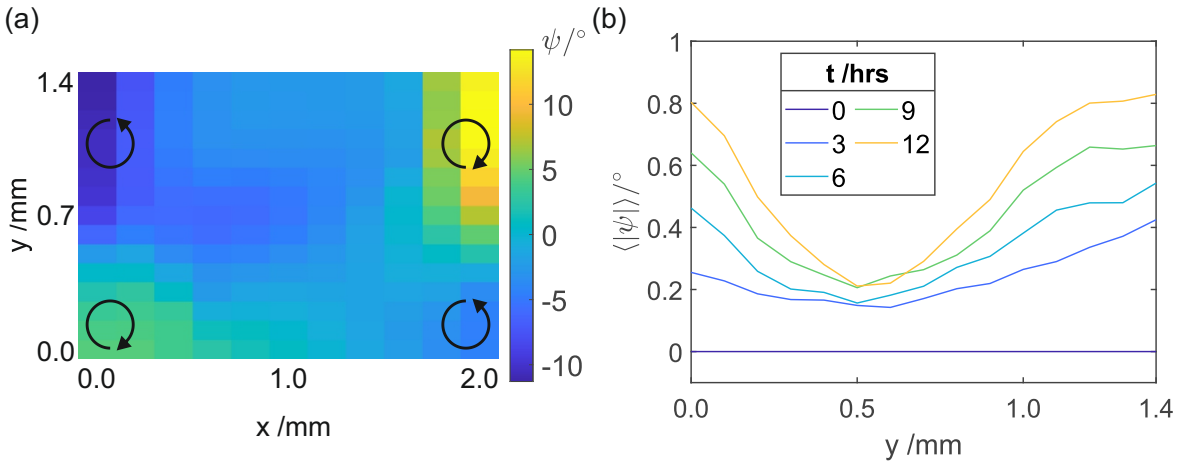


Figure 4.7: (a) Local rotation angle plotted at each irradiation position in the xy plane. (b) Mean rotation of from each irradiation position.

the rotations high up in the crystal, $y > 1.2$ mm, increase at the same rate as at the bottom of the crystal, $y = 0$ mm. Notice that the domains of rotation high in the crystal display rotations with opposite direction, i.e. ψ of opposite sign, to those directly below them, lower in the crystal. This indicates that rotations propagate upwards in the crystal by the counter rotating domains acting like meshing gears.

4.3.5 Initial volume fraction influence on fracture

Our previous observations suggest that crystal rotation can be controlled by modifying the value of $\gamma_{a'}$, as long as N, the number of crystal unit cells moving cooperatively to generate the shear, is on the order of 10^3. To examine this prediction, we modify $\gamma_{a'}$ by changing the initial volume fraction of the RHCP crystals. A higher volume fraction means that colloidal particles are closer together in the crystal. As a result, lattice constants have less capacity to shrink, therefore, reducing values of $\gamma_{a'}$. As such, the model predicts that crystal rotation should be suppressed by increasing the initial volume fraction.

The measurements of crystal deformation at high resolution were repeated for different volume fractions, and the local shear strain was calculated. Fig.4.8a shows the local shear strain at the bottom of the crystal, $\gamma^{\mathrm{f}}_{a'}$, for initial volume fraction crystals of, $\phi_0 = 0.39, 0.41$ and 0.46. The superscript f indicates the shear strain at the bottom i.e. the foundation of the crystal. We observe that the local shear at the bottom of the crystal is, in fact, lower for the highest initial volume fraction, $\phi_0 = 0.46$, crystal. The increase in ϕ does slightly increase the number of unit

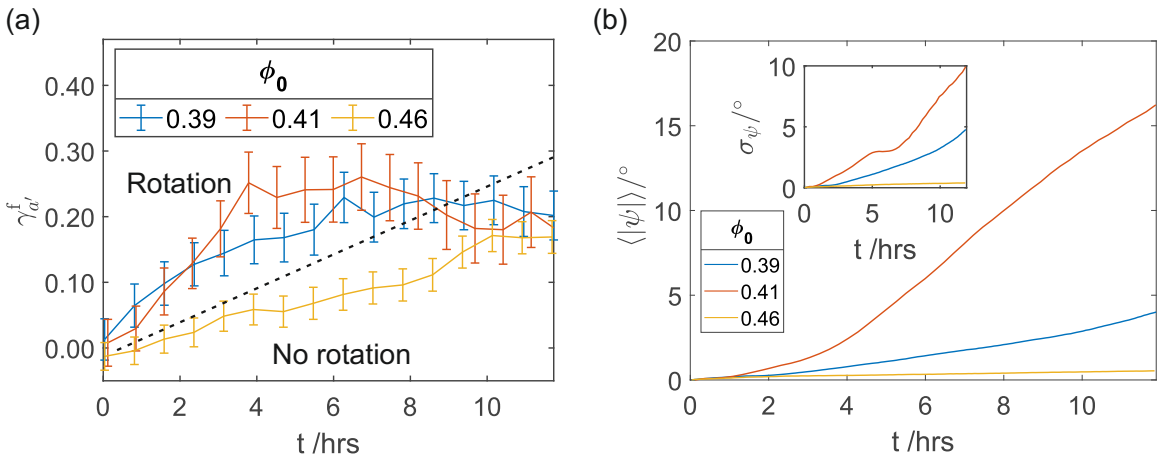


Figure 4.8: (a) Local shear strain at the bottom of the crystal, $\gamma^{f}_{a'}$, plotted against time for several crystals with different initial volume fractions. (b) Mean magnitude of rotation angles, $\langle|\psi|\rangle$, over time for several initial volume fractions. The inset shows the standard deviation in rotation angles within the field of view over time.

cells in each direction. In any case, the number of unit cells along z remains confined to an order of magnitude lower than the approximately 10^3 in the x direction observed in crystallite rotations. Therefore, combined with the lower γ, we do not expect crystal rotations with an axis of rotation parallel to the x axis. As the model predicts, crystal rotations are suppressed for higher volume fractions, as shown in Fig.4.8b. The mean magnitude of rotation angle is greater at each time for the lower initial volume fraction crystals, $\phi_0 = 0.39$ and $\phi = 0.41$, but for $\phi_0 = 0.46$, the rotation angle remains very small throughout the experiment. The standard deviation in rotation angle, σ_ψ, over the field of view is plotted in the inset of figure 4.8b. Lower volume fraction crystals display higher σ_ψ showing the formation of crystallites with differing rotation angles. Note that the magnitude of $\gamma^{f}_{a'}$ for the $\phi_0 = 0.46$ does reach values that initiate rotational fracture in the lower volume fraction crystals, yet, rotations remain suppressed. In fact, it is apparent from Fig.4.8a that a higher shear strain rate, the gradient of $\gamma^{f}_{a'}$ with respect to time is required to initiate rotational fracture of the crystal, as indicated by the dotted line in Fig.4.8a. Therefore, we modify the model so that a high shear strain *rate*, γ', exhibited by many cooperatively moving unit cells, N, is necessary for crystal rotation. For the colloidal crystals studied in this chapter, provided that the number of unit cells along a particular direction is approximately 10^3 and that the shear strain rate is approximately 7×10^{-8} s^{-1}, crystal rotation occurs. It seems possible that crystal rotation may be initiated for small N for much higher γ', which may be investigated by increasing the effect of gravity, perhaps by employing colloidal particles made from a more dense material such as silica. In this case, we may also expect to see components of rotation with axes parallel to the x axis.

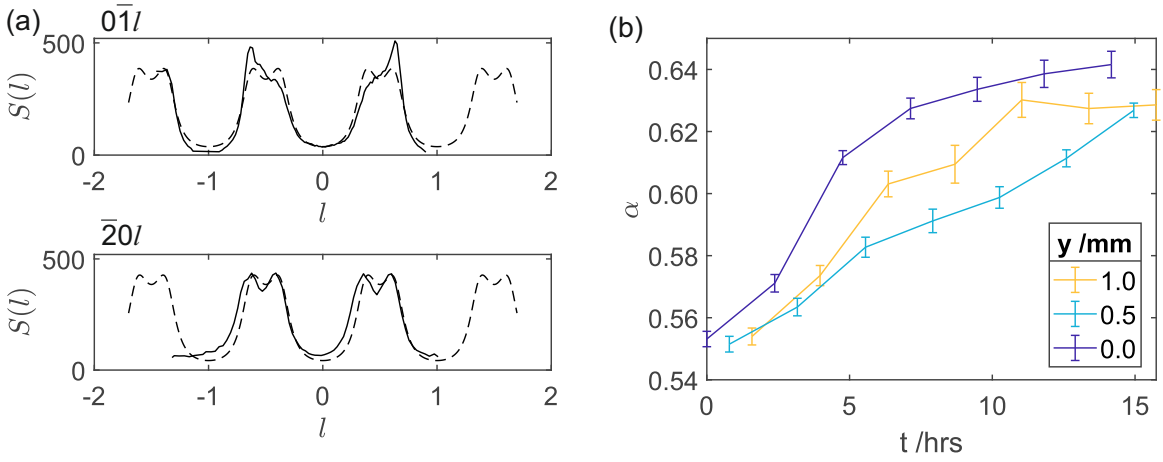


Figure 4.9: (a) Structure factor, $S(l)$, variation with l for example Bragg rods of different orders, $(0\bar{1}l)$ and $(\bar{2}0l)$ shown by the solid line. The dotted line shows the fit to Wilson theory. (b) Stacking parameter, α, over time for several heights in y. The error bars show the standard error.

4.3.6 Change of hexagonal stacking over time

In tandem with the lattice constant change and crystal fracture we also observe an evolution of the stacking parameter, α, from the goniometer scans over time. As before, α is calculated by fitting the intensity variations along Bragg rods to Wilson theory given in equation 3.10 of section 3.3.3 with details found in appendix 3.6.2. The structure factor variation $S(l)$ along Miller index l for Bragg rods at $t = 12$ hrs is shown for a 1^{st} and 2^{nd} order Bragg rod in Fig.4.9a. Notice how the shape of the variation has changed to include double peaks instead of the single peaks observed at early time as shown in Fig.3.6e, showing that the proportion of FCC has increased. The values of α over time at different heights in the crystal are shown in Fig.4.9b. At each height α increases showing an increased FCC proportion in the RHCP crystals.

4.4 Conclusion

We have used SAXS and CLSM to probe the evolution of shear-aligned colloidal crystals over time. Rotational fracture is initiated when the $\vec{G}_{1\bar{1}0}$ reciprocal lattice direction is aligned with gravity and given a low enough initial volume fraction. The rotational crystal fracture occurs exclusively with rotation axes parallel to the z axis. i.e. perpendicular to the hexagonal planes. Therefore, we demonstrate a pathway to create colloidal polycrystals with exclusively tilt grain boundaries. Next, we used spatially resolved SAXS measurements to reveal local shear strain in lattice constants and proposed a model for rotational crystal fracture. We suggest that high

local shear strain rates (with respect to time) amplified by cooperatively moving crystal unit cells induce crystal rotation and that rotational motion propagates upwards through the crystal to create rotations and fracture throughout. We examined how a higher volume fraction decreases shear strain rates (with respect to time), however, we suspect shear strain rates can be reduced in other ways, for example, by increasing the viscosity of the solvent or by lessening the effect of gravity by means of solvent particle density matching. We suspect that rotation axes parallel to the x axis can be initiated for crystals with a larger number of unit cells in the z direction. What remains unclear from our experiments is the mathematical relationship between cooperatively moving particles, shear strain rate and crystal rotation. It may be the case that large rotations only occur above critical number of cooperatively moving particles, and or above a critical strain rate, and or a critical value of some product of the two. Careful control of crystal confinement and shear rates may prove enlightening in this regard. Finally, the evolution of the structure factor variations of Bragg rods over time showed an increased preference for FCC over HCP, which is encouraging for the pursuit of colloidal crystals with photonic band gaps. The behaviour of these RCHP crystals can be controlled so as to maintain an orientational monodomain or to produce an exclusivley tilt grain boundary polycrystal via rotational fracture.

4.5 Appendix

4.5.1 Errors

Error propagation was performed using the result for the uncorrelated random (normal) errors. For two functions $f(x)$ and $f(y)$ with associated population standard deviations σ_x and σ_y, the population standard deviation for the function $g(x, y)$ is given by:

$$\sigma_g \approx \sqrt{\left(\frac{\partial g}{\partial x}\right)_y^2 \sigma_x^2 + \left(\frac{\partial g}{\partial y}\right)_x^2 \sigma_y^2}. \tag{4.5}$$

The standard error is calculated from the standard deviation as:

$$\varepsilon = \frac{\sigma}{\sqrt{N}}, \tag{4.6}$$

where N is the number of measurements. Substitution of equation 4.6 into 4.5 we arrive at

$$\varepsilon_g \approx \sqrt{\left(\frac{\partial g}{\partial x}\right)_y^2 \varepsilon_x^2 + \left(\frac{\partial g}{\partial y}\right)_x^2 \varepsilon_y^2}, \tag{4.7}$$

which is valid if the number of measurements of $f(x)$ and $f(y)$ are the same or approximately equal.

Lattice strain

The standard deviation on the strain, σ_ϵ, is calculated from the standard deviation of the lattice constant measurements at time t and y, σ_a, and the standard deviation in the lattice constant at initial time, σ_{a_0}, using error propagation of uncorrelated normally distributed random errors as described above. Substitution of equation 4.1 into equation 4.7 yields:

$$\varepsilon_\epsilon = \sqrt{\left(\frac{1}{a_0'}\right)^2 \varepsilon_{a'}^2 + \left(\frac{-a'}{a_0'^2}\right)^2 \varepsilon_{a_0'}^2}. \tag{4.8}$$

The standard error is used for the error bars: $\epsilon_a' \pm \varepsilon_\epsilon$. Note that the number of measurements for the lattice constant is not always equal as some peaks fail to be identified. Furthermore, the number of measurements of a_0' is much higher than for a' at each time. Nonetheless, this provides a good approximation to the standard error on the strain. The lattice constant strain errors are calculated in an identical fashion for b' and c.

Volume fraction

Similarly we find the standard error on the volume fraction to be:

$$\begin{aligned} \varepsilon_\phi &= \frac{4\pi r^3}{3a'b'c}\sqrt{\varepsilon_{a'b'}^2 c^2 + \varepsilon_c^2 (a'b')^2}, \quad \text{where} \\ \varepsilon_{a'b'} &= \sqrt{\varepsilon_{a'}^2 b'^2 + \varepsilon_{b'}^2 a'^2}. \end{aligned} \tag{4.9}$$

Local shear strain

We assume that the error in y is negligible compared to the errors in a'_1 and a'_2 and, as such, calculate the standard deviation in $\gamma_{a'}$ as:

$$\varepsilon_{\gamma_{a'}} = \sqrt{{a'_1}^2 \varepsilon^2_{a'_2} + {a'_2}^2 \varepsilon^2_{a'_1}}. \tag{4.10}$$

The error bars show $\gamma_{a'} \pm \varepsilon_{\gamma_{a'}}$ where $\varepsilon_{\gamma_{a'}}$ is the standard error.

Acknowledgements

The SAXS experiments were performed in collaboration with T. Yanagishima and A. V. Petukhov. Special thanks to I. P. Dolbnya for preparing the unique microradian x-ray diffraction setup at B-16 at Diamond Light Source, Didcot, UK. Daniel Bell is acknowledged for taking the rotational fracture CLSM data.

Chapter 5

Grain boundary characterisation from particle coordinates

Abstract

We present a method to locate and characterise grain boundaries in polycrystalline materials from the real space coordinates of their constituent particles. The method is robust against imperfections such as thermal noise and vacancies. We apply the method to experimentally obtained real space coordinates to explicitly measure local misorientations and structure at grain boundaries. We consider particle coordinates obtained from an epitaxially templated colloidal $\Sigma 17$ bicrystal, finding that, even though the bicrystal is predominately $\Sigma 17$ and face centered cubic, small volumes of hexagonally closed packed structure generate a mosaic of grain boundaries, increasing the complexity of the templated grain boundary. We also consider a homogeneously nucleated colloidal polycrystal and apply our method with no prior knowledge of grain boundary structure. Accordingly, we reveal detailed misorientation distributions and grain boundary structures. The method may be applied to any set of coordinates of atoms or particles in a polycrystalline system.

5.1 Introduction

Most crystalline materials in nature are polycrystalline, consisting of differently oriented crystallites packed together to create a network of grain boundaries at their interfaces. The structure of the grain boundary network has a profound impact on the macroscopic material properties and underlie much of our understanding of ductility, brittleness, electrical conductivity, deformation and fracture mechanisms [123], melting kinetics [117, 124, 125], and transport properties [126] in a wide range of materials [127]. Much effort has been made in recent decades to tune the grain boundary structure within materials by so called 'grain boundary engineering' which can involve sintering, rolling and annealing of metals, alloys and ceramics. In some cases, materials with small grains and many grain boundaries are desirable as they cause a dramatic increase in strength following the Hall-Petch law [39, 40]. In other cases, large single crystals are required, with examples including structure solution in single crystal crystallography and for the manufacture of photonic band gap crystals [47, 128, 129].

The properties of the grain boundaries themselves are governed by their degrees of freedom. In three dimensions (3D) these consist of: three for position, three for the orientation difference between the different crystallites, termed misorientation, and two for the plane of the boundary relative to the crystal lattice, known as inclination [130]. The distribution and type of grain boundary has been shown to affect the migration kinetics of boundaries under stress [131] and during grain growth [132, 133]. Additionally, grain boundary mobility, surface tension and roughening transitions are affected by the interplay between misorientation and inclination [134].

A wealth of research on materials yields structural information in reciprocal space using scattering techniques such as orientation imaging microscopy [135, 136], diffraction contrast microscopy [137–140], electron backscatter diffraction [141, 142] and 3D X-ray diffraction [143, 144]. However, one is either required to destroy the sample by serial sectioning, preventing dynamic measurements, or to prioritise between spatial, angular or time resolution [145]. The spatial resolution of these techniques limits the size of the grains to roughly 1 μm [140, 145], orders of magnitudes larger than the size of the atoms themselves, making it impossible to comment on how the behaviour of specific boundaries are tied to atomistic dynamics or arrangements. Furthermore, achieving measurements of grain boundaries in the bulk is difficult as one must have a sample thick enough to render surface effects negligible, but not so thick that scattering

peaks from multiple grains overlap [145]. Thus, there are significant advantages to studying the *real space* coordinates of atoms, molecules or mesoscopic particles over space. Real space coordinates are increasingly widely available, from electron microscopy studies [146] and simulations [147, 148], to mesoscopic model systems such as colloidal dispersions [57, 76], where optical microscopy can give the coordinates of all particles in bulk within a field of view [80]. There are advantages to the latter two techniques over electron microscopy techniques. Firstly, three-dimensional reconstruction of structure using electron microscopy once more requires serial sectioning which destroys the sample, preventing dynamic measurements; and secondly, electron microscopy is necessarily a surface technique meaning that surface effects must be ruled out from measurements.

With the availability of three-dimensional coordinates, there is an increasing need for a robust means to extract the location and properties of grain boundaries from real space data. However, existing grain and boundary detection schemes offer only a partial analysis. Some schemes use order parameters to locate grain boundaries [149, 150] and by doing so neglect to measure orientation. Polyhedral template matching [151], used in the OVITO software [152], allows orientation measurement and grain resolution but neglects grain boundary surfaces or local resolution of misorientations at the grain boundaries [153]. Many detection schemes are only useful in specific contexts e.g. where a system is constrained to only one or one type of grain boundary and the orientation of one or more of the grains is known beforehand [57,148,154–157]. Taming grain boundaries like this is beneficial because it reduces their complexity. However, the resulting boundary properties only apply to themselves [133] because forces associated with ever present neighbouring grain boundaries are neglected.

Here, we present a generally applicable method to fully identify and characterise crystalline grains, crystalline structures and to render grain boundaries using real space particle coordinates. We apply the method to real space coordinates of colloidal particles in dense crystalline dispersions. The method is shown to be robust against thermal noise as well as defects in the crystals, and to provide exhaustive information on both the location and orientation of several kinds of boundary. Importantly, we also provide a means to locally characterise the degree of misorientation between grains at different locations on the grain boundary surface, giving unprecedented access to the range of structures present.

This chapter is organised as follows. Section 5.2 covers theoretical aspects of orientations

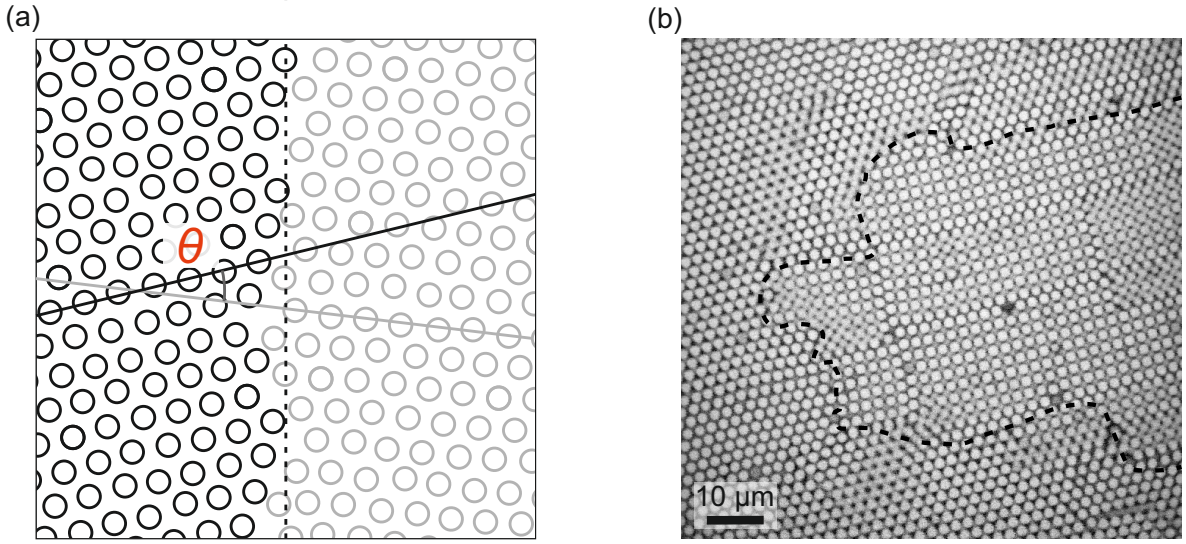


Figure 5.1: (a) Illustration of a 2D grain boundary between two grains in black and grey respectively. The misorientation is marked by θ. The dotted line roughly marks the boundary. (b) 2D confocal microscopy image of a 3D grain boundary. The dotted line roughly marks the boundary.

and crystal symmetry. Subsequently, section 5.3 details the grain and grain boundary characterisation method. Section 5.4 then shows its application where we uncover unprecedented detail in the grain and grain boundary structure of both a templated colloidal bicrystal and a polycrystalline colloidal crystal.

5.2 Theory

A grain boundary is the intersection between two differently oriented crystallites [134, 158]. In two dimensions, grain boundaries have 4 degrees of freedom, one for the misorientation, another for the orientation of the boundary with respect to the crystal lattice, and the final two for the position in space. In three dimensions the situation becomes more complicated with the degrees of freedom extending to eight. In this case there are three for misorientation, two for inclination and three for position in space. Fig.5.1a and b show an illustration of a 2D and an image of a 3D grain boundary in a colloidal crystal, respectively. The 3D boundary looks to be between two different crystal structures, however, this is simply because the appearance of the crystal depends on the crystal orientation.

5.2.1 Orientation, misorientation and symmetry

A challenging aspect in describing grain boundaries in 3D is the interplay between the symmetry of the crystallites and the rotations that describe their orientations. Firstly, the mathematics underpinning the description of rotations is outlined, followed by the consequences of introducing crystal symmetry. Finally graphical representation for visualising orientations is discussed.

Orientation

An orientation is defined as a rotation with respect to a reference and, as such, the mathematics that applies to rotations may also be applied to orientations. Three-dimensional rotations have a couple of important characteristics: they have 3 degrees of freedom and are non-commutative, meaning that the order of rotations in a sequence matters.

There are many ways to describe 3D rotations including, rotation matrices, Euler angles, angle axis, Rodrigues-Frank vectors and quaternions [158, 159], and a brief discussion of their form and utility follows. Firstly we consider rotation matrices, which are a D by D array of numbers where D is the dimension of the rotation. For rotations in 2D, $D = 2$ and in 3D, $D = 3$, therefore a 3D rotation matrix $\mathbf{M}$ takes the form:

$$\mathbf{M} = \begin{pmatrix} m_{11} & m_{12} & m_{13} \\ m_{21} & m_{22} & m_{23} \\ m_{31} & m_{32} & m_{33} \end{pmatrix}. \tag{5.1}$$

Matrix representation suffers from a couple of disadvantages. Firstly, it contains degenerate information (9 elements for 3 degrees of freedom) and secondly, it is not immediately intuitive what kind of rotation the matrix describes. Another representation of rotations are the three Euler angles, α, β, γ, [158]. These angles pertain to a sequence of three rotations about a selection of axes. There are several definitions for which axes are used and in which order. While Euler angles offer a more intuitive description of the rotation, Euler angle representation suffers upon consideration of rotational symmetry, as orientation space becomes warped and distorted inside fundamental zones (see section 5.2.2) of orientation with complicated shapes.

Arguably the most intuitive representation of rotations is the angle axis form. It is built

from Euler's observation that any rotation may be described by a rotation of angle, θ, about some axis $\vec{A}$, and herein, we use the right-hand screw convention. It is more intuitive than Euler angles as its description relies on only one rotational motion about a single axis. Angle axis representation takes the form:

$$\begin{aligned} R_{\mathrm{AA}} &= (\theta, A_x, A_y, A_z), \\ \vec{A} &= (A_x, A_y, A_z), \\ |\vec{A}| &= 1, \end{aligned} \tag{5.2}$$

where $\vec{A}$ is a normalised vector parallel to the axis of rotation. For example a 90° rotation about the x axis is written as:

$$R_{\mathrm{AA}} = (90, 1, 0, 0). \tag{5.3}$$

While this representation is intuitive, it still suffers from containing degenerate information. The degeneracy may be removed by creating the angle axis vector, $\vec{R}_{\mathrm{AA}}$:

$$\vec{R}_{\mathrm{AA}} = \theta\vec{A}. \tag{5.4}$$

The greater the magnitude of the vector, the larger the rotation. Next we consider the Rodrigues-Frank vector [160, 161], $\vec{RF}$, which builds on the angle axis representation. Degeneracy is removed in a similar way to before by modifying the length of the rotation axis vector. However, in this instance, this is achieved by multiplication by the tangent of half the rotation angle:

$$\begin{aligned} \vec{RF} &= \vec{A}\tan\frac{\theta}{2} \\ &= (RF_x, RF_y, RF_z). \end{aligned} \tag{5.5}$$

Again, the greater the magnitude of the Rodrigues-Frank vector, the larger the rotation about an axis parallel to vector. The Rodrigues-Frank vector has a significant advantage in the visualisation of rotations for objects with rotational symmetry (greater than or equal to order 2). This is discussed in more detail in section 5.2.1. We use Rodrigues-Frank vectors to visualise orientations in this chapter, as discussed in detail later.

Finally we consider quaternions. Quaternions are a 4 tuple consisting of a real, *scalar* part

and an imaginary, *vector* part. They are often presented as a sum of their components [162]:

$$\begin{aligned} q &= w + xi + yj + zk \\ &= [w, v], \end{aligned} \tag{5.6}$$

where w is the scalar part and $v = xi + yj + zk$ is the vector part. They can be viewed as a four dimensional vector, but for ease of notation we will simply write them as q. The magnitude of a quaternion is calculated in a similar way to the magnitude of a 3D vector:

$$|q| = \sqrt{w^2 + x^2 + y^2 + z^2}. \tag{5.7}$$

Unit quaternions have a magnitude $|\vec{q}| = 1$ and are advantageous because they are more efficient and convenient way to compute rotations. Quaternions may be written in an alternative *angle axis* form which makes their use for rotations more clear:

$$q = \cos(\theta/2) + \sin(\theta/2)(xi + yj + zk), \tag{5.8}$$

where θ is the angle of rotation about the axis (x, y, z).

Computing rotations

Both rotation matrices and quaternions may be used as rotation operators to compute rotations. Here, we will consider two operations: successive rotations and the rotation of a point. Successive rotations, where one is performed after the other are computed as:

$$\mathbf{O}_{12} = \mathbf{O}_1\mathbf{O}_2, \tag{5.9}$$

where $\mathbf{O}$ represents the rotation operator. In the following, we will consider the operator to be a quaternion. As such, the process of quaternion multiplication must be specified. Taking the scalar and vector form of each quaternion, multiplication is defined as:

$$q_1 q_2 = [w_1 w_2 - v_1 \cdot v_2, w_1 v_2 + w_2 v_2 + v_1 \times v_2] \tag{5.10}$$

where $\cdot$ represents the dot product and $\times$ the cross product. The rotation of a point, represented by $p = (p_1, p_2, p_3)$ may be expressed as:

$$p_\mathrm{r} = \mathbf{O}p, \tag{5.11}$$

where p_r is the rotated point. In the case of quaternions, p is rotated by creating quaterion $q_\mathrm{p} = p_1 i + p_2 j + p_3 k$ with 0 scalar part and vector part formed from the components of p. p_r is calculated as [162]:

$$p_\mathrm{r} = q q_\mathrm{p} q^{-1}, \tag{5.12}$$

where the quaternion multiplication defined in equation 5.10 is applied. The vector part of the resulting quaternion is p_r, representing the rotated point. Note that the conjugate of q, expressed as q^{-1}, is defined as [162]:

$$q = w - xi - yj - zk. \tag{5.13}$$

The machinery of the grain and grain boundary detection method uses quaternions to compute rotations efficiently.

Symmetry equivalent orientations and misorientations

Any object can be rotated by 360° about any axis and appear to be unchanged. However, for objects possessing rotational symmetry, this can happen at a lower rotation angle provided the rotation is about some special axis known as a symmetry axis. This means that there are multiple symmetry equivalent ways to describe the orientation of objects with rotational symmetry, one for each of the members of the proper rotational symmetry group, $\{S\}$, defined as:

$$\{S\} \equiv \{S_i\}_{i \in \{1 \ldots n\}} \tag{5.14}$$

where S_i is a symmetry element and n is the number of symmetry elements. The elements are in fact themselves rotations. The set of symmetry equivalent orientations represented as rotation operators,$\{\mathbf{O}\} \equiv \{\mathbf{O}_i\}_{i \in \{1 \ldots n\}}$, can be generated from one description of the orientation using

equation 5.9. As such, symmetry equivalent rotations are calculated as:

$$\mathbf{O}_i = S_i\mathbf{O}, \tag{5.15}$$

where S_i is a symmetry element and may be expressed as a rotation matrix or a quaternion. Misorientations are the relative rotations between two objects and are independent of reference. A misorientation between two crystal orientations $\mathbf{O}_1$ and $\mathbf{O}_2$ is calculated using equation 5.9 where taking the inverse of $\mathbf{O}_2$ removes the the dependence on the reference [159]:

$$\mathbf{O}_{12} = \mathbf{O}_1\mathbf{O}_2^{-1}, \tag{5.16}$$

where $\mathbf{O}_2\mathbf{O}_2^{-1} = \mathbf{I}$, the identity operator, i.e. the inverse is the operator that performs the reverse rotation. For quaternions, the inverse operation is given by the conjugate, and is expressed as q^{-1}. Symmetry equivalent misorientations are formed by substituting equation 5.15 in to equation 5.16. Let the set of symmetry equivalent misorientations of $\mathbf{O}_{12}$ be $\{\mathbf{O}_{12}\} \equiv \{\mathbf{O}_{ij}\}_{i\in\{1\ldots n\},j\in\{1\ldots m\}}$, where n and m span the elements of the rotational symmetry groups of crystal 1 and crystal 2, $\{S^a\} \equiv \{S_i^a\}_{i\in\{1\ldots n\}}$ and $\{S^b\} \equiv \{S_j^b\}_{j\in\{1\ldots m\}}$, respectively, which may be the same, or different. Thus, the members of the set of symmetry equivalent misorientations are given by [163],

$$\begin{aligned}\mathbf{O}_{ij} &= S_i^a\mathbf{O}_1(S_j^b\mathbf{O}_2)^{-1} \\ &= S_i^a\mathbf{O}_1\mathbf{O}_2^{-1}(S_j^b)^{-1}.\end{aligned} \tag{5.17}$$

Using the group property inverse, $(S_j^b)^{-1}$ may be replaced by S_j^b to give:

$$\mathbf{O}_{ij} = S_i^a\mathbf{O}_{12}S_j^b, \tag{5.18}$$

leaving the set $\{\mathbf{O}_{12}\}$ unchanged. This generates $n \times m$ symmetry equivalent misorientations, where n and m are the number of elements of the rotational symmetry groups belonging to crystals 1 and 2, respectively. When crystals 1 and 2 are of the same symmetry, it does not matter whether the misorientation corresponds to a rotation from crystal 1 to 2 or vice versa. Therefore the inverse misorientations, $(O_{ij})^{-1}$, are equivalent and the number of symmetry equivalent representations doubles to $n \times m \times 2$. However, this is not the case when crystals 1 and 2 do not have the same symmetry. Here, O_{ij} are given by the rotations that map the crystal

with lower symmetry onto the crystal with higher symmetry following the convention given by Heinz and Neumann [163].

5.2.2 Visualising orientations and misorientations

Of the representations discussed above, the Euler angles, the angle axis vector and the Rodrigues-Frank vectors are composed of only three components. An orientation space may be created where the components span three orthogonal axes and an orientation is represented by a point. The most convenient space to use for our purposes is that created by Rodrigues-Frank vectors. This is because the bounding surfaces of zones containing only one symmetry equivalent orientation are planar instead of curved [164], as is the case for Euler angles and angle axis vectors. Conventionally, only the symmetry equivalent representation with the lowest rotation angle is given [158, 163]. In the case of misorientations, there may be equivalences with the same smallest rotation angle but different axes. We adopt the conventions for the standard stereographic triangle set out in the work by Heinz and Neumann [163]. They consist of a set of inequalities selecting one of a set of equivalent misorientation fundamental zones. Grain boundary misorientations presented in the results and discussion section 5.4 will be given as Rodrigues-Frank vectors within fundamental zones of misorientation, as defined below. Misorientation angle distributions also visualise misorientations, where histograms of misorientation angle, θ, within the Rodrigues-Frank misorientation fundamental zone are plotted as defined in equation 5.5.

Fundamental zones

Fundamental zones contain only one from a group of symmetry equivalent orientations. Accordingly, they are useful to plot orientation and misorientation distributions. Included in Fig.5.2 are a selection of orientation and misorientation fundamental zones in Rodrigues-Frank representation. The planar surfaces in Rodrigues-Frank space make plotting fundamental zone boundaries simple. However, it is important to note that Rodrigues-Frank fundemantal zones are finite only if the rotational symmetry is at least order 2. Without rotational symmetry i.e. symmetry order 1, the fundamental zone extends from $-\infty$ to $+\infty$. In this case a switch to angle axis representation is preferable, however for our purposes we will only consider cases with symmetry above order 2.

Figures 5.2a and b show orientation fundamental zones for objects with rotational point group O and D_6 symmetry, respectively. Each of the bounding planes correspond to one of the symmetry elements of the rotational symmetry group, and are normal to axes of rotational symmetry. For example, the octagonal faces of the O fundamental zone in Fig.5.2a correspond to the C_4 rotational symmetry elements, and accordingly these faces sit at $2\tan^{-1}(0.4142) = 45°$ (see equation 5.5) away from the origin, generating 90° rotation between opposite faces, marking the equivalence of such a rotation of a crystal with C_4 symmetry. Likewise, the triangular faces sit at $2\tan^{-1}(0.5774) = 60°$ (see equation 5.5) away from the origin. The C_2 symmetry elements are not observed in the O fundamental zone because their corresponding planes sit further away from the origin than do the others, however, they are seen in the D_6 orientation (and misorientation) fundamental zones (see Fig.5.2b and e, respectively) as the rectangular faces with normals perpendicular to the RF_z axis. The identity operator exists not as a plane, but as a singularity at the origin.

Figures 5.2c-e contain the misorientation fundamental zones corresponding to misorientations between crystals with O, D_6 and O, and D_6 symmetry, respectively. These have a smaller volume owing to misorientations being constrained by symmetries of both crystals. For example, Fig. 5.2c shows the fundamental zone between two crystals of O symmetry. The volume of this space is 24×2 times smaller than the O orientation fundamental zone. 24 for each symmetry element and the factor of 2 from the rotations from crystal 1 to 2 and vice versa being equivalent. The bounding surfaces of these spaces relate to combinations of symmetry operators between two crystal symmetries.

Figure 5.2f shows the fundamental zones from a to e superimposed to aid the reader to establish spatial relationships between these spaces. Both the fundamental zones of misorientation between O and between O and D_6 crystals entirely fit inside the the O orientation fundamental zone. Likewise the fundamental zone of misorientation between D_6 symmetry crystals fits entirely inside the D_6 orientation fundamental zone. The orientation fundamental zones for O and D_6 extend along different directions to different extents to reflect the order of symmetry in those directions. The reader is reminded that length of a Rodrigues-Frank vector corresponds to $\tan\left(\frac{\theta}{2}\right)$ (see equation 5.5), so, a fundamental zone exhibiting a shorter extent in some direction corresponds to a higher order of symmetry along that same direction.

Practically, fundamental zones enable the comparison of orientations and misorientations.

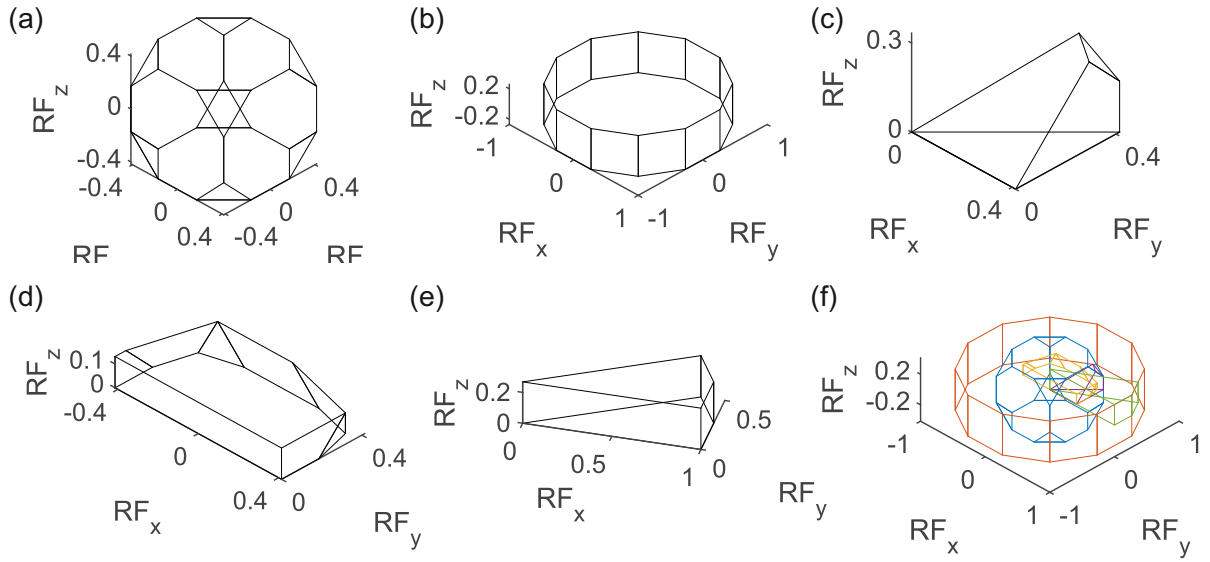


Figure 5.2: A selection of Rodrigues Frank fundamental zones of orientation and misorientation. (a) and (b) show orientation fundamental zones for O and D_6 symmetry, respectively. (c), (d) and (e) are misorientation fundamental zones between two crystals of O, O and D_6, and D_6 symmetry, respectively. (f) Shows a perspective view of all of the fundamental zones from (a) to (e).

Use of the rotation with the lowest angle of orientation or misorientation allows simple quantitative comparison between crystallites whether they rotate over time or whether they are on either side of a grain boundary.

5.3 Grain and grain boundary characterisation method

To characterise grains and grain boundaries, we start with real space coordinates of particles in a region of interest, and apply an analysis consisting of 4 steps: (1) the nearest neighbours of each particle are identified; (2) the orientation and structure of each nearest neighbour cluster is identified; (3) grains are identified and separated; (4) grain boundary locations and misorientations are found and visualised. The method is compatible with periodic boundary conditions, so may be directly applied to computational as well as experimental data.

5.3.1 Nearest neighbour identification

Correct identification of the nearest neighbour shell is essential for accurate structure and orientation assignment. For a given particle, the parent, we locate up to $N_{\max}$ nearest neighbours within a cut off distance using a k-d tree [165] to determine neighbour distances. For close

packed monodisperse spheres, $N_{\max} = 12$ due to geometrical constraints. The cut off distance is typically the first minimum in the radial distribution function of the particle coordinates. Each 'cluster' that is formed by a parent particle's nearest neighbours is referred to as the nearest neighbour cluster (NNC).

5.3.2 Registration, orientation, and structure assignment

To identify the orientation and structure of each NNC, we require a quantitative comparison of experimentally observed specimen NNCs and a set of reference NNCs from perfect crystal structures. To do this, each point in a specimen NNC must be paired with their corresponding point in a reference NNC by aligning the two point sets. This process is known as point set registration and is a common procedure in computer vision processes [166]. Methods for point set registration that involve only translation and orientation transformations are called rigid registrations. Here we will implement a rigid registration to dramatically simplify the process. This approach is valid because other small transformations have little effect on orientation measurements. In fact, the registration process can be further simplified by using the translational invariance property of crystal lattices. This is achieved by aligning the central point from the specimen NNC and the reference NNC. In doing so, the translation is removed from the registration calculation and the central parent points are registered. This simplification is valid for small displacements of the points from their lattice sites in the specimen NNC.

Point set registration is challenging because in order to align two point sets, the corresponding pairs of points must be known, but to find the corresponding pairs of points the sets must be aligned. Only by chance will the reference and specimen sets align, and if we wish to calculate the orientations for many different crystallites, it is almost guaranteed that there will be some specimen sets that do not align with the reference set. There are two options for registration: 1) trials over orientations and 2) trials over corresponding pair permutations. Iterative methods are unreliable for NNC set alignment because there are many local maxima in set alignment, where one point is aligned and others are not. Therefore, a registration scheme must span all possibilities to find the global maximum set alignment. Trials over orientations, considering option 1), requires a large number of trials for good angular resolution which makes the computation prohibitively costly. It is important to have as small a number of trials as possible, particularly for large sets of real space coordinates. For example, recent confocal microscopy studies have

regions of interest containing in excess of 10,000 particles (and therefore 10,000 NNCs). Thus, we propose a method using option 2): trials over corresponding pair permutations. We increase the efficiency by significantly reducing the number of permutation trials.

The method proceeds as follows. Let the reference NNC and the specimen NNC have N_r and N_s elements, respectively. Note that the central parent points are registered from the translation step so they are not included. Set alignment is quantified by the sum of the N_s smallest distances between the point sets of the specimen NNC and the reference NNC. Maximum set alignment is achieved for the minimum value of this sum. A brute force approach would require trailing all permutations of pairs of points between the specimen and reference sets, equal to $N_s!$. For a close packed crystal this is $12! \approx 4.8 \times 10^8$, which is prohibitively costly. However this number may be significantly reduced by taking advantage of the fact that for an orientation to be specified in D dimensions it is enough to select only D linearly independent vectors [159]. If the reference NNC and specimen NNC are related by a rigid transformation, as is the case for a *perfect* polycrystal where the reference and specimen NNC have the same structure, the sets can be aligned by considering only three corresponding pairs of points. Thus, in three dimensions, instead of $N_s!$ trials, the number is reduced to the permutations of three from N_r, ${}^{N_r}P_3$, lowering the number of trials by a factor of $(N_r - 3)!$. Therefore, corresponding pair trials are generated from the permutations of three points from the N_r reference NNC points paired with the same three randomly selected points from the specimen NNC. For a close packed crystal, $(N_r - 3)! = 9! \approx 10^5$, cutting the computational cost by 5 orders of magnitude. This number may be reduced further with consideration of the symmetry of the reference NNCs, as certain permutations of 3 particles from N_r are equivalent. For example, the number of trials required for face centered cubic (FCC), hexagonal close packed (HCP) and body centered cubic (BCC) NNCs reduces to 39, 223 and 17, respectively.

The point set registration is laid out in the following sequence and illustrated in the flow diagram in Fig.5.3a where Y and N represent yes and no, respectively.

1. Input trials of inequivalent permutations of three corresponding pairs.

2. Is the number of completed loops equal to the number of trials of corresponding pairs? If no go to 3, if yes go to 5.

3. Each trial of three corresponding pairs is converted to an orientation by the Kabsh Algo-

rithm [122, 167], which minimises the squared distance between the pairs of corresponding points. Note we modify the Kabsch Algorithm to fix the centre of rotation to the parent particle. Each orientation is applied to all points in the specimen set in an attempt at set alignment.

4. Calculate the sum of the N_s smallest distances between pairs of points, one from each NNC set. Return to 2.

5. The trial that produced an alignment with the minimum sum of the N_s smallest distances between pairs of points, one from each NNC set, establishes the corresponding pairs. Points are paired when the distance between them is one of the N_s smallest. The registration is formed by this set of pairs where every point in the specimen NNC has a corresponding point in the reference NNC.

6. Is any point paired with more than one other? If no go to 7, if yes go to 8. To enhance the accuracy of the method, registrations are only accepted if no point is paired with more than one other. This means that only specimen NNCs with a structure approximately equal to the reference are registered.

7. Output accepted registration.

8. Registration fails.

Although success in finding the global minimum in the sum of N_s smallest distances between the specimen and registered NNC points is only guaranteed for *perfect* polycrystals, this approach will still pair corresponding points in each set for specimen NNCs with small deviations from a perfect structure. The global minimum is found by using the accepted registration from step 7, where corresponding pairs for *all* points in the specimen NNC are used (instead of just three) as the input for the Kabsch Algorithm [122]. Again, we modify the Kabsch Algorithm so the rotation centre is fixed to the central parent particle, regardless of the centre of mass of the NNC. This allows robust orientation measurement for incomplete NNCs. The reported orientation for each NNC is calculated from this complete registration.

Structure assignment is performed by minimising the sum of the N_s smallest distances between corresponding pairs of points from the accepted registrations over reference NNC structures of interest. For example, a hard sphere system may have an FCC or HCP crystal structure,

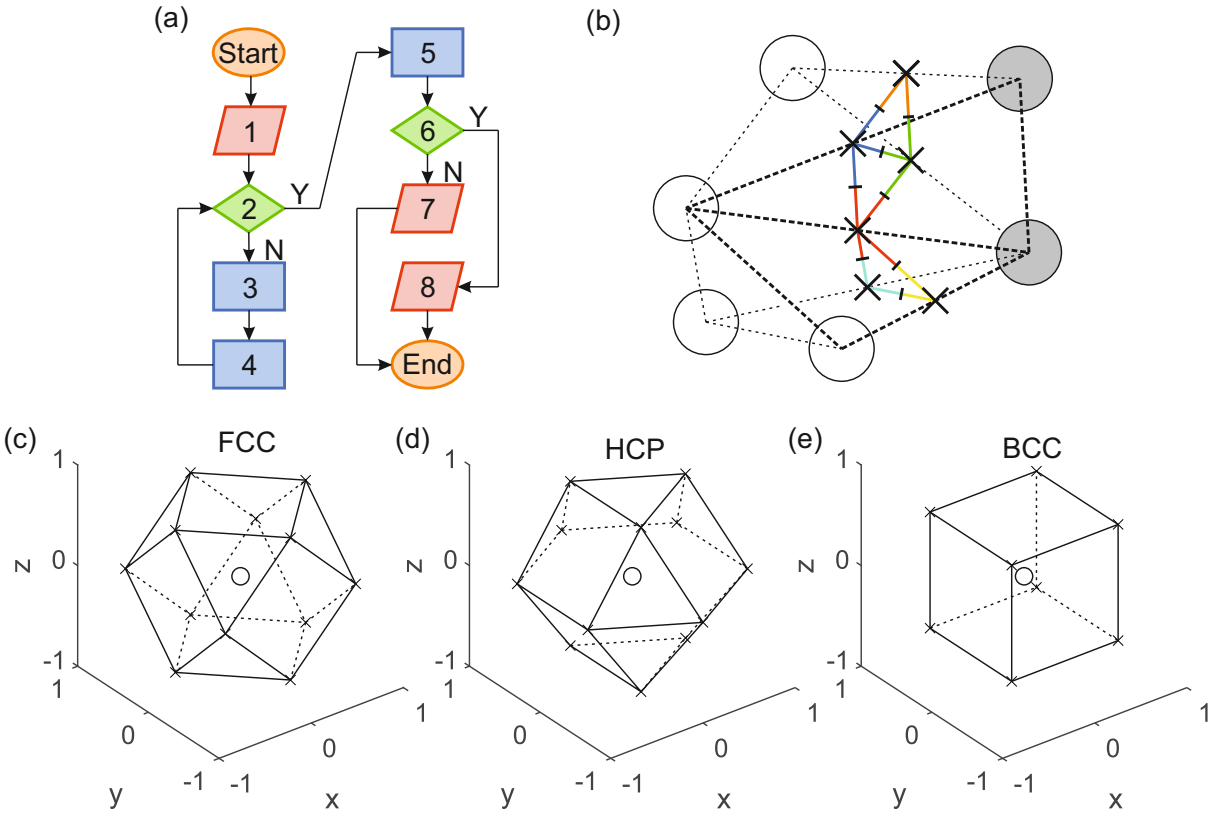


Figure 5.3: (a) Flow chart of the point set registration process. Ovals denote the start or end, parallelograms are inputs or outputs, diamonds represent decisions, where Y and N stand for yes and no, respectively, and rectangles indicate processes. The detail for each number is given in the text. (b) Cartoon showing the grain boundary rendering process. The positions of particles in two grains in three dimensions are shown by white and grey circles, respectively. They are not positioned in a crystalline arrangement for the purpose of clarity. Delaunay triangulation edges are shown as dotted lines (thickness for perspective) and grain boundary points are shown as black crosses. The grain boundary lines are shown in two colours, either side of a perpendicular bisector. (c), (d) and (e) show the NNCs for FCC, HCP and BCC, respectively. The black crosses mark the positions of particles and the black circle, the parent particle.

whereas a BCC crystal structure is expected for spheres with long range repulsion. Therefore, one may wish to assign the set of references to contain three reference NNCs, one each for FCC, HCP and BCC where N_r = 12, 12, or 8, respectively. The reference NNCs for FCC, HCP and BCC are shown in Fig.5.3 c, d and e, respectively. The procedures in this section can be parallelised over each specimen NNC individually for efficient computation.

5.3.3 Separation of grains

After the orientation of all NNCs have been measured, these may be used to separate different grains. Firstly, a Delaunay triangulation between all parent particles with NNCs assigned the same structure forms a graph where each particle is a node and each pair of connected particles is a link. Since each link connects two different particles each with their own NNC orientation, a misorientation may be found. Like an orientation, a misorientation may be expressed as a rotation θ about an axis. Two thresholds are then applied to eliminate links, and separate grains. The first is a distance cut off R_{cut} for NNCs with the same orientation but separated in space. The second is θ_{cut}, a maximum misorientation angle for adjacent NNCs in the same grain. This leaves disparate 'clusters' of links between particles; each of these clusters form a single grain. A high θ_{cut} runs the risk of including particles that have intermediate orientation and position between grains, thus, preventing grain separation. A low θ_{cut} may fragment grains to produce low angle grain boundaries within them. Particles with no neighbours within these thresholds are not assigned to a grain, they are not considered as a grain themselves. As a result, the smallest grain possible consists of two particles. This step also serves to confirm or reject the structure assigned in section 5.3.2, and suppresses the spurious identification of orientation and structure. Any particles not belonging to a grain are considered to have a structure different to the reference NNCs considered, which may include particles with a liquid-like local environment.

5.3.4 Grain boundary location, misorientation and visualisation

Boundaries between grains may be resolved using a method similar to that used by Lavergne et al. [56], but extended to three dimensions. Firstly, a Delaunay triangulation over particles belonging to a grain is calculated. The midpoints of Delaunay edges which connect particles in different grains form a surface of grain boundary points. Fig.5.3b shows a schematic of a

triangulation of particles in two grains where the members of each grain are shown as white or grey circles, respectively. The dotted lines show the triangulation edges and the black crosses show the grain boundary points. Note that these points do not lie on a particle coordinate. Furthermore, a 'local' misorientation may be calculated for each grain boundary point using the orientation of the particles on either end of the triangulation edge, yielding a spatial map of misorientations over the boundary surface. Grain boundary particles may be identified as those within a cut off distance to the grain boundary surface and not a member of a grain. In this way, grain boundary particles may be identified without searching for a particular arrangement of particles at the boundary.

The geometry of the surface may be visualised in more detail by again considering the Delaunay traingulation. For every tetrahedron with vertices in two grains, the grain boundary points formed from its edges may be linked by lines to form edge-sharing triangles, as shown in Fig.5.3b. It is convenient to render the local misorientation by colouring the lines instead of the grain boundary points. This is done by bisecting each line and colouring each half by the misorientation of the closest grain boundary point. This can be seen in Fig.5.3b where each line has two colours, one either side of the bisecting line. In this way grain boundaries are rendered as a triangle mesh where local misorientation information is represented by colour. In this work we choose to map the colour to the misorientation angle from an angle axis representation.

5.4 Results and discussion

To demonstrate the utility and capabilities of this method, we study two colloidal crystals, a templated bicrystal using a patterned surface, and a homogeneously nucleated polycrystal. We characterise misorientations of grain boundaries with particle level detail; one should note that single-particle resolution is often presented as a key strength of colloidal model system, and our method broadens this strength to grain boundary studies.

5.4.1 Grain boundary structure in a templated colloidal bicrystal

Here, we re-purpose particle coordinates from a colloidal bicrystal produced to study grooves at grain-boundary–liquid triple junctions [57]. We use this data as a test case to demonstrate the method on a grain boundary of known location and misorientation. The sample was produced

by slowly sedimenting a colloidal dispersion of monodisperse, 1.6μm diameter silica spheres onto a glass slide [57]. The glass slide was pre-templated using stereolithography, drilling dimples in positions corresponding to the first plane of a Σ17 (a type of coincident site lattice) grain boundary between two compact planes. During slow sedimentation, the first layer of deposited particles sits in the dimples; subsequent layers grow by epitaxy by completing compact planes. The aqueous dispersion is index matched to allow deep penetration of the light without scattering; it also contains fluorescein so that the matrix can be easily distinguished from the non fluorescent glass spherical particles. The sediment is imaged using 3D laser scanning confocal microscopy. Appropriate post processing finally allows us to determine the center of mass of each colloidal particle [57]. The cut off distance for nearest neighbours is set to 2.0μm, the first minimum of the radial distribution function. The distribution for the number of nearest neighbours is found in appendix 5.6.1. All NNCs with at least 3 neighbours of the parent particle were considered for orientation measurement, comparing against both FCC and HCP reference NNCs, which were scaled such that the average nearest neighbour separation was 1.633μm, the same as the first peak in the radial distribution function. The misorientation angle cut off was set empirically to be $\theta_{\text{cut}} = 2°$, which is small enough to separate the grains in this data set. Appendix 5.6.2 provides a discussion on the effects of different values of θ_{cut}. The distance cut off for grain boundaries was set to be the same as for nearest neighbour detection i.e. $R_{\text{cut}} = 2.0\mu\text{m}$. The total computation time for the grains and grain boundaries in the following discussion from 38977 particle coordinates was 172 s using a quadcore Intel Core i-6500 with 16 GB of RAM. The rendering was performed using open source PyMol software [168].

Fig.5.4a shows a reconstruction of the coordinates of all particles. A boundary may be roughly identified by eye. Applying our method, the two largest FCC grains detected are shown in Fig.5.4b, coloured by grain, sitting on either side of the nominal Σ17 boundary. Initially, we consider only these two major grains, and identify a grain boundary between them. The misorientation is found to be $\vec{RF}_{\text{M}} = (0.2497, 0.0088, 0.0002)$; in agreement with the value for a Σ17 boundary in an FCC crystal, $\vec{RF}_{\Sigma 17} = (0.25, 0, 0)$ [169]. Note that this average misorientation is calculated from the average orientation of each large FCC grain using an implementation [170] of the rotational averaging method described in ref. [171]. If we graphically render the boundary and colour code misorientations over the edges (see section 5.3.4) making up the surface as shown in Fig.5.4c, a broad spatial variation in misorientation is revealed. This is accordingly seen in the Rodrigues-Frank misorientation fundamental zone in Fig.5.4d, where

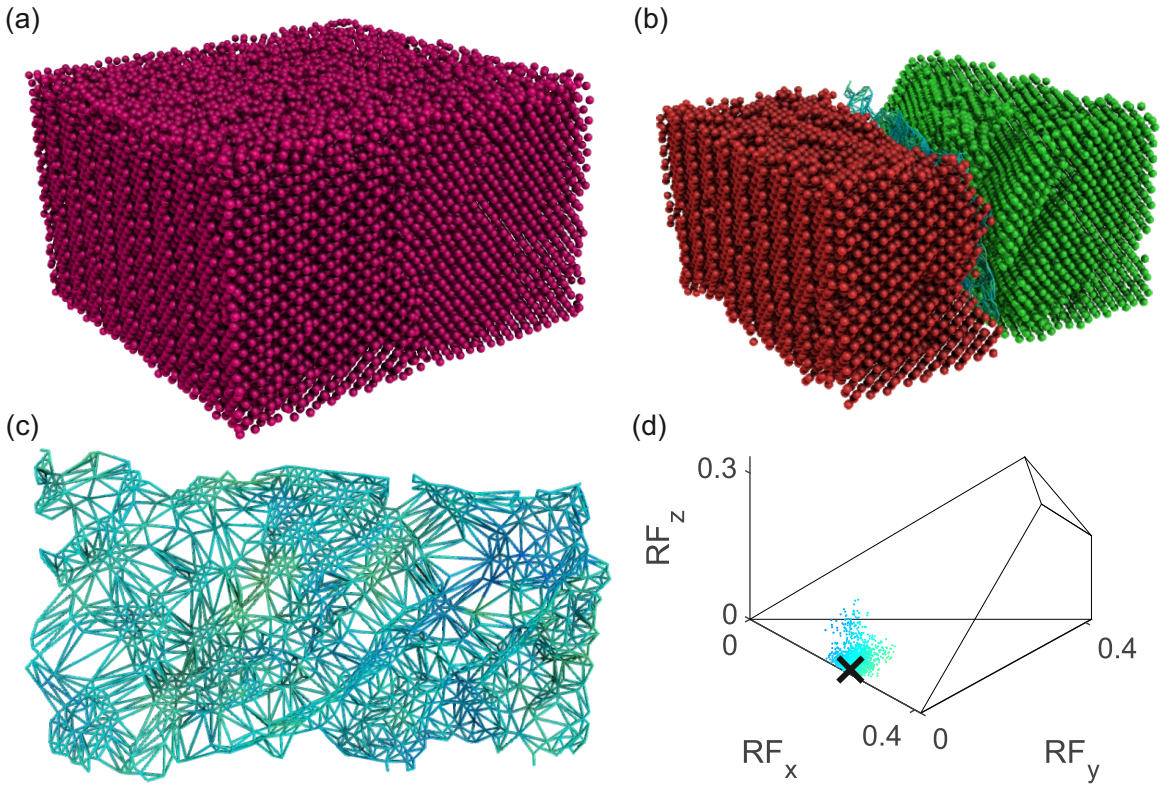


Figure 5.4: Templated colloidal bicrystal. (a) Rendering of the colloidal crystal from particle coordinates. (b) Two largest FCC grains, either side of the Σ17 boundary. (c) Normal projection of the Σ17 boundary. (d) Rodrigues-Frank fundamental zone of misorientation containing the local misorientation for the boundary. The black cross shows the mean misorientation $\vec{RF}_{\mathrm{M}} = (0.2497, 0.0088, 0.0002)$.

points are scattered around the misorientation expected for a Σ17 boundary, shown as a black cross. Thus, we show the method characterises grain boundaries correctly and resolves spatial variation in misorientation at the particle level. Details of the grain boundary particles within R_{cut} of the Σ17 boundary may be found in appendix 5.6.3, however, the following grain boundary discussions will focus on the grain boundary surfaces, rather than the particles themselves.

Templating techniques such as those used to create this bicrystal [57] are designed to create a single boundary with a pre-engineered misorientation. However, the two major grains and the boundary between them do not account for all the grain and grain boundary structures present: this manufactured boundary is far more complex than a single surface with a single misorientation. Using our method we proceed to identify all FCC and HCP grains composed of 50 or more particles and characterise the multitude of unique boundaries which are present.

We firstly consider the range of FCC-FCC boundaries present in the system, in particular the twin boundaries. Twinning is of interest as particular twin geometries have consequences for grain growth kinetics [132]. To this end, HCP grains are omitted during the FCC-FCC grain boundary generation (as explained in section 5.3.4) so that triangulation edges connect FCC grains on either side of a stacking fault. This prevents FCC twin boundaries being replaced by two grain boundaries between the two twinned FCC grains and the bisecting HCP layer. A particularly salient example of a twin boundary is shown in Fig.5.5a, where a smaller FCC grain, labelled G_t is surrounded by one of the major FCC grains. It is wrapped in an envelope-like grain boundary, whose misorientation is located around $\vec{RF} = (\frac{1}{3}, \frac{1}{3}, \frac{1}{3})$ in the FCC-FCC Rodrigues-Frank misorientation fundamental zone (see inset in Fig.5.5a). These values are close to those expected for a twin boundary in an FCC crystal. This boundary is composed of two different inclinations, one where the boundary plane has a normal perpendicular to the hexagonal plane direction, marked i in Fig.5.5a, and another where the normal is contained in the hexagonal plane, marked as ii. Here we see how the spatial resolution of our method reveals the fine details of grain boundaries. If we add the HCP stacking, we indeed find that the parts of the boundary parallel to the hexagonal planes, i, are coincident with single, isolated HCP layers. However, this is not case for the parts of the boundary that wrap around the small twin grain to connect these planes, ii. In principle, one might also identify isolated FCC-HCP boundaries, as we will see below, but the ability to freely calculate the misorientation angle between grains of selected structure makes the detection of twin grain boundaries much simpler.

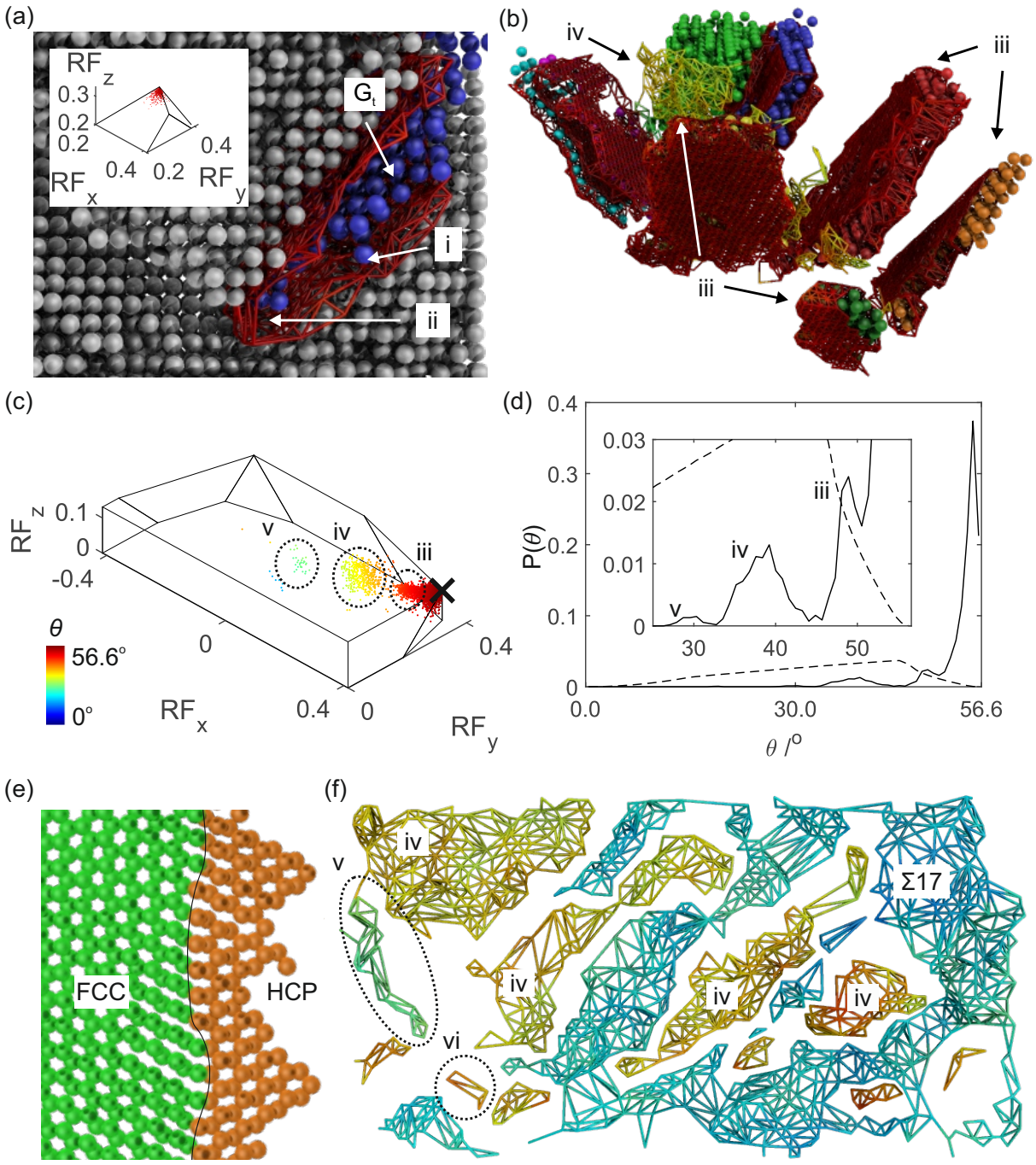


Figure 5.5: A selection of other grain and grain boundary structures within the templated colloidal bicrystal, the numbered labels, i through v, included in several panels are explained in the main text. (a) FCC twin boundary and twin grain G_t. The inset shows the local misorientation distribution. (b) HCP grains and FCC-HCP grain boundaries. The particles are coloured by grain identity and the grain boundaries by local misorientation angle, θ (see colour bar in panel(c)). (c) Rodrigues-Frank misorientation distribution within the fundamental zone for boundaries between FCC and HCP grains, coloured by misorientation angle (see colour bar). (d) Local misorientation angle distribution for FCC-HCP boundaries. The inset shows a magnified portion. (e) In-plane stacking sequence change from FCC to HCP. The black line is a visual guide. (f) A mosaic of grain boundary structures including the Σ17 boundary and the contributions of other boundaries.

We proceed to consider the HCP crystalline regions and FCC-HCP boundaries. As shown in Fig.5.5b, the nominally 'simple' Σ17 boundary has a significant number of HCP layers extending into the FCC grains. The corresponding misorientations are plotted in the Rodrigues-Frank fundamental zone in Fig.5.5c with a colour depending on the misorientation angle, θ. Projecting the distribution of points in misorientation space onto a probability distribution in misorientation angle, $P(\theta)$, (see Fig.5.5d), we see that there are multiple peaks. The distribution is magnified in the inset so that the peaks with smaller probabilities may be seen more clearly. The largest peak at misorientation angle $\theta \approx 56.6^\circ$ corresponds to Blackburn [172] boundaries between HCP and FCC grains either side of a stacking fault. The energy associated with stacking fault creation is very low so it is no surprise to see the highest probability at this position. Fig.5.5c shows the local misorientation distribution of these boundaries, scattered about the Blackburn position marked with an black cross at position $\vec{RF}_{\mathrm{B}} = (0.414, 0.318, 0.132)$.

Note the presence of a smaller peak at $\theta \approx 49^\circ$, marked iii in Fig.5.5d. In fact, these correspond to the portion of the boundaries running approximately perpendicular to the hexagonal planes, which wrap around the HCP grains to connect two in-plane FCC-HCP boundaries. They are marked iii in Fig.5.5b, where they appear a lighter shade of red. Their location in the Rodrigues-Frank misorientation fundamental zone is also marked iii in Fig.5.5c. Fig.5.5e shows how particle positions vary across this FCC-HCP boundary, where the boundary adopts this lower misorientation angle. There is no abrupt change from HCP to FCC; instead, the hexagonal planes gradually shift relative to one another. This results in NNCs in the vicinity of the boundary being distorted. Here, NNC particles move in a concerted manner with their counterparts from the same hexagonal plane, but differently from members in other hexagonal planes. This results in a net rotation of the NNCs near the boundary. Note that the Blackburn boundaries have the maximum misorientation possible i.e. the full misorientation between the two structures. Thus, the misorientation angle is necessarily reduced for the distorted NNCs. This kind of boundary has been identified before in colloidal crystals by Hilhorst et al. [55], though without a specific detection scheme.

Having located both FCC-FCC and FCC-HCP boundaries over all grains in the system, we are now in a position to characterise the Σ17 boundary in more depth. The 'single' boundary identified in Fig.5.4c using the two major FCC grains now looks very different (see Fig.5.5f). The blue portion marked as Σ17 corresponds to FCC-FCC boundaries, nominally the 'remnants'

of the original Σ17 boundary. However, there are now other contributions including FCC-HCP boundaries with different misorientation where the HCP grains meet FCC grains at the boundary. These are marked iv and shown in yellow; they also appear as surfaces in Fig.5.5b and in the misorientation distribution Fig.5.5c. The misorientation angles of these boundaries peak at $\theta \approx 39°$, marked iv in the misorientation angle distribution in Fig.5.5d.

Another contribution to the boundary in Fig.5.5f is the FCC-HCP boundary between the twin grain G_t from Fig.5.5a and HCP layers on the other side of the Σ17 plane. This is shown in green on the left hand side and marked v. This is also visible at peak v at $\theta \approx 30°$ in Fig.5.5d. Finally, there is a contribution from the junction between G_t and the major FCC grain on the other side of the Σ17 plane, marked vi.

With our method we have characterised the grain and grain boundary structure of a pre-templated Σ17 boundary [57] in great detail. Despite the misorientation between the major grains conforming to the intended structure, the microstructure of the boundary itself is far more complex, with a combination of defects and highly curved grain boundaries with misorientations that do not exactly conform to the angles predicted for simple stacking faults. Furthermore, the difference in structure of the boundary can contribute to a difference in the properties, which may go unexamined without particle level structural characterisation.

5.4.2 Characterisation of homogeneously nucleated polycrystalline structures

We extend the analysis to a sample where we have no pre-knowledge of the position or misorientation of the grain boundaries. We demonstrate this by analysing a homogeneously nucleated colloidal polycrystal. The finer grain structure showcases the spatial resolution of our method for grain and grain boundary detection. We apply the algorithm to coordinates of particles in a polycrystalline colloidal sample composed of $\approx 2\mu m$, $p = 0.03$ polydisperse, polydimethylsiloxane stabilized PMMA spheres. The synthesis of the particles is based on the methods presented in references [173, 174]. The particles are suspended in a density and index matching mixture of cyclohexyl bromide and cis-decahydronaphthalene saturated with tetrabutylammonium bromide (TBAB) to achieve electrostatic screening. The particles are dyed with trace amounts of cumarin for fluorecent imaging using a confocal scan head on a Leica SP5 microscope. The particle coordinates are recovered from the confocal images using conventional particle identification software [80].

To prevent heterogeneous nucleation, the glass walls of the sample cell were coated with a polydisperse colloidal PMMA to create a uniform but rough surface on the length scale of the colloidal particle. To this end, a 22×22 mm number 1 cover slip was spin coated with a cis-decalin solution of volume fraction $\phi \approx 0.2$, polydispersity $p = 0.3$ PMMA particles, taking care to avoid bulges on the outer rim of the cover slip. This is immediately transferred to a 120° hot plate to dry the solution rapidly to avoid de-wetting. This cover slip forms the imaging wall of a glass sample cell. A small glass bottle with the bottom removed is attached to the cell to allow the placement of the colloidal dispersion via pipette. The cell is sealed by attaching screw top lid with a teflon liner to the bottle top. The colloidal sample is left for several hours to crystallise, after which a field of view far away from the flat walls of the container is investigated.

As in the case of the templated bicrystal, the nearest neighbour and grain boundary cut off distances are set to equal the first minimum of the radial distribution function, in this instance, $R_{\text{cut}} = 3.0$ μm, and the reference NNCs are scaled to have a nearest neighbour distance equal to the first peak of the radial distribution function (2.35 μm). The distribution of numbers of nearest neighbours for the particles is found in appendix 5.6.1. The misorientation angle cut off is set to $\theta_{\text{cut}} = 2°$. However, this time we do not impose a cut off for the size of grains; thus, the smallest grains can now consist of as few as two NNCs. The total computation time was 234 s for 44025 particle coordinates on the same quadcore Intel Core i-6500 with 16 GB of RAM.

Fig.5.6a and Fig.5.6b show the FCC and HCP grains, respectively, where each grain is assigned a unique colour. Some colours may appear indistinguishable because there are many colours for the many grains: 866 FCC grains and 964 HCP grains. The grain sizes range from 2 to approximately 500 particles. The number of particles in FCC and HCP grains are 8606 and 5368, respectively, showing that, in general, HCP grains are smaller than FCC grains. A striking feature of both Fig.5.6a and Fig.5.6b are the planar gaps, and flat, narrow grains. These are formed by stacking sequence changes, where FCC changes to HCP or vice versa and serve to break up the crystallites parallel to the hexagonal layers. We may subsequently identify FCC-FCC, FCC-HCP and HCP-HCP boundaries. Each row of Fig.5.6 from 5.6c and beyond contains three panels that present from left to right the location of grain boundaries, the misorientation within the fundamental zone and a misorientation angle distribution, respectively. As before, grain boundaries and their distributions are coloured by their misorientation angle, θ, and the colours are consistent for each row. The colour maps are shown attached to the location plots

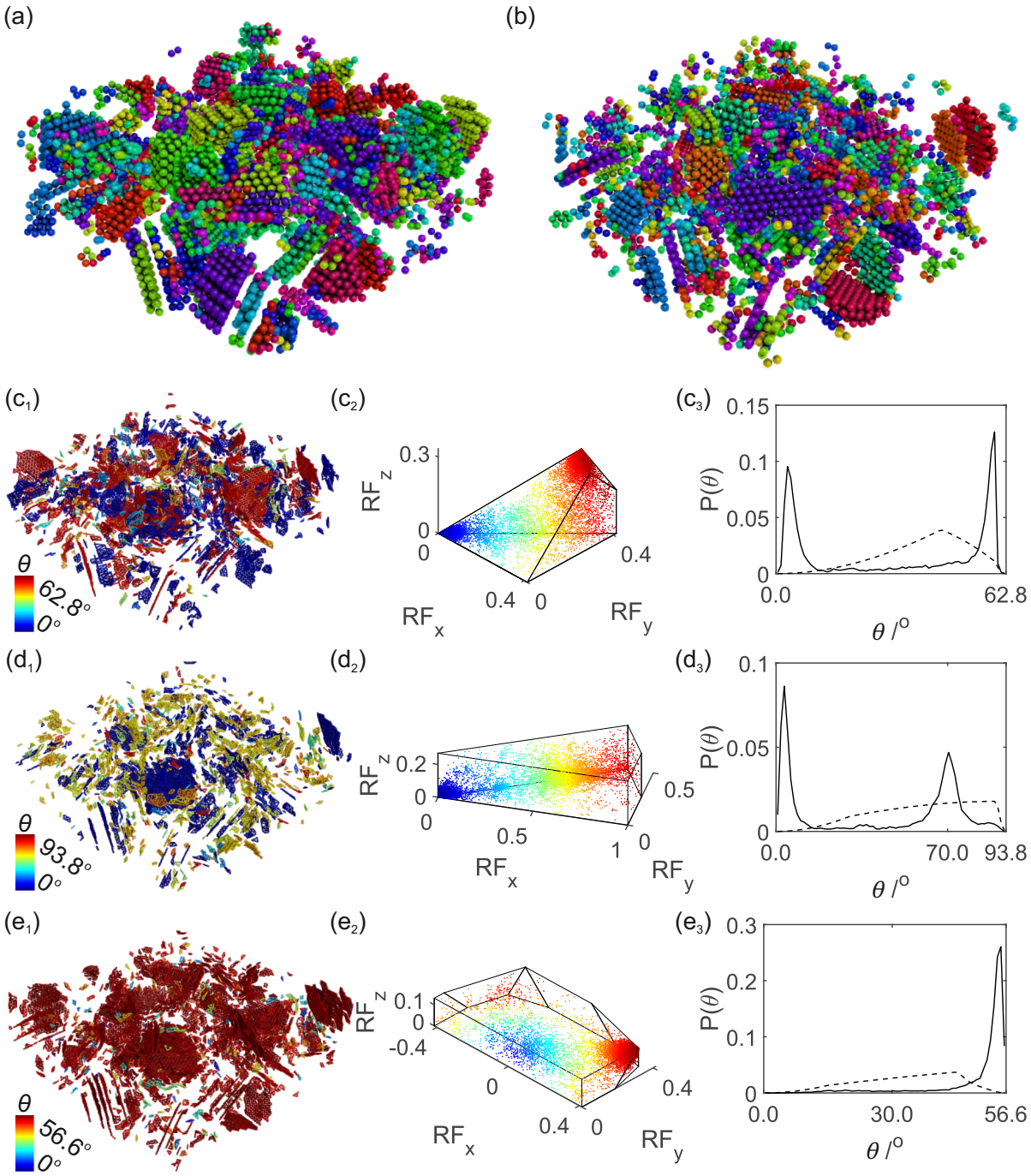


Figure 5.6: The grain and grain boundary structures within the colloidal polycrystal. (a) and (b) show FCC grains and HCP grains, respectively, each grain is given a unique colour. The remaining panels of the image are organised as follows. Rows (c), (d) and (e) show characterisation for grain boundaries between FCC grains ommiting HCP grains, between HCP grains omitting FCC grains, and between FCC and HCP grains, respectively. Column (1) shows the spatial distribution of grain boundaries. Column (2) shows the misorientation distribution in the Rodrigues-Frank fundamental zone. Column (3) contains probability distributions of misorientation angles. The dotted lines show distributions for randomly oriented grains. The colour bar extends from the smallest rotation angle to the largest and governs the colours for the panels in the same row.

span angles between 0° and the maximum misorientation angle.

Again, we start by looking at FCC-FCC boundaries, omitting the HCP grains (see Fig.5.6 row (c)). The boundary structure is dominated by low angle and twin grain boundaries, in approximately equal measure. They occur where an even or odd number of HCP stacked hexagonal layers, respectively separate two FCC grains. Accordingly, these boundaries are flat and lie parallel to the local hexagonal plane direction as seen in Fig.5.6c$_1$. The corresponding misorientation distribution is shown in Fig.5.6c$_2$ where the misorientations at low angle and twin boundaries are concentrated around the points $\vec{RF}_0 = (0, 0, 0)$ and $\vec{RF}_T = \left(\frac{1}{3}, \frac{1}{3}, \frac{1}{3}\right)$, respectively in the Rodrigues-Frank fundamental zone. Accordingly, these boundaries appear as peaks in the misorientation angle distribution in Fig.5.6c$_3$ at $\theta \approx 0°$ and $\theta \approx 60°$. The twin peak at $\theta \approx 60°$ and the peak at $\theta \approx 0°$ have approximately equal probabilities relative to the random misorientation distribution, showing that stacking faults in the FCC crystal contain an equal proportion of even and odd hexagonally close packed layers. Note that all these twin boundaries are planes, unlike the example shown in the templated bicrystal where an FCC-FCC boundary bends around to encapsulate an FCC crystallite as in Fig.5.5a. None of the grains in this sample are large enough to support the in-plane stacking fault required to generate such a boundary. Fig.5.6c$_2$ and 5.6c$_3$ show that there are also a significant proportion of misorientations located between the peaks at $\theta \approx 60°$ and $\theta \approx 0°$. These misorientations are a hallmark of a polycrystalline sample, displaying many differently oriented grains. The surface area of these boundaries is far smaller than the twin and low angle boundaries so they appear with lower probabilities.

We may also look at HCP-HCP boundaries by omitting the FCC grains (see Fig.5.6 row (d)). Again, the structure is dominated by boundaries arising from stacking sequence changes of hexagonal planes. The most probable peak appears at $\theta \approx 0°$ in Fig.5.6d$_3$ and the corresponding boundaries are shown in blue in Fig.5.6d$_1$ and 5.6d$_2$. These boundaries are created where one or more FCC layers intersect two HCP grains, exposing a gap between two HCP grains of the same orientation. The other dominating feature of the distribution in 5.6d$_3$ is at $\theta \approx 70°$. This is again a consequence of stacking sequence changes, only this time along different hexagonal plane normal directions. Specifically, they are the different hexagonal plane normal directions in the FCC structure. The angle between these planes is equal to 70.53° and accordingly, boundaries with misorientation $\theta \approx 70°$ appear with a significant probability.

Finally, considering FCC-HCP boundaries (see Fig.5.6 row (e)), we see a grain boundary

structure dominated by the Blackburn misorientation relationship, corresponding to very high stacking disorder. Again, this is evidence for the random close packing structure of the polycrystal. Fig.5.6e$_1$ shows mostly planar boundaries coloured in red corresponding to a Blackburn misorientation of $\vec{RF}_{\mathrm{B}} = (0.414, 0.318, 0.132)$ as shown in Fig.5.6e$_2$. The distribution has a proportionately large peak at $\theta \approx 56°$ in Fig.5.6e$_3$. However, there is now no small peak at $\theta \approx 49°$, due to the absence of in-plane stacking faults. These grains are smaller than in the bicrystal discussed in section 5.4.1. Much like the absence of any curved FCC-FCC twin boundaries in the polycrystalline sample there is also an absence of curved FCC-HCP boundaries. In the templated bicrystal of section 5.4.1, the stacking changes over roughly six particle spacings as shown in Fig.5.5f, similar in length scale to the in-plane stacking faults of Hilhorst et al. [55]; this is too large a length scale for the finer grains of the polycrystal. Hence, no boundaries due to in-plane stacking faults are seen in either FCC-HCP boundaries or indeed FCC-FCC boundaries as presented earlier.

5.5 Conclusion

A complete method is presented to convert real space particle coordinates of polycrystalline materials to the location and character of grains and grain boundaries. Heterogeneity in misorientations may be characterised with single-particle resolution over boundaries without a priori knowledge of local crystal structure, giving unprecedented insight into a wide range of faults and defects, and how the degree of misorientation might affect physical properties. Here, we apply this to colloidal crystals, finding an unexpected degree of structural complexity in a nominally 'tame' [133] templated system and how the distribution of misorientations change when similar particles are instead allowed to homogeneously nucleate crystals and grow. Importantly, we identify features such as twin boundaries, the Blackburn orientation relationship and low angle grain boundaries without targeting different portions of the structure. Our method may be applied to both experimental and numerical data with minimal knowledge of crystal orientations in a region of interest and would serve as a useful tool in future studies of polycrystals, nucleation and grain growth.

5.6 Appendix

5.6.1 Nearest neighbour cluster size distributions

Following the description of nearest neighbours in section 5.3.1, we calculate the number of neighbours for each particle. Histograms for the templated bicrystal from section 5.4.1 and for the polycrystal from section 5.4.2 are shown in Fig.5.7a and b, respectively. In both cases, the majority of particles have nearest 12 nearest neighbours, with a steep decay in the number of particles with fewer than 12 nearest neighbours. This is indicative of a mixture of close packed crystal and particles with liquid like order.

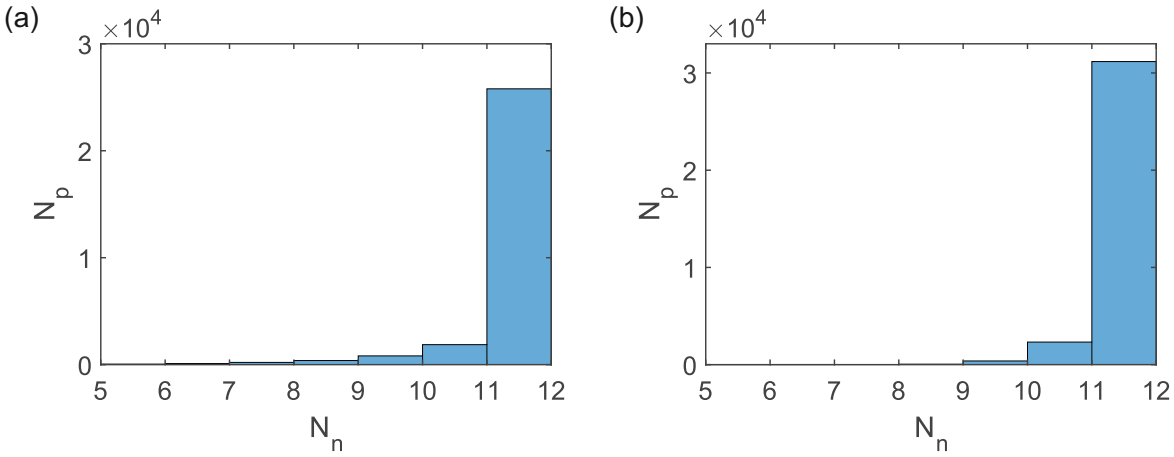


Figure 5.7: Histograms of number of nearest neighbours of particles in (a) the templated bicrystal and (b) the polycrystal. N_p and N_n are number of particles and number of nearest neighbours, respectively.

5.6.2 Angle cut off

We perform the grain boundary surface calculations with a greater value of misorientation angle cut off θ_cut to demonstrate its effect. We use two larger values of $\theta_\mathrm{cut} = 3.5°$ and $\theta_\mathrm{cut} = 5.0°$. The grain boundary surfaces for three θ_cut values, $\theta_\mathrm{cut} = 2°, 3.5°$ and $5.0°$ lie approximately on top of one another, as shown in Fig.5.8a. Note that the persepctive of the 3D plot is the same as in Fig.5.4b. This shows that changing θ_cut has little effect on the grain boundary location.

Next, we measure the misorientation for each grain boundary point and plot the distributions in the Rodrigues-Frank fundamental zone. The distributions for $\theta_\mathrm{cut} = 2.0°$, $\theta_\mathrm{cut} = 3.5°$ and $\theta_\mathrm{cut} = 5.0°$, are shown in Fig.5.8a, b and c, respectively. The spread of points about

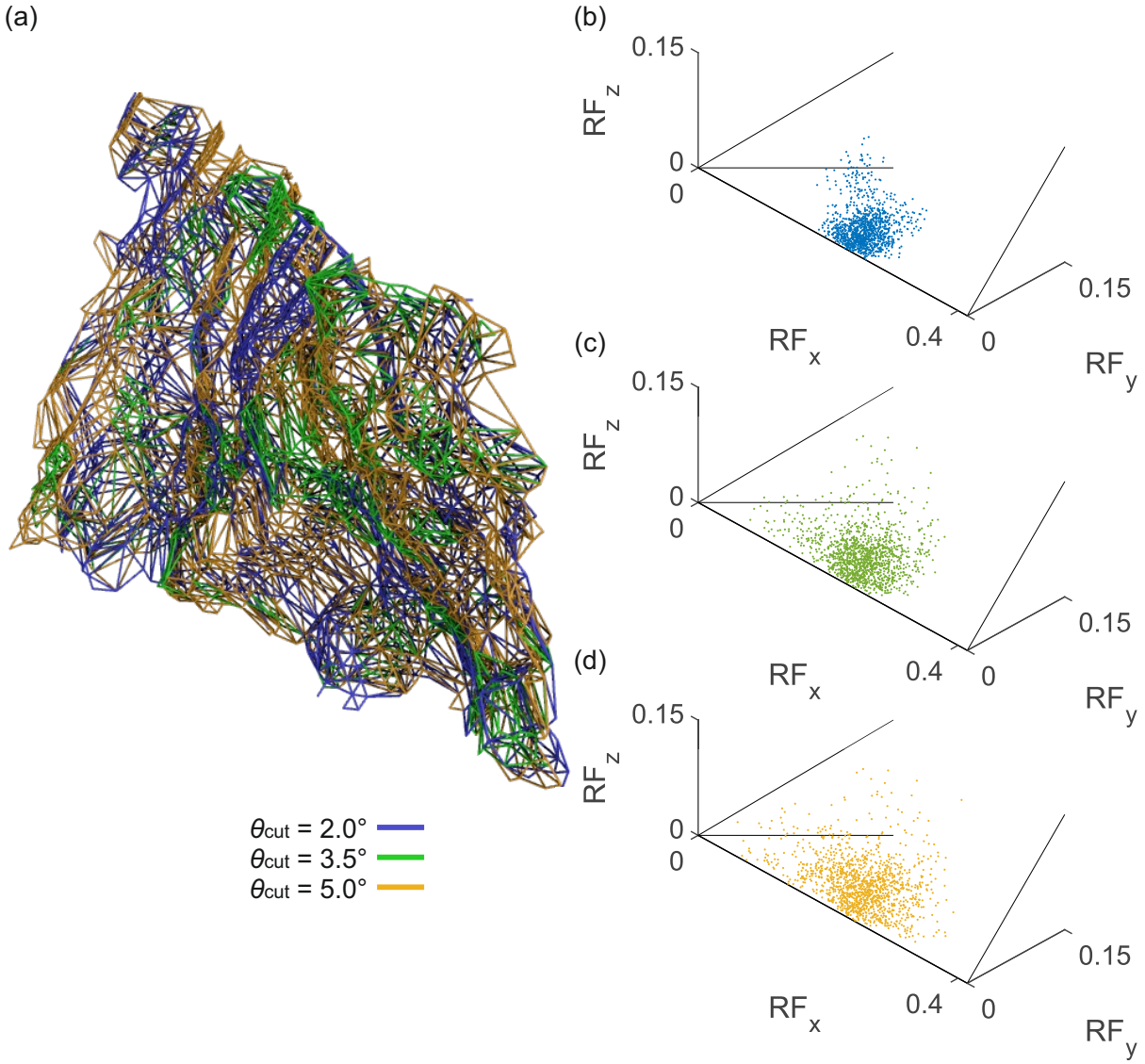


Figure 5.8: (a) Σ17 grain boundary surfaces for several θ_{cut} values. (b) and (c) and (d) show the local misorientation distributions within a section of the Rodrigures-Frank fundamental zone for $\theta_{\text{cut}} = 2.0°$, for $\theta_{\text{cut}} = 3.5°$ and for $5.0°$ respectively.

$\vec{RF}_{\Sigma 17}$ increases with θ_{cut}, however, the mean orientation between the two large grains, either side of the Σ17 boundary is not significantly affected. Their mean values are equal to $\vec{RF}_{\text{M}} = (0.2489, 0.0091, 0.0007)$ and $\vec{RF}_{\text{M}} = (0.2487, 0.0091, 0.0007)$ for $\theta_{\text{cut}} = 3.5°$ and $\theta_{\text{cut}} = 5.0°$, respectively, which are both very close to $\vec{RF}_{\Sigma 17}$. This shows that the grain boundary identity may still be evaluated with a variety of θ_{cut} values.

However, if the misorientation cut off is set too low, grains begin to be split apart with low angle grain boundaries within. We found that $\theta_{\text{cut}} = 2°$ provided a good compromise between keeping grains intact and measuring grain boundary misorientations with clearly defined and separated regions within the fundamental zones across both data sets.

5.6.3 Grain boundary particles

Grain boundary particles are identified as those that lie within a user defined distance cut off of the grain boundary surface. We apply a R_{cut} as the distance cut off equal to 2.0 μm to find the grain boundary particles for the Σ17 boundary as an example. These particles are shown in Fig.5.9a and b as a side on perspective, the same as in Fig.5.4b and at a normal perspective, the same as in Fig.5.4c respectively.

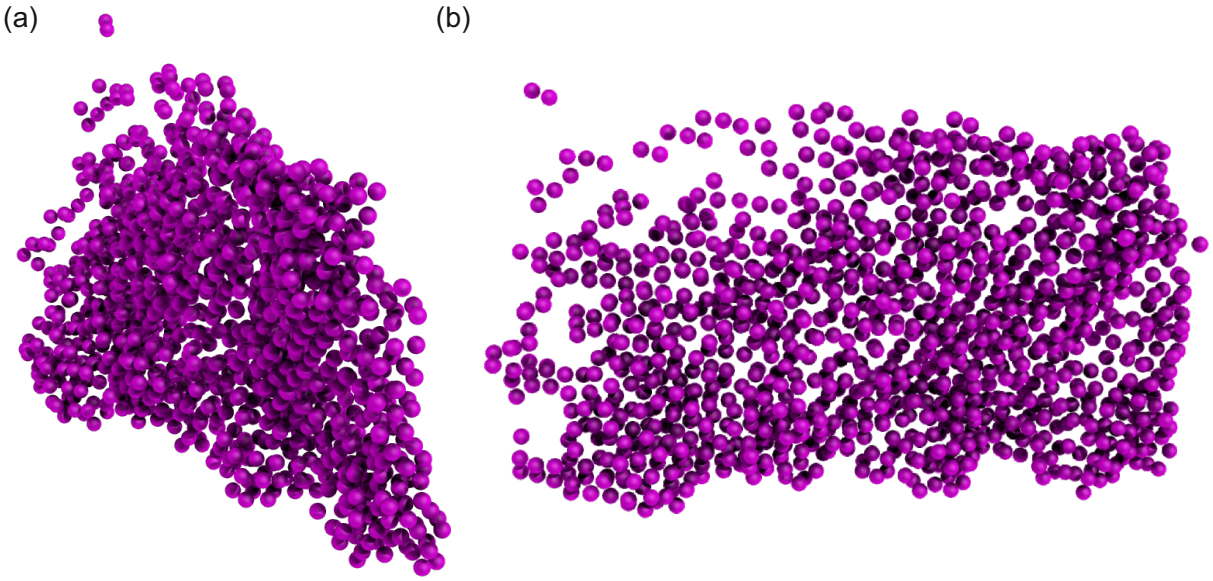


Figure 5.9: Σ17 grain boundary particles, (a) and (b) show a side on and a normal perspective.

Acknowledgements

The experimental bicrystal data set was taken by E. Maire and the polycrystal data set, by T. Yanagishima. I wish to acknowledge F. A. Lavergne, A. E. Stones and H. Tanaka for insightful discussions.

Chapter 6

Misorientation during homogeneous nucleation of a colloidal crystal

Abstract

The homogeneous crystal nucleation of a colloidal dispersion was studied to reveal the structure and misorientation within nuclei during nucleation and crystal growth. We find that close packed nuclei grow with a random hexagonal close packed structure displaying stacking faults and low angle misorientations exclusively. By examining the spatial variation of misorientations within nuclei we find that nuclei transition from a structure containing high misorientation angles, to one with high misorientation angles at the surface but lower angles at the core. Thus, we demonstrate that the crystal structure that forms at early times of nucleation is less ordered and is, therefore, not the same as the crystal structure at late times.

6.1 Introduction

Crystal nucleation is the process of forming an ordered crystal phase from a disordered fluid phase and has far-reaching consequences from pharmaceutical drug production to condensed matter and materials science [175]. Despite several decades of investigation [176], a comprehensive understanding of nucleation phenomena remains elusive. A simple and general interpretation for nucleation is expressed by classical nucleation theory, CNT. In CNT, the free energy to form a spherical crystal nucleus of radius, r, within the bulk of the fluid is [58, 177]:

$$\Delta G = -\frac{4\pi r^3 \rho \Delta\mu}{3} + 4\pi r^2 \gamma, \tag{6.1}$$

where ρ is the number density of the solid, γ, is the surface tension and $\Delta\mu$ (> 0) is the chemical potential difference between the fluid and solid. A nucleus only survives if the gain in free energy from forming the more thermodynamically stable crystal phase overcomes the loss in free energy associated with the creation of the solid-liquid interface [58]. These quantities are given by the first and second term in equation 6.1, respectively. As r increases, the nucleus grows and ΔG initially increases to reach a maximum at the critical nucleus size, $r = \frac{2\gamma}{\rho\Delta\mu}$, from which, ΔG subsequently decreases. Thus, nucleation depends on the barrier to forming a critical nucleus, ΔG_{crit} and the rate is expressed by [58]:

$$\begin{aligned} I &= \kappa \exp(-\Delta G_{\text{crit}}/k_{\text{B}}T) \quad \text{where,} \\ \Delta G_{\text{crit}} &= \frac{16\pi\gamma^3}{3(\rho\Delta\mu)^2}, \end{aligned} \tag{6.2}$$

where κ is the kinetic prefactor. The predictive ability of CNT rests on the accuracy of γ, $\Delta\mu$, ρ and κ. However there are large discrepancies between predicted and measured nucleation rates [58, 178]. For example, CNT predicts a nucleation rate for Argon as much as 26 orders of magnitude lower than experimentally measured [178]. The discrepancies are possibly due to the CNT assumption that the initial fluid and final crystal are the only relevant phases [177]. In reality, this may not be true, as proposed by Ostwald's step rule [179]. As such, γ, $\Delta\mu$, ρ and κ may be different if nucleation occurs via intermediate structures. Finally, a lack of a rigorous theoretical form for κ [58], undermines the predictive capabilities of CNT further.

Arguably the most simple system to exhibit crystal nucleation is a dispersion of Brownian

hard spheres. Even for this simple system, nucleation rates predicted by CNT do not agree with those observed by experiments [58]. The disagreement is possibly due to deviations of experimental colloidal dispersions from the perfect hard sphere model such as gravity or a small charge on the particle surfaces [52]. Another explanation is that intermediate structures produce a low γ for critical nuclei to account for the higher measured rates. Evidence for intermediate crystal structures has come from both simulations and confocal microscopy of colloidal dispersions [52,53,175,177] which reveal single particle arrangements during nucleation.

The analysis of microscopic arrangements of particles during crystal nuclation is heavily reliant on selecting crystalline particles from the fluid using the bond orientational order parameters, as proposed by Steinhardt et al. [149] and made popular by Frenkel and coworkers [180–182]. These order parameters are based on spherical harmonics and enable the crystalline assignment of individual particles based on their relative neighbour positions. As such, they provide a way to search for crystals with high spatial resolution, at the single particle level. However, bond-orientational order parameters rely on thresholds to distinguish between crystal structures like face centered cubic or hexagonal close packed and, as such, crystal structure assignment is open to interpretation. Furthermore, it is not possible to explicitly measure the misorientations within (or between) nuclei. To overcome these obstacles, we use the method defined in the previous chapter. Crystal structure is determined through a minimisation procedure and is therefore, not subject to thresholds. Additionally, the method allows for measurement of misorientation within nuclei, providing detailed information about the crystalline order. Importantly, the method offers these advantages while retaining the same high spatial resolution offered by bond-orientational order parameters. Therefore, we are able to quantitatively resolve rotational disorder of crystal structures within nuclei over space and time.

In the following sections, we begin by describing the experimental details for the preparation and microscopy of the homogeneously nucleating colloidal dispersion. Next, we measure the nuclei growing to form randomly hexagonally close packed crystals and show how our alternative crystalline assignment agrees with the conventional bond-orientational order metric. Then, we examine the global intra-nuclei misorientation distributions during nucleation, revealing a change as nucleation progresses in time. Finally, we show the microscopic spatial distribution of intra-nuclei misorientation angles, observing lower angles in the nuclei cores than on their surfaces.

6.2 Methods

6.2.1 Sample preparation

The colloidal crystals were prepared identically to the ones described in section 5.4.2 of the previous chapter, based on the methods presented in references [173,174]. The colloidal samples are composed of $\approx 2\mu$m diameter, $p = 0.03$ polydisperse, polydimethylsiloxane stabilized PMMA spheres. The particles are suspended in a density and index matching mixture of cyclohexyl bromide and cis-decahydronaphthalene saturated with tetrabutylammonium bromide (TBAB) to achieve a very short ranged, screened Yukawa potential. Therefore, these particles act as quasi-hard spheres. The particles are dyed with trace amounts of cumarin for fluorecent imaging using a confocal scan head on a Leica SP5 microscope. The particle coordinates are recovered from the confocal images with a $100 \times 100 \times 30$ μm^3 ($x \times y \times z$) field of view using conventional particle identification software [80]. To suppress heterogeneous nucleation, the glass walls of the sample cell were coated with a polydisperse $p = 0.3$ colloidal PMMA to create a uniform but rough surface on the length scale of the colloidal particles. A colloidal sample with $\phi = 0.52$ is introduced to the sample cell, placed on the microscope and imaged over several hours as the crystallites nucleate and grow. The colloidal dispersion was 1 mm thick and a field of view roughly 20 μm way from the lower wall was imaged. The volume fraction of particles as a function of time was measured to asses the density matching. We observe a small increase by about 5.8% from $\phi = 0.52$ to $\phi = 0.55$ (see Fig.6.1a) over 4 hours owing to a slight sedimentation of the particles (parallel to z). However, the volume fraction remains in a region of the phase diagram where the colloidal crystal is the thermodynamically most stable phase throughout the experiment.

6.2.2 Crystalline proportion and structure analysis

The proportion of crystalline particles may be calculated using *bond coherence*, d_6, a type of bond-orientational order parameter [52, 149, 180, 183, 184]. This parameter is calculated from the nearest neighbour clusters of two neighbouring particles and varies from $d_6 = 0$ for two liquid-like neighbours to $d_6 = 1$ for two perfectly crystalline (FCC or HCP) neighbours (see appendix 6.5.1). A particle is defined as locally crystalline if it has 6 or more neighbours with

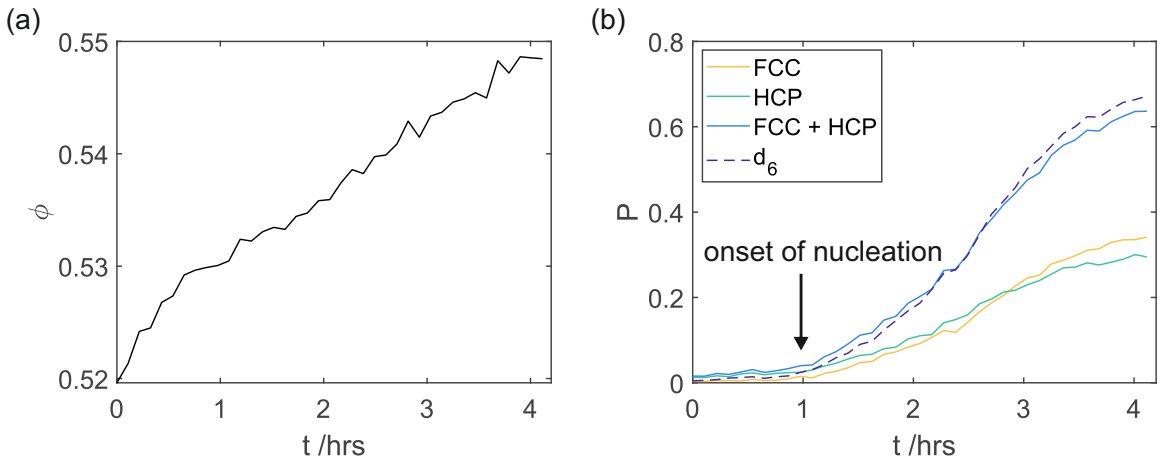


Figure 6.1: (a) Volume fraction time dependence. (b) Proportion of FCC, HCP and crystalline particles over time. The proportion of FCC and HCP particles is given by curve FCC + HCP and is one way of measuring the proportion of crystalline particles. Curve d_6 shows another measure for the proportion of crystalline particles, this time measured by bond coherence (see main text for details).

bond coherence values greater than $d_6 = 0.7$ [183]. The proportion, P, of crystalline particles is calculated as the number of locally crystalline particles divided by the total number of particles (excluding the edges) and is plotted as the dashed line in Fig.6.1b. We observe the onset of nucleation, when nuclei first begin to persist and P increases after $t \approx 1$ hours which then rises quickly during grain growth, before reaching a plateau $t = 4.2$ hours when the field of view becomes dominated by crystalline particles.

We may also calculate the proportion of crystalline particles in a different way using the method detailed in chapter 5 (section 5.3). Crystalline structures are measured by comparing the nearest neighbour clusters of each particle against those for perfect face centered cubic, FCC, hexagonal close packed, HCP, and body centered cubic, BCC, structures (see section 5.3.3). Then, several thresholds determine the crystalline particles. Firstly, a distance cut off which determines if two particles are close enough in space to be in the same grain is set to R_{cut} as defined above. Secondly, we select the misorientation cut off, θ_{cut}, which evaluates whether two particles have similar enough orientations to be considered within the same grain, is set to $\theta_{\text{cut}} = 11°$. Lastly, we impose a threshold on the smallest grain size of 6, similarly to the requirement for 6 or more neighbours with d_6 values greater than 0.7 in the bond orientational order parameter definition of crystalline particles. Therefore, particles that belong to a grain larger than or equal to 6 members, are assigned as crystalline, and the rest are assigned as liquid-like. In the following sections, we adopt this definition for crystalline particles. Likewise, FCC, HCP and BBC particles are those that exist in grains with at least 6 members. The above

thresholds, $\theta_{\text{cut}} = 11^\circ$ and minimum grain size = 6 particles, where chosen so that the variation of the proportion, P, of crystalline particles with time using this method agrees well with that measured using d_6 (see Fig.6.1b). Note that these thresholds distinguish between liquid-like structure and a particular crystal structure, and do not distinguish *between* crystal structures. Different crystal structures are distinguished in a threshold independent manner by following the minimisation procedure described in section 5.3.2.

6.3 Results and discussion

6.3.1 Nucleation and growth

Fistly, we monitor the crystal structures over time. The variation for the proportion of FCC and HCP individually is shown in Fig.6.1b, and we see that the proportion of FCC and HCP remains approximately equal throughout, suggesting the formation of a random hexagonal close packed, RHCP, crystal structure. We find that no particles are measured as having nearest neighbours in BCC structure and therefore, there are no crystalline particles in BCC grains. Then, the individual crystalline particles are detected for and plotted in space for snapshots in time. Three instances are shown in Fig.6.2a, b and c for times $t = 1.2$, 2.2 and 4.1 hours, respectively. These snapshots uncover the nuclei structures observed during crystal growth from a time shortly after the onset of nucleation. We see several crystal nucleation events from within the field of view that grow to form larger crystal nuclei, consisting of multiple grains. We observe that some smaller features identified do not persist and dissolve, suggesting that nuclei may be observed at pre-critical sizes using this method.

6.3.2 Intra-nuclei misorientation during nucleation

Next, we determine the misorientation relationships within crystal nuclei, in other words, intra-nuclei misorientations. To this end, we calculate the misorientations between neighbouring pairs of crystalline particles, where neighbours are connected by a Delaunay triangulation edge shorter than R_{cut}. In this way, misorientations between nuclei are excluded as nuclei surfaces are separated by a distance greater than R_{cut}. A brief discussion of nearest neighbour definitions is given in appendix 6.5.3. We start by considering the distibution of misorientation angles, θ,

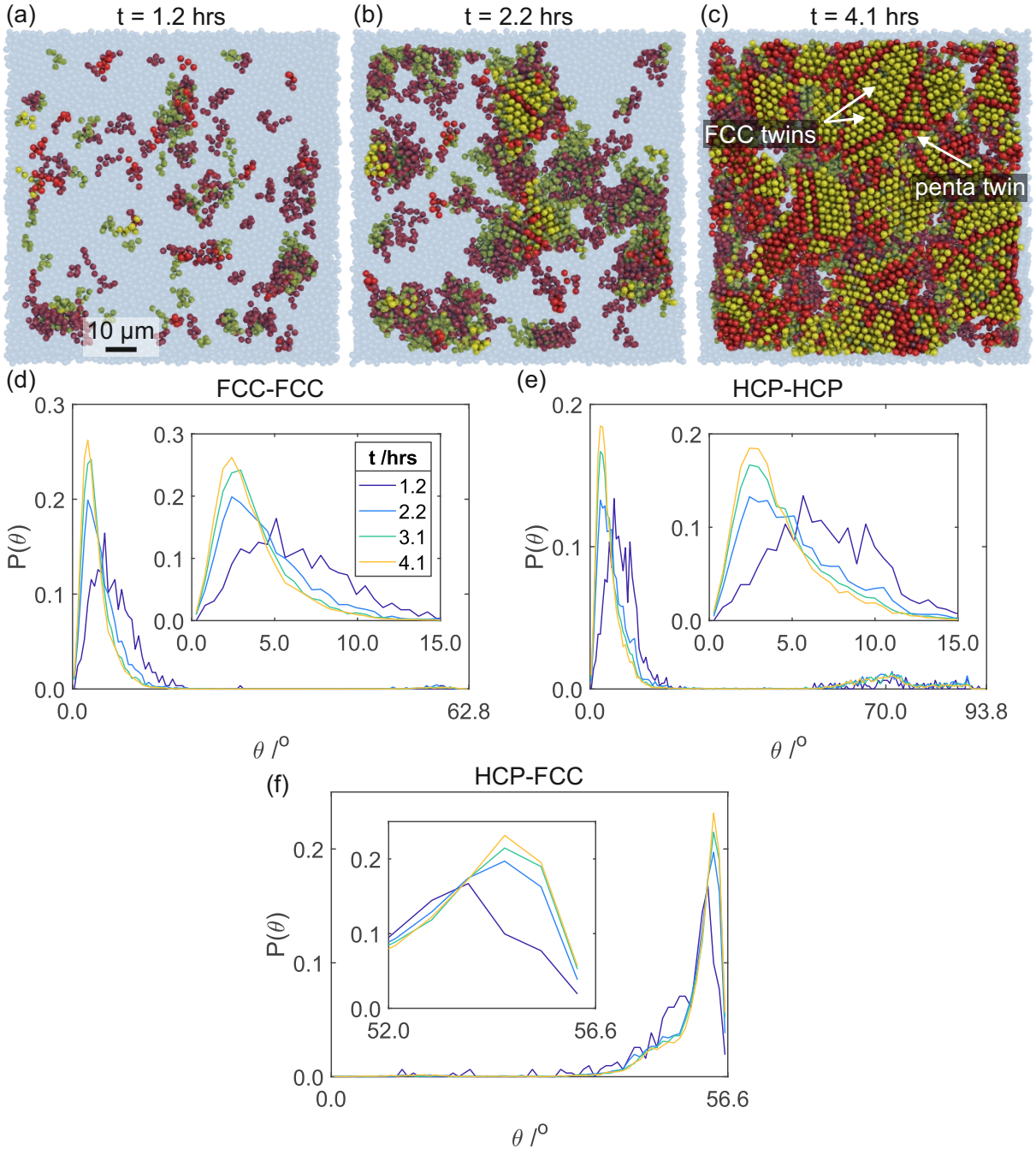


Figure 6.2: (a), (b) and (c) show crystal nucleation over several hours at early, intermediate and late time, respectively. The perspective in normal to the xy plane of the field of view and the snapshots show the entire depth in z. Particles coloured in yellow or red have FCC or HCP structure, respectively. Liquid-like particles are plotted as partially transparent blue. Panels (d), (e) and (f) show misorientation angle distribution between pairs of FCC neighbours, HCP neighbours and between HCP and FCC neighbours respectively. The insets show magnified regions of the misorientation angle distributions.

between FCC neighbours. The distributions at several times after the onset of nucleation is shown in Fig.6.2d. At each time, the distribution is dominated by low angle misorientations, as shown by the peak $\theta \approx 0^\circ$ at times $t = 1.2, 2.2, 3.1$ and 4.1 hours. The $\theta \approx 0^\circ$ peak shows that FCC crystal growth is dominated by single orientation grains growing in distinct regions away from other differently oriented FCC grains. Secondly, we examine the misorientation angle distribution between HCP neighbours over time. The distributions shown in Fig.6.2e are similar to the distributions between FCC neighbours, where the distribution is dominated by a peak at $\theta \approx 0^\circ$ at all times. Correspondingly, the $\theta \approx 0^\circ$ peak shows that HCP grain growth is also dominated by single orientation grains growing in distinct regions. Next, we consider the misorientation angle distribution between HCP-FCC neighbours, where one neighbour is FCC and the other HCP, as shown in Fig.6.2f. Here, we see that the misorientation angle distribution is dominated by high angles near the stacking fault misorientation angle of $\theta \approx 56.6^\circ$ [172] at all times, thereby showing the prevalence of stacking faults. Thus, the three distributions from Fig.6.2d-f show that staking faults are present from early stages of nucleation, and persist through crystal growth. Therefore, nuclei grow as collections of HCP and FCC grains in an RHCP arrangement, agreeing with observations from scattering experiments [185,186] and from confocal microscopy [52].

The presence of stacking faults means that nuclei often contain multiple FCC or HCP grains with differing orientations related by the geometric constraints of stacking faults. Firstly, we consider FCC orientations. In an RHCP crystal there may be FCC twin grains[1] present if two FCC grains are separated by an odd number of HCP layers. Examples of such FCC twins are marked on Fig.6.2c. However, the peak at $\theta = 60^\circ$, corresponding to FCC twinning, is negligibly small in Fig.6.2d because FCC twin grains are intersected by HCP grains, so they sit further away from each other than R_{cut}. Secondly, we consider HCP orientations. The small peak at $\theta \approx 70^\circ$ in Fig.6.2e reveals different orientations of HCP grains within nuclei. The misorientation angle is $\theta \approx 70^\circ$ because of geometric constrains of close packing. Consider building an RHCP crystal by starting with several particles arranged in a hexagonal layer, and continue by adding layers of hexagonally packed particles in random lateral A, B or C positions (see section 2.2.1). Eventually, the random stacking will create a region of FCC. In FCC, there are four hexagonal plane directions that intersect each other at an angle of $\theta = 70.53^\circ$. Therefore, if we continue building RHCP, but select one of the alternative four hexagonal plane

[1]FCC grains separated by a 60° misorientation about a rotation axis parallel to a {111} lattice direction.

directions on which to place the next hexagonal layer, the RHCP crystal will now contain HCP domains with a misoriention of $\theta = 70.53°$. The peak at $\theta \approx 70°$ results from the positions where these HCP grains meet. A salient example of such a position is at the centre of a penta-twin. Here, five of these HCP grains (which separate twinned FCC grains) can meet to create penta-twins[2], an example of which is marked on Fig.6.2c. We observe an increase in the proportion of $\theta \approx 70°$ misorientations over time in Fig.6.2e. The increase occurs because each added layer of hexagonally packed particles, there is a chance that a new hexagonal stacking direction will emerge from regions of FCC. As the number of hexagonal layers increases during crystal growth, the probability of a change in direction increases. Furthermore, as the crystals grow, the likelihood of these two HCP orientations growing towards each other and meeting increases. Therefore, we see an increase in the proportion of $\theta \approx 70°$ neighbour misorientations as time progresses.

Next, we inspect the low angle misorientations between FCC neighbours in more detail. The inset of Fig.6.2d shows a magnified portion of the misorientation angle distribution where we observe that the low angle peak is intially broad, with a peak at $\theta \approx 6°$ for the time $t = 1.2$ hours, shortly after the onset of nucleation. Over time, the peak becomes sharper and shifts to a lower misorientation angle, arriving at $\theta \approx 2.5°$ at $t = 4.1$ hours. Similarly, we inspect the low angle distribution between HCP neighbours in more depth. The inset of Fig.6.2e shows a magnified portion of the distribution, where the trend is approximately the same as between FCC neighbours. Crucially, figures 6.2d and e show a decrease in intra-nuclei misorientation as nuclei grow and we see that the FCC and HCP neighbours shortly after the onset of nucleation have higher misorientation angles with a greater spread than those at late time. The change in distribution to lower misorientation angles shows that nuclei formed at initial times are more orientationally disordered from those at late times.

We may also examine the stacking faults in more detail by magnifying the high angle peak from Fig.6.2f, shown in the inset. Here too, we see an initially broad peak at $\theta \approx 53°$ shortly after the onset of nucleation at $t = 1.2$ hours. As time progresses, we see the misorientation angle peak sharpen and increase to $\theta \approx 54°$ towards the angle for a stacking fault between a perfect FCC and HCP crystal, $\theta = 56.6°$ [172]. This shows that the stacking faults in initial nuclei are less ordered than in their late time counterparts.

[2]These structures are slighly frustrated as $5 \times 70.53° = 352.65° < 360°$.

6.3.3 Spatial misorientation variation

We uncover more detail during nucleation by exploring the spatial distribution of intra-nuclei misorientations over time. This is achieved by plotting the midpoints between crystalline neighbours, which are given a colour according to the misorientation angle. We use a colour bar to map misorientation angles between $1^\circ < \theta < 5^\circ$ and consider that high and low misorientation angles to be those above or below 5°, respectively. Spatial distributions in misorientation angle between FCC neighbours and between HCP neighbours for several instances in time during nucleation and growth are shown in Fig.6.3a-f. Shortly after nucleation onset at $t = 1.1$ hours (see Fig.6.3a), we see small distinct patches of points corresponding to nuclei in the initial stages of growth. These initial nuclei contain misorientation angles dominated by high angles. As time progresses, (see Fig.6.3b-d) the larger nuclei persist and grow while others vanish. As the nuclei grow, the misorientations in their cores decrease, as shown in Fig.6.3e-f. However, the outer edges of the nuclei retain high misorientation angles. This shows that the structure that forms at the early stage of nucleation is distinct from the late time crystal. The initial structure contains mostly high misorientation angles between neighbouring crystalline particles, whereas, the late time structure contains low misorientation angles at the core and high only at the surface. These nuclei are also structurally distinct from the liquid having neighbour misorientation angles of $\theta < 11^\circ$, as defined above.

6.3.4 Isolating a homogeneous nucleation event

Next, a small field of view with dimensions 16 μm × 16 μm × 24 μm ($x \times y \times z$) is isolated to observe a single nucleation event at early time with greater magnification. The nucleus can be seen at approximately centre top of the panels in Fig.6.3. A snapshot shortly after nucleation at $t = 0.98$ hours, which shows a nucleus surrounded by liquid-like particles, is displayed in Fig.6.4a. Two later snapshots at $t = 1.2$ and 1.4 hours are shown in Fig.6.4b and c, respectively. They display the growth of the nucleus within the field of view, surrounded by liquid-like particles. Within the same field of view, we reveal the misorientation as before, by colouring the midpoints between neighbouring crystalline particles by the misorientation angle. Snapshots for the same three times, $t = 0.96$, 1.2 and 1.4 hours, are shown in Fig.6.4d-f respectively, where we use the same colour scheme for misorientation angles as before (see Fig.6.4d). These snapshots show

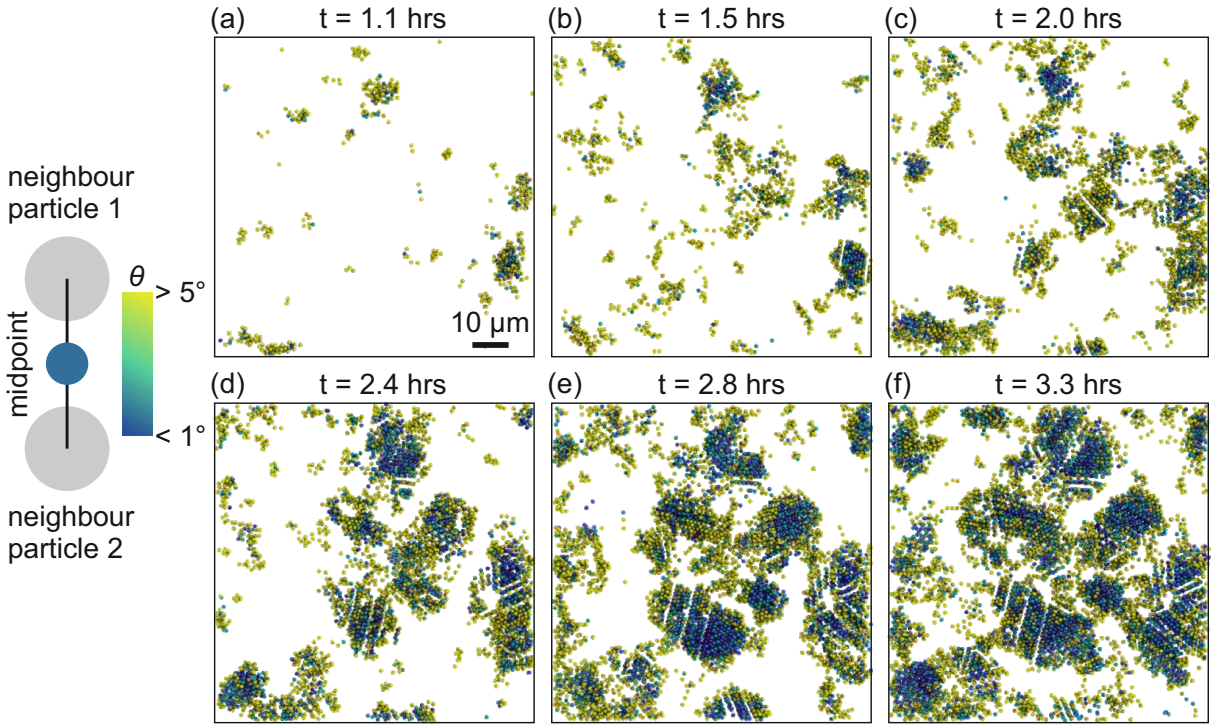


Figure 6.3: Spatial distribution of intra-nuclei misorientation angle, θ. The perspective is normal to the xy plane of the field of view and shows $0 < z < 15$ µm in depth. The neighbour midpoints (see schematic on the left) are coloured according to the colour bar shown on the left. The thresholds of the colour bar are set to clearly show the changes in misorientation over time and space. Patches of points show the position of nuclei. Time increases from panels (a) to (f).

the misorientation angles are initially high ($\theta > 5°$). Later, at time $t = 1.2$ hours (see Fig.6.4e), the inter-neighbour misorientation decreases mostly towards the core of the nucleus. By time $t = 1.4$ hours, we see that the core with lower inter-neighbour misorientation has grown and is surrounded by higher inter-neighbour misorientations at the surface of the nucleus (see Fig.6.4f). This supports the observations of section 6.3.3, where initial nuclei have higher misorientations between their neighbours, but at later time, a structure with lower misorientation in the core and higher misorientation at the surface is formed.

The mean inter-neighbour misorientation angle, $\langle\theta\rangle$, is calculated to reveal the time evolution and is plotted for FCC neighbours and HCP neighbours in Fig.6.4g. Both trends are approximately equal, starting at $\langle\theta\rangle \approx 7°$ which decreases over time to a plateau value of $\langle\theta\rangle \approx 2.5°$ after $t \approx 3$ hours, where the core of the nucleus dominates the field of view. This result supports the observation of higher neighbour misorientation angles in nuclei at early time.

Next, we measure the radial profile of the neighbour misorientations from the centre of the nucleus which is presented in Fig.6.4h for several times. We see that the misorientation angle increases with distance from the nucleus centre, revealing the spatial dependence of the misorientation angle from nucleus core to surface. As time progresses, the misorientation angles near the centre decrease, but remain high at the surface. This suggests that the orientations of neighbouring particles get more similar as they spend a longer time together in the nucleus core, during which their surrounding NNC has time to sample configurational space to minimise the free energy. The particles arrive at the surface of the nucleus, at high r, have spent less time amongst their crystalline neighbours and have not reached the optimum configuration to minimise their free energy. Thus, the particles arriving at the surface show higher misorientations between their neighbours. What remains unclear is whether the low misorientations in the core at late time are a consequence of the longer time spent next to their neighbours, or a consequence of nucleus size where larger particle fluctuations at the fluid-liquid interface account for a smaller proportion of the nucleus.

The shape of the radial profiles shows that the gradients of $\langle\theta\rangle$ with r change over time. At initial nucleation ($t = 0.98$), the gradient is constant, and varies smoothly from low to high misorientation. Therefore, we may wish to define the nucleus radius, r, for some maximum value of $\langle\theta\rangle$. However, there is no clear choice of value, showing that during nucleation, the fluid-crystal interface is diffuse, in agreement with simulations of a Lennard-Jones system [187],

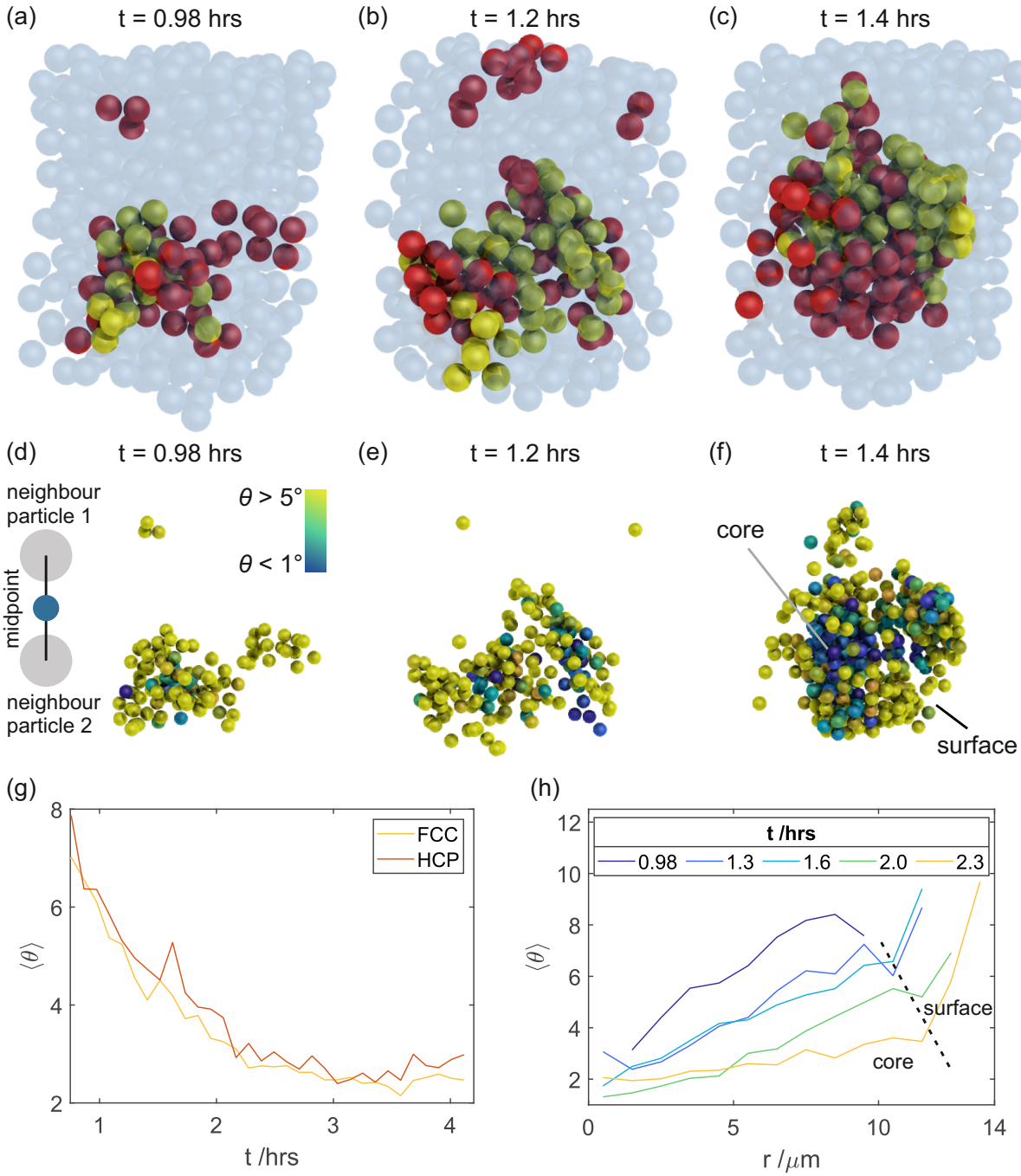


Figure 6.4: A single nucleation event isolated within a 16 × 16 × 24 μm^3 ($x \times y \times z$) field of view. (a)-(c) show early time snapshots of nucleation, where HCP, FCC and liquid-like particles are coloured in red, yellow and transparent blue respectively. (d)-(f) show the same snapshots where the misorientations between neighbouring particles within grains are plotted at the neighbour particle midpoints (see the schematic in panel (d)). These points are coloured by the misorientation angle as indicated by the colour map in panel (d). (g) Time dependence of mean misorientation angle, $\langle\theta\rangle$, within the field of view. (h) Radial profile of mean misorientation angle as a function of distance from the centre of the nucleus, r.

density functional calculations of hard spheres [188] and qualitative observations from CLSM on a similar colloidal system [52]. Thus, it is hard to determine r, γ, ρ and $\Delta\mu$, and consequently, a reliable prediction of nucleation rates from CNT is difficult. As time progresses, this gradient decreases within the core, but remains high at the surface. To guide the eye the approximate position of the core-surface interface is marked by the dashed line in Fig.6.4h. The changes in gradient show that the disorder of the nucleus core and surface becomes more dissimilar over time, but the variation is still smooth, making it hard to irrefutably determine the radius of the nucleus.

6.4 Conclusion

A colloidal dispersion was studied to reveal misorientations during homogeneous crystal nucleation of a colloidal dispersion. We observe that within growing nuclei of close packed crystals only misorientations corresponding to stacking faults are observed. This suggests that grain boundaries with different misorientations resulting in a polycrystal are a result of nuclei growing to meet each-other. Furthermore, we observe that initial nuclei are structurally distinct from both the liquid and late time nuclei, having neighbour misorientations with high angles. We see a structural variation of intra-nuclei misorientation over time and within nuclei themselves. Initial nuclei display larger intra-nuclei misorientation angles than mature nuclei which display a core containing low misorientation angles but surfaces containing high angles. This adds to the evidence of intermediate structures [53] and diffuse fluid-crystal interface [187, 188] during nucleation. These results question the assumption of CNT that the final crystal and the fluid are the only phases at play. Intermediate structures and diffuse interfaces may exhibit γ significantly lower than for a sharp interface between liquid and the late time crystal and thus, may accelerate nucleation rates. However, this provides only a qualitative picture, but perhaps highlights the need to measure local γ, ρ and $\Delta\mu$ at the fluid-crystal interface during nucleation. If this is possible, one may predict nucleation rates more accurately.

6.5 Appendix

6.5.1 Bond coherence

The order parameter bond coherence measures the correlation between the bond orientational order of the nearest neighbours of two neigbouring particles. Each of the components of the vector associated with the particle i is given by [149, 183]:

$$q_{6,m} = \frac{1}{N_b(i)} \sum_{j=1}^{N_b(i)} Y_{l,m}(\vec{r}_{ij}), \tag{6.3}$$

where j runs over the number of neighbours of particle i, $N_b(i)$, where $Y_{6,m}$ is a spherical harmonic of order 6 and degree m, which runs from 1 to 13. Order 6 is chosen to replect the hexagonal symmetry of close packed colloidal crystals. The bond coherence between two particles i and j is then calculated as [183]:

$$\begin{aligned} d_6 &= \sum_{m=-6}^{6} \hat{q}_{6,m}(i)\hat{q}^*_{6,m}(j), \text{where,} \\ \hat{q}_{6,m} &= \frac{q_{6,m}}{q_{6,m}q^*_{6,m}}. \end{aligned} \tag{6.4}$$

6.5.2 Crystalline proportion for the isolated nucleus

The crystalline proportion, P, within the field of view that isolates the nucleus presented in figure 6.4, is measured over time to reveal the time dependence. Crystalline proportion is measured, again, as the ratio of the sum of FCC and HCP particles to the total number of particles (excluding edges) and is plotted in Fig.6.5. We observe an increase in P commencing just before $t = 1$ hour, which rises to a plateau at $t = 3$ hours where $P \approx 0.8$ due to the growth of the crystal nucleus. Note that at late time, the nucleus has grown beyond the field of view, but the core remains within view. The proportion of HCP and FCC are approximately equal at early time, but FCC dominates at late time.

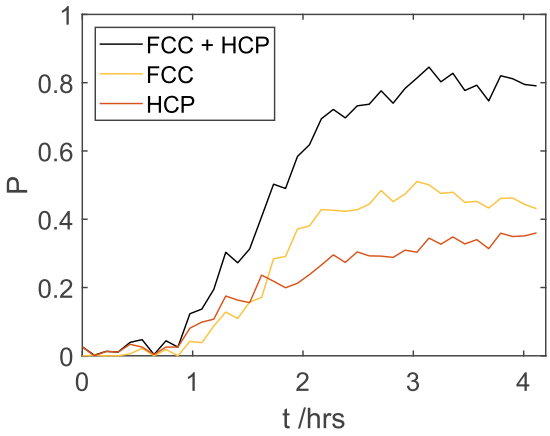


Figure 6.5: Proportions of crystalline (FCC + HCP), FCC and HCP particles within the small field of view containing the isolated nucleus.

6.5.3 Nearest neighbours

There are several ways to define nearest neighbours [189]. Above, we have chosen two very similar metrics to define nearest neighbours in the case of nearest neighbour clusters, NNCs, and in the case of neighbours within nuclei. In the latter we use a Delaunay traingulation. We find that neighbours within nuclei are found identically whether or not a Delaunay triangulation is performed before applying the cut off, R_{cut}. However, if R_{cut} is set too large, nearest neighbours are found differently. The choice of Delaunay triangulation is a technical one: it is advantageous because it allows the same computer code function to be called for both grain boundary and neighbour misorientation measurement. Note that different definitions for NNCs can sometimes produce different results for misorientation and for Steinhardt bond orientational order parameters [189]. We find that if a Delaunay triangulation is imposed on the NNC definition such that nearest neighbours are: *the up to 12 closest neighbours connected by a Delaunay triangulation edge*, neighbours are calculated differently for 0.082 % of particles, with an average difference of 1.3 neighbours. Therefore, for our purposes, the two definitions of nearest neighbours used in the analysis are equivalent. Again, if R_{cut} is set too large, the difference in neighbour assignment increases.

Acknowledgements

Colloidal particle synthesis and data acquisition was performed by T. Yanagishima, who is also thanked for enlightening discussions.

Chapter 7

Conclusion and outlook

The chapters in this thesis have used confocal microscopy and small angle X-ray scattering to explore the ways in which colloidal spheres pack together within a three-dimensional colloidal crystal. In chapter 3 we examined how shear can promote the arrangement of spherical colloidal particles into hexagonal sheets with long range orientational order within RHCP crystals, agreeing with many studies in the literature [95, 101, 104]. We studied the crystallisation mechanism to reveal that a combination of shear alignment and epitaxial crystal growth is responsible for the final crystal. We showed that these crystals can be produced inside of a narrow and flat walled capillary, relatively simply with respect to other methods using shear cells.

In chapter 4, we examined the long term behaviour of these crystals, finding that they persist indefinitely at high enough volume fractions, therefore, broadening their utility. These crystals may serve as a canvas to observe the long term behaviour of both lateral and inter planar FCC-HCP stacking faults. Furthermore, their use may be found within photonic band gap crystals provided that FCC may be selected over HCP. At lower volume fractions, we saw that these crystals break apart to produce many rotated domains of RHCP crystal. We found that crystal rotations initiated near the bottom of the crystal where shear strain rate is highest, before rotations propagate upwards through the crystal via a gearing type mechanism. Notably, the crystallite rotations all shared a common rotation axis to produce an entirely tilt grain boundary network. Such tilt grain boundary crystals may prove useful in grain boundary model studies such as microrheology during grain boundary tweezing. An exclusively tilt grain boundary network constrains two of the eight degrees of freedom of the grain boundary reducing

its complexity. This should facilitate experiments, analysis and perhaps simplify the observed physics.

A method for determining the structure and misorientation of grain boundaries from particle coordinates was detailed in chapter 5. We demonstrated the utility by finding unexpected complexity within the grain boundary structure of a well characterised colloidal bicrystal [57]. Furthermore, we found that lateral HCP-FCC stacking faults produce a signature peak in the misorientation angle distribution at $\theta \approx 49°$, and should aid the description of RHCP crystals. We hope that this method finds wide use in the experimental and simulation communities to find grain boundaries. In the future we hope to add other functionality to the method including the ability to ignore FCC-HCP stacking faults to resolve RHCP grains individually. We hope to add to the number of in built crystal structures the method can identify and to add functionality to determine the reference structure if it is unknown.

Finally, in chapter 6, we examined the misorientational disorder during homogeneous crystal nucleation of a colloidal dispersion. Similarly to several other studies [52, 184, 188], we found that the edge of the crystal nucleus is poorly defined exhibiting a smooth transition from liquid like to crystalline structure. This undermines the assumption of classical nucleation theory that only the liquid and the final crystalline structure are involved during nucleation and may underlie the failures of classical nucleation theory to predict nucleation rates. In this chapter we only considered one data set, owing to the difficulty in sample preparation and acquisition. We hope to obtain more data and examine a greater number of nuclei, both from confocal microscopy of hard sphere colloidal dispesions and from simulation to obtain more statistically significant observations.

Bibliography

[1] D. Fennell Evans and H. Wennerström. *The colloidal domain: Where physics, chemistry, biology, and technology meet* (Wiley, 1999), 2nd edition.

[2] J. Perrin. Mouvement brownien et réalité moléculaire. Annales de Chimie et de Physique **18**, 5 (1909).

[3] W. Poon, P. Pusey, and H. Lekkerkerker. Colloids in suspense. Physics World **9**, 27 (1996).

[4] R. A. L. Jones. *Soft condensed matter* (Oxford University Press, 2002).

[5] W. B. Russel, D. A. Saville, and W. R. Schowalter. *Colloidal dispersions* (Cambridge University Press, 1989).

[6] A. van Blaaderen and P. Wiltzius. Real-Space Structure of Colloidal Hard-Sphere Glasses. Science **270**, 1177 (1995).

[7] M. Doi. *Soft Matter Physics* (Oxford University Press, 2013).

[8] J. N. Israelachvili. *Intermolecular and surface forces* (Academic Press, 2011), 2nd edition.

[9] A. Yethiraj and A. Van Blaaderen. A colloidal model system with an interaction tunable from hard sphere to soft and dipolar. Nature **421**, 513 (2003).

[10] C. P. Royall, D. G. Aarts, and H. Tanaka. Bridging length scales in colloidal liquids and interfaces from near-critical divergence to single particles. Nature Physics **3**, 636 (2007).

[11] H. N. Lekkerkerker and R. Tuinier. *Colloids and the Depletion Interaction*, volume 833 of *Lecture Notes in Physics* (Springer Netherlands, Dordrecht, 2011).

[12] D. H. Napper. Steric stabilization. Journal of Colloid And Interface Science **58**, 390 (1977).

[13] C. M. Van Kats, P. M. Johnson, J. E. Van Den Meerakker, and A. Van Blaaderen. Synthesis of monodisperse high-aspect-ratio colloidal silicon and silica rods. Langmuir **20**, 11201 (2004).

[14] C. Fernández-Rico, T. Yanagishima, A. Curran, D. G. A. L. Aarts, and R. P. A. Dullens. Synthesis of Colloidal SU-8 Polymer Rods Using Sonication. Advanced Materials **31**, 1807514 (2019).

[15] C. Fernández-Rico, M. Chiappini, T. Yanagishima, H. de Sousa, D. G. A. L. Aarts, M. Dijkstra, and R. P. A. Dullens. Shaping colloidal bananas to reveal biaxial, splay-bend nematic, and smectic phases. Science **369**, 950 (2020).

[16] L. Rossi, S. Sacanna, W. T. Irvine, P. M. Chaikin, D. J. Pine, and A. P. Philipse. Cubic crystals from cubic colloids. Soft Matter **7**, 4139 (2011).

[17] S. Sacanna and D. J. Pine. Shape-anisotropic colloids: Building blocks for complex assemblies. Current Opinion in Colloid and Interface Science **16**, 96 (2011).

[18] S. Sacanna, M. Korpics, K. Rodriguez, L. Colón-Meléndez, S. H. Kim, D. J. Pine, and G. R. Yi. Shaping colloids for self-assembly. Nature Communications **4**, 1688 (2013).

[19] A. Kuijk, T. Troppenz, L. Filion, A. Imhof, R. Van Roij, M. Dijkstra, and A. Van Blaaderen. Effect of external electric fields on the phase behavior of colloidal silica rods. Soft Matter **10**, 6249 (2014).

[20] A. L. Thorneywork, J. L. Abbott, D. G. A. L. Aarts, and R. P. A. Dullens. Two-Dimensional Melting of Colloidal Hard Spheres. Physical Review Letters **118**, 158001 (2017).

[21] D. G. Grier. A revolution in optical manipulation. Nature 2003 **424**, 810 (2003).

[22] F. A. Lavergne, A. Curran, D. G. A. L. Aarts, and R. P. A. Dullens. Dislocation-controlled formation and kinetics of grain boundary loops in two-dimensional crystals. Proceedings of the National Academy of Sciences of the United States of America **115**, 6922 (2018).

[23] N. A. Clark, A. J. Hurd, and B. J. Ackerson. Single colloidal crystals. Nature **281**, 57 (1979).

[24] W. L. Vos, M. Megens, C. M. Van Kats, and P. Bösecke. X-ray diffraction of photonic colloidal single crystals. Langmuir **13**, 6004 (1997).

[25] M. Megens, C. M. Van Kats, and P. Bösecke. Synchrotron small-angle X-ray scattering of colloids and photonic colloidal crystals. Journal of Applied Crystallography **30**, 637 (1997).

[26] M. Ballauff. SAXS and SANS studies of polymer colloids. Current Opinion in Colloid and Interface Science **6**, 132 (2001).

[27] S. A. Asher, J. M. Weissman, A. Tikhonov, R. D. Coalson, and R. Kesavamoorthy. Diffraction in crystalline colloidal-array photonic crystals. Physical Review E - Statistical Physics, Plasmas, Fluids, and Related Interdisciplinary Topics **69**, 14 (2004).

[28] P. A. Hassan, S. Rana, and G. Verma. Making sense of Brownian motion: Colloid characterization by dynamic light scattering. Langmuir **31**, 3 (2015).

[29] J. Hilhorst, V. V. Abramova, A. Sinitskii, N. A. Sapoletova, K. S. Napolskii, A. A. Eliseev, D. V. Byelov, N. A. Grigoryeva, A. V. Vasilieva, W. G. Bouwman, K. Kvashnina, A. Snigirev, S. V. Grigoriev, and A. V. Petukhov. Double Stacking Faults in Convectively Assembled Crystals of Colloidal Spheres. Langmuir **25**, 10408 (2009).

[30] G. P. Baeza, A. C. Genix, C. Degrandcourt, L. Petitjean, J. Gummel, M. Couty, and J. Oberdisse. Multiscale filler structure in simplified industrial nanocomposite silica/SBR systems studied by SAXS and TEM. Macromolecules **46**, 317 (2013).

[31] J. H. J. Thijssen, A. V. Petukhov, D. C. 't Hart, A. Imhof, C. H. M. van der Werf, R. E. I. Schropp, and A. van Blaaderen. Characterization of Photonic Colloidal Single Crystals by Microradian X-ray Diffraction. Advanced Materials **18**, 1662 (2006).

[32] P. P. Edwards, A. Porch, M. O. Jones, D. V. Morgan, and R. M. Perks. Basic materials physics of transparent conducting oxides. Dalton Transactions **19**, 2995 (2004).

[33] R. S. Datta, N. Syed, A. Zavabeti, A. Jannat, M. Mohiuddin, M. Rokunuzzaman, B. Yue Zhang, M. A. Rahman, P. Atkin, K. A. Messalea, M. B. Ghasemian, E. D. Gaspera, S. Bhattacharyya, M. S. Fuhrer, S. P. Russo, C. F. McConville, D. Esrafilzadeh, K. Kalantar-Zadeh, and T. Daeneke. Flexible two-dimensional indium tin oxide fabricated using a liquid metal printing technique. Nature Electronics **3**, 51 (2020).

[34] J. D. Watson and F. H. C. Crick. Molecular structure of nucleic acids: A structure for deoxyribose nucleic acid. Nature **171**, 737 (1953).

[35] R. E. Franklin and R. G. Gosling. Molecular configuration in sodium thymonucleate. Nature **171**, 740 (1953).

[36] M. J. Adams, T. L. Blundell, E. J. Dodson, G. G. Dodson, M. Vijayan, E. N. Baker, M. M. Harding, D. C. Hodgkin, B. Rimmer, and S. Sheat. Structure of rhombohedral 2 zinc insulin crystals. Nature **224**, 491 (1969).

[37] T. L. Blundell, J. F. Cutfield, S. M. Cutfield, E. J. Dodson, G. G. Dodson, D. C. Hodgkin, D. A. Mercola, and M. Vijayan. Atomic positions in rhombohedral 2-zinc insulin crystals. Nature **231**, 506 (1971).

[38] T. A. Wertime. Man's first encounters with metallurg. Science **146**, 1257 (1964).

[39] E. O. Hall. The deformation and ageing of mild steel: III Discussion of results. Proceedings of the Physical Society. Section B **64**, 747 (1951).

[40] N. J. Petch. The cleavage strength of polycrystals. J. Iron and Steel Institute **173**, 25 (1953).

[41] J. Schiøtz, F. D. Di Tolla, and K. W. Jacobsen. Softening of nanocrystalline metals at very small grain sizes. Nature **391**, 561 (1998).

[42] L. Lu, M. L. Sui, and K. Lu. Superplastic extensibility of nanocrystalline copper at room temperature. Science **287**, 1463 (2000).

[43] P. Jiang, K. S. Hwang, D. M. Mittleman, J. F. Bertone, and V. L. Colvin. Template-directed preparation of macroporous polymers with oriented and crystalline arrays of voids. Journal of the American Chemical Society **121**, 11630 (1999).

[44] R. C. Schroden, M. Al-Daous, C. F. Blanford, and A. Stein. Optical properties of inverse opal photonic crystals. Chemistry of Materials **14**, 3305 (2002).

[45] A. P. Hynninen, J. H. J. Thijssen, E. C. M. Vermolen, M. Dijkstra, and A. Van Blaaderen. Self-assembly route for photonic crystals with a bandgap in the visible region. Nature Materials **6**, 202 (2007).

[46] R. D. Meade, A. Devenyi, J. D. Joannopoulos, O. L. Alerhand, D. A. Smith, and K. Kash. Novel applications of photonic band gap materials: Low-loss bends and high Q cavities. Journal of Applied Physics **75**, 4753 (1994).

[47] G. A. Ozin and S. M. Yang. The Race for the Photonic Chip: Colloidal Crystal Assembly in Silicon Wafers. Advanced Functional Materials **11**, 95 (2001).

[48] R. K. Cersonsky, J. Antonaglia, B. D. Dice, and S. C. Glotzer. The diversity of three-dimensional photonic crystals. Nature Communications **12**, 2543 (2021).

[49] P. N. Pusey and W. Van Megen. Phase behaviour of concentrated suspensions of nearly hard colloidal spheres. Nature **320**, 340 (1986).

[50] B. J. Alder and T. E. Wainwright. Phase transition for a hard sphere system. The Journal of Chemical Physics **27**, 1208 (1957).

[51] W. G. Hoover and F. H. Ree. Melting transition and communal entropy for hard spheres. The Journal of Chemical Physics **49**, 3609 (1968).

[52] U. Gasser, E. R. Weeks, A. Schofield, P. N. Pusey, and D. A. Weitz. Real-space imaging of nucleation and growth in colloidal crystallization. Science **292**, 258 (2001).

[53] P. Tan, N. Xu, and L. Xu. Visualizing kinetic pathways of homogeneous nucleation in colloidal crystallization. Nature Physics **10**, 73 (2014).

[54] I. Buttinoni and R. P. A. Dullens. Mechanical properties of colloidal crystals at fluid interfaces. JPhys Materials **4**, 025001 (2021).

[55] J. Hilhorst and A. V. Petukhov. Variable Dislocation Widths in Colloidal Crystals of Soft Thermosensitive Spheres. Physical Review Letters **107**, 095501 (2011).

[56] F. A. Lavergne, D. G. A. L. Aarts, and R. P. A. Dullens. Anomalous grain growth in a polycrystalline monolayer of colloidal hard spheres. Physical Review X **7**, 041064 (2017).

[57] E. Maire, E. Redston, M. P. Gulda, D. A. Weitz, and F. Spaepen. Imaging grain boundary grooves in hard-sphere colloidal bicrystals. Physical Review E **94**, 042604 (2016).

[58] S. Auer and D. Frenkel. Prediction of absolute crystal-nucleation rate in hard-sphere colloids. Nature **409**, 1020 (2001).

[59] R. Brown. A brief account of microscopical observations made in the months of June, July and August 1827, on the particles contained in the pollen of plants; and on the general existence of active molecules in organic and inorganic bodies. Edinburgh New Philosophical Journal **4**, 161 (1828).

[60] A. Einstein. The theory of the brownian movement. Annalen der Physik **17**, 549 (1905).

[61] W. Sutherland. The measurement of large molecular masses. In *Australasian Association for the Advancement of Science. Report of Meeting. (10)*, 117–121. (Dunedin, 1904).

[62] B. Derjaguin and L. Landau. Theory of the stability of strongly charged lyophobic sols and of the adhesion of strongly charged particles in solutions of electrolytes. Progress in Surface Science **43**, 30 (1993).

[63] E. J. Verwey. Theory of the stability of lyophobic colloids. Journal of Physical and Colloid Chemistry **51**, 631 (1947).

[64] R. M. J. Jacobs. Private communication. Oxford (2016).

[65] R. J. Pugh, T. Matsunaga, and F. M. Fowkes. The dispersibility and stability of carbon black in media of low dielectric constant. 1. Electrostatic and steric contributions to colloidal stability. Colloids and Surfaces **7**, 183 (1983).

[66] S. K. Sainis, V. Germain, C. O. Mejean, and E. R. Dufresne. Electrostatic interactions of colloidal particles in nonpolar solvents: Role of surface chemistry and charge control agents. Langmuir **24**, 1160 (2008).

[67] T. Yanagishima, Y. Liu, H. Tanaka, and R. P. A. Dullens. Particle-Level Visualization of Hydrodynamic and Frictional Couplings in Dense Suspensions of Spherical Colloids. Physical Review X **11**, 021056 (2021).

[68] Y. Liu, T. Yanagishima, A. Curran, K. V. Edmond, S. Sacanna, and R. P. A. Dullens. Colloidal Organosilica Spheres for Three-Dimensional Confocal Microscopy. Langmuir **35**, 7962 (2019).

[69] G. Bosma, C. Pathmamanoharan, E. H. De Hoog, W. K. Kegel, A. Van Blaaderen, and H. N. Lekkerkerker. Preparation of monodisperse, fluorescent PMMA-latex colloids by dispersion polymerization. Journal of Colloid and Interface Science **245**, 292 (2002).

[70] W. K. Kegel and A. Van Blaaderen. Direct observation of dynamical heterogeneities in colloidal hard-sphere suspensions. Science **287**, 290 (2000).

[71] C. Kittel. *Introduction to solid state physics* (John Wiley & Sons, Ltd, 1953).

[72] H. van der Hulst. *Light Scattering by Small Particles* (Dover Publications, Inc, New York, 1981).

[73] B. L. Henke, E. M. Gullikson, and J. C. Davis. X-ray interactions: Photoabsorption, scattering, transmission, and reflection at E = 50-30, 000 eV, Z = 1-92. Atomic Data and Nuclear Data Tables **54**, 181 (1993).

[74] The Centre for X-Ray Optics. Index of Refraction. https://henke.lbl.gov/optical_constants/getdb2.html [Accessed 2021-02-11] .

[75] A. G. de Beer and A. V. Petukhov. A simple model for dynamic small-angle X-ray diffraction in colloidal crystals. Journal of Applied Crystallography **40**, 144 (2007).

[76] Y. Liu, K. V. Edmond, A. Curran, C. Bryant, B. Peng, D. G. A. L. Aarts, S. Sacanna, and R. P. A. Dullens. Core-Shell Particles for Simultaneous 3D Imaging and Optical Tweezing in Dense Colloidal Materials. Advanced Materials **28**, 8001 (2016).

[77] C. van der Wel, R. K. Bhan, R. W. Verweij, H. C. Frijters, Z. Gong, A. D. Hollingsworth, S. Sacanna, and D. J. Kraft. Preparation of Colloidal Organosilica Spheres through Spontaneous Emulsification. Langmuir **33**, 8174 (2017).

[78] P. Sollich. Predicting phase equilibria in polydisperse systems. Journal of Physics Condensed Matter **14**, R79 (2002).

[79] M. Minsky. Memoir on inventing the confocal scanning microscope. Scanning **10**, 128 (1988).

[80] J. C. Crocker and D. G. Grier. Methods of digital video microscopy for colloidal studies. Journal of Colloid and Interface Science **179**, 298 (1996).

[81] C. Hammond. *The basics of crystallography and diffraction* (Oxford University Press, 2015), 4th edition.

[82] A. Guinier. *X-ray Diffraction in Crystals, Imperfect Crystals, and Amorphous Bodies* (Courier Corporation, Chelmsford, Massachusetts, USA, 1994).

[83] A. Wilson. *X-ray optics, the diffraction of X-rays by finite and imperfect crystals* (Methuen, 1962).

[84] J. M. Manski, A. J. van der Goot, and R. M. Boom. Advances in structure formation of anisotropic protein-rich foods through novel processing concepts. Trends in Food Science and Technology **18**, 546 (2007).

[85] G. C. Beroza and S. Ide. Slow Earthquakes and Nonvolcanic Tremor. Reviews of Geophysics **39**, 271 (2011).

[86] N. Y. Lin, C. Ness, M. E. Cates, J. Sun, and I. Cohen. Tunable shear thickening in suspensions. Proceedings of the National Academy of Sciences of the United States of America **113**, 10774 (2016).

[87] X. Cheng, J. H. McCoy, J. N. Israelachvili, and I. Cohen. Imaging the microscopic structure of shear thinning and thickening colloidal suspensions. Science **333**, 1276 (2011).

[88] T. C. B. McLeish and R. C. Ball. A molecular approach to the spurt effect in polymer melt flow. Journal of Polymer Science Part B: Polymer Physics **24**, 1735 (1986).

[89] J. B. Salmon, A. Colin, and D. Roux. Dynamical behavior of a complex fluid near an out-of-equilibrium transition: Approaching simple rheological chaos. Physical Review E **66**, 031505 (2002).

[90] T. G. Mason, J. N. Wilking, K. Meleson, C. B. Chang, and S. M. Graves. Nanoemulsions: Formation, structure, and physical properties. Journal of Physics Condensed Matter **18**, R635 (2006).

[91] J. Vermant and M. J. Solomon. Flow-induced structure in colloidal suspensions. Journal of Physics Condensed Matter **17**, 187 (2005).

[92] R. G. Larson. *The structure and rheology of complex fluids* (Oxford University Press, New York, Oxford, 1999).

[93] M. Joy, T. Muangnapoh, M. A. Snyder, and J. F. Gilchrist. Flow-induced alignment of (100) fcc thin film colloidal crystals. Soft Matter **11**, 7092 (2015).

[94] M. J. Miyama and S. I. Sasa. Shear-induced criticality near a liquid-solid transition of colloidal suspensions. Physical Review E **83**, 020401 (2011).

[95] Y. L. Wu, D. Derks, A. Van Blaaderen, and A. Imhof. Melting and crystallization of colloidal hard-sphere suspensions under shear. Proceedings of the National Academy of Sciences of the United States of America **106**, 10564 (2009).

[96] N. Koumakis, J. F. Brady, and G. Petekidis. Amorphous and ordered states of concentrated hard spheres under oscillatory shear. Journal of Non-Newtonian Fluid Mechanics **233**, 119 (2016).

[97] S. Hess and H. J. Hanley. Distortion of the structure of a simple fluid. Physical Review A **25**, 1801 (1982).

[98] A. R. Rennie, S. Barè, J. K. Cockcroft, and A. C. Jupe. Characterization of the flow of anisotropic colloidal particles using energy-dispersive X-ray diffraction. Journal of Colloid and Interface Science **293**, 475 (2006).

[99] S. J. S. Qazi, A. R. Rennie, I. Tucker, J. Penfold, and I. Grillo. Alignment of dispersions of plate-like colloidal particles of Ni(OH) 2 induced by elongational flow. Journal of Physical Chemistry B **115**, 3271 (2011).

[100] S. J. S. Qazi, A. R. Rennie, and J. K. Cockcroft. Orientation of a dispersion of kaolinite flowing in a jet. Langmuir **28**, 3704 (2012).

[101] L. T. Shereda, R. G. Larson, and M. J. Solomon. Boundary-Driven Colloidal Crystallization in Simple Shear Flow. Physical Review Letters **105**, 228302 (2010).

[102] V. L. Colvin. From opals to optics: Colloidal photonic crystals. MRS Bulletin **26**, 637 (2001).

[103] V. V. Abramova, A. S. Sinitskii, N. A. Grigor'Eva, S. V. Grigor'Ev, D. V. Belov, A. V. Petukhov, A. A. Mistonov, A. V. Vasil'Eva, and Y. D. Tret'Yakov. Ultrasmall-angle X-ray scattering analysis of photonic crystal structure. Journal of Experimental and Theoretical Physics **109**, 29 (2009).

[104] M. D. Haw, W. C. Poon, and P. N. Pusey. Direct observation of oscillatory-shear-induced order in colloidal suspensions. Physical Review E - Statistical Physics, Plasmas, Fluids, and Related Interdisciplinary Topics **57**, 6859 (1998).

[105] D. Frenkel and A. J. Ladd. New Monte Carlo method to compute the free energy of arbitrary solids. Application to the fcc and hcp phases of hard spheres. The Journal of Chemical Physics **81**, 3188 (1984).

[106] U. Gasser. Crystallization in three- and two-dimensional colloidal suspensions. Journal of Physics: Condensed Matter **21**, 203101 (2009).

[107] European Syncrotron Radiation Facility. Rat tail positions. https://www.esrf.fr/UsersAndScience/Experiments/CR [Accessed 2021-08-02] .

[108] B. J. Ackerson and P. N. Pusey. Shear-induced order in suspensions of hard spheres. Physical Review Letters **61**, 1033 (1988).

[109] B. J. Ackerson. Shear induced order and shear processing of model hard sphere suspensions. Journal of Rheology **34**, 553 (1990).

[110] Y. D. Yan, J. K. G. Dhont, C. Smits, and H. N. W. Lekkerkerker. Oscillatory-shear-induced order in nonaqueous dispersions of charged colloidal spheres. Physica A: Statistical Mechanics and its Applications **202**, 68 (1994).

[111] D. Derks, H. Wisman, A. Van Blaaderen, and A. Imhof. Confocal microscopy of colloidal dispersions in shear flow using a counter-rotating cone-plate shear cell. Journal of Physics Condensed Matter **16** (2004).

[112] G. Fiorucci and M. Dijkstra. Oscillatory shear-induced bcc-fcc martensitic transformation in a colloidal suspension with long-range repulsive interactions. Journal of Chemical Physics **154**, 164903 (2021).

[113] E. J. Stancik, G. T. Gavranovic, M. J. Widenbrant, A. T. Laschitsch, J. Vermant, and G. G. Fuller. Structure and dynamics of particle monolayers at a liquid–liquid interface subjected to shear flow. Faraday Discussions **123**, 145 (2003).

[114] V. C. Martelozzo, A. B. Schofield, W. C. Poon, and P. N. Pusey. Structural aging of crystals of hard-sphere colloids. Physical Review E - Statistical Physics, Plasmas, Fluids, and Related Interdisciplinary Topics **66**, 021408 (2002).

[115] J. Russo and H. Tanaka. Crystal nucleation as the ordering of multiple order parameters. Journal of Chemical Physics **145**, 211801 (2016).

[116] R. Ganapathy, M. R. Buckley, S. J. Gerbode, and I. Cohen. Direct measurements of Island growth and step-edge barriers in colloidal epitaxy. Science **327**, 445 (2010).

[117] A. M. Alsayed, M. F. Islam, J. Zhang, P. J. Collings, and A. G. Yodh. Premelting at defects within bulk colloidal crystals. Science **309**, 1207 (2005).

[118] V. Prasad, D. Semwogerere, and E. R. Weeks. Confocal microscopy of colloids. Journal of Physics-Condensed Matter **19**, 25 (2007).

[119] B. J. Ackerson and N. A. Clark. Shear-induced partial translational ordering of a colloidal solid. Physical Review A **30**, 906 (1984).

[120] A. Imhof, A. Van Blaaderen, and J. K. Dhont. Shear Melting of Colloidal Crystals of Charged Spheres Studied with Rheology and Polarizing Microscopy. Langmuir **10**, 3477 (1994).

[121] X. Cheng, X. Xu, S. A. Rice, A. R. Dinner, and I. Cohen. Assembly of vorticity-aligned hard-sphere colloidal strings in a simple shear flow. Proceedings of the National Academy of Sciences of the United States of America **109**, 63 (2012).

[122] W. Kabsch. A solution for the best rotation to relate two sets of vectors. Acta Crystallographica **A32**, 922 (1976).

[123] Z. W. Shan, E. A. Stach, J. M. K. Wiezorek, J. A. Knapp, D. M. Follstaedt, and S. X. Mao. Grain boundary-mediated plasticity in nanocrystalline nickel. Science **305**, 654 (2004).

[124] R. Lipowsky. Melting at grain-boundaries and surfaces. Physical Review Letters **57**, 2876 (1986).

[125] J. Q. Broughton and G. H. Gilmer. Thermodynamic criteria for grain-boundary melting - A molecular dynamics study. Physical Review Letters **56**, 2692 (1986).

[126] H. Hilgenkamp and J. Mannhart. Grain boundaries in high-T-c superconductors. Reviews of Modern Physics **74**, 485 (2002).

[127] S. Gokhale, K. H. Nagamanasa, R. Ganapathy, and A. K. Sood. Grain growth and grain boundary dynamics in colloidal polycrystals. Soft Matter **9**, 6634 (2013).

[128] K. Busch and S. John. Photonic band gap formation in certain self-organizing systems. Physical Review E - Statistical Physics, Plasmas, Fluids, and Related Interdisciplinary Topics **58**, 3896 (1998).

[129] K. S. Napolskii, N. A. Sapoletova, D. F. Gorozhankin, A. A. Eliseev, D. Y. Chernyshov, D. V. Byelov, N. A. Grigoryeva, A. A. Mistonov, W. G. Bouwman, K. O. Kvashnina, A. V. Lukashin, A. A. Snigirev, A. V. Vassilieva, S. V. Grigoriev, and A. V. Petukhov. Fabrication of artificial opals by electric-field-assisted vertical deposition. Langmuir **26**, 2346 (2010).

[130] A. P. Sutton, E. P. Banks, and A. R. Warwick. The five-dimensional parameter space of grain boundaries. Proceedings of the Royal Society A: Mathematical, Physical and Engineering Sciences **471**, 20150442 (2015).

[131] T. J. Rupert, D. S. Gianola, Y. Gan, and K. J. Hemker. Experimental observations of stress-driven grain boundary migration. Science **326**, 1686 (2009).

[132] S. L. Thomas, A. H. King, and D. J. Srolovitz. When twins collide: Twin junctions in nanocrystalline nickel. Acta Materialia **113**, 301 (2016).

[133] J. Han, S. L. Thomas, and D. J. Srolovitz. Grain-boundary kinetics: A unified approach. Progress in Materials Science **98**, 386 (2018).

[134] G. Gottstien and L. S. Shvindlerman. *Grain Boundary Migration in Metals: Thermodynamics, Kinetics, Applications* (CRC Press, 2009), 2nd edition.

[135] B. L. Adams, S. I. Wright, and K. Kunze. Orientation imaging - The emergence of a new microscopy. Metallurgical Transactions A **24**, 819 (1993).

[136] B. L. Adams. Orientation imaging microscopy: Emerging and future applications. Ultramicroscopy **67**, 11 (1997).

[137] G. Johnson, A. King, M. G. Honnicke, J. Marrow, and W. Ludwig. X-ray diffraction contrast tomography: a novel technique for three-dimensional grain mapping of polycrystals. II. The combined case. Journal of Applied Crystallography **41**, 310 (2008).

[138] W. Ludwig, S. Schmidt, E. Mejdal Lauridsen, and H. F. Poulsen. X-ray diffraction contrast tomography: a novel technique for three-dimensional grain mapping of polycrystals. I. Direct beam case. J. Appl. Cryst **41**, 302 (2008).

[139] M. P. Echlin, N. S. Husseini, J. A. Nees, and T. M. Pollock. A New Femtosecond Laser-Based Tomography Technique for Multiphase Materials. Advanced Materials **23**, 2339 (2011).

[140] P. Reischig, A. King, L. Nervo, N. Vigano, Y. Guilhem, W. J. Palenstijn, K. J. Batenburg, M. Preuss, and W. Ludwig. Advances in X-ray diffraction contrast tomography: flexibility in the setup geometry and application to multiphase materials. Journal of Applied Crystallography **46**, 297 (2013).

[141] M. D. Uchic, M. A. Groeber, D. M. Dimiduk, and J. P. Simmons. 3D microstructural characterization of nickel superalloys via serial-sectioning using a dual beam FIB-SEM. Scripta Materialia **55**, 23 (2006).

[142] N. Bozzolo, L. Chan, and A. D. Rollett. Misorientations induced by deformation twinning in titanium. Journal of Applied Crystallography **43**, 596 (2010).

[143] J. M. Dake, J. Oddershede, H. O. Sørensen, T. Werz, J. C. Shatto, K. Uesugi, S. Schmidt, C. E. Krill Iii, C. E. K. Performed, and C. E. K. Ana-Lyzed. Direct observation of grain rotations during coarsening of a semisolid Al-Cu alloy. Proceedings of the National Academy of Sciences of the United States of America **113**, E5998 (2016).

[144] A. King, P. Reischig, S. Martin, J. F. B. D. Fonseca, M. Preuss, and W. Lugwig. Grain mapping by diffraction contrast tomography: extending the technique to sub-grain information. In *Risø International Symposium on Materials Science: Challenges in materials science and possibilities in 3D and 4D characterization techniques* (Denmark, 2010).

[145] H. F. Poulsen. An introduction to three-dimensional X-ray diffraction microscopy 1. J. Appl. Cryst **45**, 1084 (2012).

[146] G. Lucadamo and D. L. Medlin. Geometric origin of hexagonal close packing at a grain boundary in gold. Science **300**, 1272 (2003).

[147] C. P. Race, J. von Pezold, and J. Neugebauer. Role of the mesoscale in migration kinetics of flat grain boundaries. Physical Review B **89**, 214110 (2014).

[148] C. P. Race, R. Hadian, J. von Pezold, B. Grabowski, and J. Neugebauer. Mechanisms and kinetics of the migration of grain boundaries containing extended defects. Physical Review B **92**, 174115 (2015).

[149] P. J. Steinhardt, D. R. Nelson, and M. Ronchetti. Bond-orientational order in liquids and glasses. Physical Review B **28**, 784 (1983).

[150] E. A. Padston. *Structure and Dynamics of Colloidal Grain Boundaries.* Ph.D. thesis (2018).

[151] P. M. Larsen, S. Schmidt, and J. Schiøtz. Robust structural identification via polyhedral template matching. Modelling and Simulation in Materials Science and Engineering **24**, 055007 (2016).

[152] A. Stukowski. Visualization and analysis of atomistic simulation data with OVITO-the Open Visualization Tool. Modelling and Simulation in Materials Science and Engineering **18**, 015012 (2010).

[153] M. Wagih and C. A. Schuh. Spectrum of grain boundary segregation energies in a polycrystal. Acta Materialia **181**, 228 (2019).

[154] A. Van Blaaderen, R. Ruel, and P. Wiltzius. Template-directed colloidal crystallization. Nature **385**, 321 (1997).

[155] J. L. Priedeman, C. W. Rosenbrock, O. K. Johnson, and E. R. Homer. Quantifying and connecting atomic and crystallographic grain boundary structure using local environment representation and dimensionality reduction techniques. Acta Materialia **161**, 431 (2018).

[156] T. Frolov, D. L. Olmsted, M. Asta, and Y. Mishin. Structural phase transformations in metallic grain boundaries. Nature Communications **4**, 1899 (2013).

[157] A. Yamanaka, K. McReynolds, and P. W. Voorhees. Phase field crystal simulation of grain boundary motion, grain rotation and dislocation reactions in a BCC bicrystal. Acta Materialia **133**, 160 (2017).

[158] O. Engler and V. Randle. *Introduction to Texture Analysis Macrotexture, Microtexture, and Orientation Mapping Introduction* (CRC Press, Boca Raton, 2010), 2nd edition.

[159] A. Morawiec. *Orientations and Rotations, Computations in Crystallographic Textures* (Springer, 2004).

[160] F. C. Frank. Orientation mapping. Metallurgical Transactions A **19**, 403 (1988).

[161] A. P. Sutton and R. W. Balluffi. *Interfaces in Crystalline Materials* (Oxford University Press, 1995).

[162] Mathworks. Navigation Toolbox: Coordinate Transformations and Trajectories: Rotations, Orientation, and Quaternions: User's Guide (R2021a). https://uk.mathworks.com/help/nav/ug/rotations-orientation-and-quaternions.html [Accessed 2021-08-17] .

[163] A. Heinz, P. Neumann, and IUCr. Representation of orientation and disorientation data for cubic, hexagonal, tetragonal and orthorhombic crystals. Acta Crystallographica Section A Foundations of Crystallography **47**, 780 (1991).

[164] A. Morawiec and D. P. Field. Rodrigues parameterization for orientation and misorientation distributions. Philosophical Magazine A **73**, 1113 (1996).

[165] J. L. Bentley. Multidimensional binary search trees used for associative searching. Communications of the ACM **18**, 509 (1975).

[166] L. Cheng, S. Chen, X. Liu, H. Xu, Y. Wu, M. Li, and Y. Chen. Registration of Laser Scanning Point Clouds: A Review. Sensors **18**, 1641 (2018).

[167] E. Schreiber. Kabsch algorithm. https://www.mathworks.com/matlabcentral/fileexchange/25746-kabsch-algorithm, MATLAB Central File Exchange [Accessed 2018-01-11] .

[168] The PyMOL Molecular Graphics System, Version 2.4, Schrödinger, LLC .

[169] H. Grimmer, W. Bollmann, D. Warrington, and IUCr. Coincidence-site lattices and complete pattern-shift in cubic crystals. Acta Crystallographica Section A **30**, 197 (1974).

[170] T. Birdal. Averaging quaternions. https://github.com/tolgabirdal/averaging_quaternions [Accessed 2021-07-15] .

[171] F. L. Markley, Y. Cheng, J. L. Crassidis, and Y. Oshman. Averaging Quaternions. Journal of Guidance, Control, and Dynamics **30**, 1193 (2007).

[172] R. Krakow, R. J. Bennett, D. N. Johnstone, Z. Vukmanovic, W. Solano-Alvarez, S. J. Lainé, J. F. Einsle, P. A. Midgley, C. M. F. Rae, and R. Hielscher. On three-dimensional misorientation spaces. Proceedings of the Royal Society A: Mathematical, Physical and Engineering Sciences **473**, 20170274 (2017).

[173] R. P. A. Dullens, M. Claesson, D. Derks, A. Van Blaaderen, and W. K. Kegel. Monodisperse core-shell poly (methyl methacrylate) latex colloids. Langmuir **19**, 5963 (2003).

[174] S. M. Klein, V. N. Manoharan, D. J. Pine, and F. F. Lange. Preparation of monodisperse PMMA microspheres in nonpolar solvents by dispersion polymerization with a macromonomeric stabilizer. Colloid and Polymer Science **282**, 7 (2003).

[175] J. Russo and H. Tanaka. Nonclassical pathways of crystallization in colloidal systems. MRS Bulletin **41**, 369 (2016).

[176] K. F. Kelton and A. L. Greer. *Nucleation in condensed matter: Applications in materials and biology* (Pergamon, 2010).

[177] T. Kawasaki and H. Tanaka. Formation of a crystal nucleus from liquid. Proceedings of the National Academy of Sciences of the United States of America **107**, 14036 (2010).

[178] K. Iland, J. Wölk, R. Strey, and D. Kashchiev. Argon nucleation in a cryogenic nucleation pulse chamber. Journal of Chemical Physics **127**, 154506 (2007).

[179] W. Ostwald. The formation and changes of solids (translated from german). Zeitschrift für Physikalische Chemie **22**, 289 (1897).

[180] J. S. Van Duijneveldt and D. Frenkel. Computer simulation study of free energy barriers in crystal nucleation. The Journal of Chemical Physics **96**, 4655 (1992).

[181] P. R. ten Wolde, M. J. Ruiz-Montero, and D. Frenkel. Numerical evidence for bcc ordering at the surface of a critical fcc nucleus. Physical Review Letters **75**, 2714 (1995).

[182] S. Auer and D. Frenkel. Suppression of crystal nucleation in polydisperse colloids due to increase of the surface free energy. Nature **413**, 711 (2001).

[183] P. N. Pusey, E. Zaccarelli, C. Valeriani, E. Sanz, W. C. K. Poon, and M. E. Cates. Hard spheres: crystallization and glass formation. Philosophical Transactions of the Royal Society a-Mathematical Physical and Engineering Sciences **367**, 4993 (2009).

[184] P. R. ten Wolde, M. J. Ruiz-Montero, and D. Frenkel. Simulation of homogeneous crystal nucleation close to coexistence. Faraday Discussions **104**, 93 (1996).

[185] P. N. Pusey, W. van Megen, P. Bartlett, B. J. Ackerson, J. G. Rarity, and S. M. Underwood. Structure of crystals of hard colloidal spheres. Physical Review Letters **63**, 2753 (1989).

[186] J. Zhu, M. Li, R. Rogers, W. Meyer, R. H. Ottewill, W. B. Russel, and P. M. Chaikin. Crystallization of hard-sphere colloids in microgravity. Nature 1997 387:6636 **387**, 883 (1997).

[187] P. R. ten Wolde, M. J. Ruiz-Montero, and D. Frenkel. Numerical calculation of the rate of crystal nucleation in a Lennard-Jones system at moderate undercooling. The Journal of Chemical Physics **104**, 9932 (1996).

[188] R. Ohnesorge, H. Löwen, and H. Wagner. Density functional theory of crystal-fluid interfaces and surface melting. Physical Review E **50**, 4801 (1994).

[189] W. Mickel, S. C. Kapfer, G. E. Schroder-Turk, and K. Mecke. Shortcomings of the bond orientational order parameters for the analysis of disordered particulate matter. Journal of Chemical Physics **138**, 044501 (2013).

Publications

To date, the following publications based upon work in this thesis have been submitted or are in preparation.

N. H. P. Orr, T. Yanagishima, I. P. Dolbnya, A. V. Petukhov, and R. P. A. Dullens. Colloidal crystallisation induced by capillary action. *In preparation* (Chapter 3).

N. H. P. Orr, T. Yanagishima, I. P. Dolbnya, A. V. Petukhov, and R. P. A. Dullens. Deformation under gravity of shear-aligned colloidal crystals. *In preparation* (Chapter 4).

N. H. P. Orr, T. Yanagishima, E. Maire, and R. P. A. Dullens. Grain boundary characterisation from particle coordinates. *Submitted* (Chapter 5).

N. H. P. Orr, T. Yanagishima, and R. P. A. Dullens. Misorientation during homogeneous nucleation of a colloidal crystal. *In preparation* (Chapter 6).

Acknowledgements

Firstly, thank you to Roel and Andrei for the support, guidance and inspiration throughout my D.Phil studies. I feel truly grateful to have learnt so much from you.

I would also like to thank my colleagues, especially those resident in the big office. Thank you Taiki for the detailed help over so many academic topics and encouragement over the long beam time sessions at ESRF and Diamond. Thanks also go to Carla, for the support and good times both inside and outside of work; to Arran, for your encyclopedic optics knowledge and for always being up for a cheerful chat; and to Balkis, for help with maths and large supply of jokes.

Special thanks also goes to Harry and Dom, you have been great housemates and fantastic friends throughout. Thank you Mati, for brilliant advice on mechanics and for essential support during thesis writing. Finally, thank you to Mum and Kieran, for support in so many ways.